ACTUAL PROBLEMS OF MODERN SCIENCE, EDUCATION AND TRAINING

KHOREZMSCIENCE.UZ





CONTENTS

Section 1. MODERN PROBLEMS OF PEDAGOGY AND PSYCHOLOGY…..4

MUXAMMADIYEV G‘AYRAT G‘ANIYEVICH // PEDAGOGICAL MODEL FOR IMPROVING THE INFORMATION SECURITY COMPETENCE OF LIBRARY SPECIALISTS IN IN-SERVICE TRAINING: COMPARATIVE POSITIONING AGAINST EXISTING MODELS.....4

RUZIYEVA DILAFRUZ RAUPOVNA // THE STRUCTURE OF COMPETENCE IN CREATING ARTIFICIAL INTELLIGENCE ELEMENTS AMONG FUTURE INFORMATICS SPECIALISTS AND A METHODOLOGICAL MODEL FOR ITS DEVELOPMENT 15

Section 2. ACTUAL PROBLEMS IN MODERN TOURISM AND ECONOMICS……24

ALTIBAYEVA MUXAYYO BEGIMQULOVNA // ASSESSING THE POTENTIAL FOR THE TERRITORIAL DEVELOPMENT OF SERVICE SECTORS IN THE SIRDARYO REGION 24

Section 3. ACRUAL PROBLEMS IN MODERN TECHNICAL SCIENCES….32

ATAJONOV MUZAFFAR NE’MATJON O‘G‘LI // ADAPTIVE DETECTION OF SPAM IN UZBEK-LANGUAGE MESSAGES: EVALUATION UNDER DATA-PROVENANCE SHIFT AND DRIFT-TRIGGERED RETRAINING.....32

MATYOKUBOV UTKIR KARIMOVICH, DAVRONBEKOV DILMUROD ABDUJALILOVICH, MURADOV MUHAMMAD MUROD UGLI // EVALUATING THE SURVIVAL OF HYBRID TELECOMMUNICATION NETWORKS CONSIDERING COMMON CAUSED FAULTS AND PHYSICAL RESOURCE LIMITS ..43

MATYOKUBOV UTKIR KARIMOVICH // A MODEL FOR ASSESSING CONFIRMED RECOVERY OF CRITICAL TELECOMMUNICATIONS SERVICES USING TIME CONSTRAINTS AND EPISODE MEMORY 60

JURAKULOV TOLIB TOKHIROVICH // DESIGN AND EVALUATION PROTOCOL OF THE SEMANTIC SIMILARITY ANALYZER FOR AUTOMATIC DETECTION OF SEMANTIC SIMILARITY IN UZBEK TEXTS.....76

Section 4. ACTUAL PROBLEMS OF HISTORY, PHILOSOPHY AND SOCIOLOGY……90

SAIPOVA MADINA SAIDAXBOR QIZI // ARCHITECTURAL, ARTISTIC, AND SEMANTIC ANALYSIS OF THE CRESCENT SYMBOL AT THE APEX OF THE TAJ MAHAL DOME.....90

Section 5. ACTUAL PROBLEMS OF NATURAL SCIENCES……..100

KELDIYOROVA SHOXIDA XUSNIDDIN QIZI // HISTOMORPHOMETRIC EVALUATION OF THE AMELIORATIVE EFFECTS OF BITTER ALMOND EXTRACT ON E171-INDUCED THYMIC INJURY IN RATS 100

Section 6. ACTUAL PROBLEMS OF MATHEMATICS, PHYSICS AND MECHANICS……106

ERKABOEV ULUGBEK, KHABIBULLAEVA LAYLOKHON, RAKHIMOV RUSTAMJON // DETERMINATION OF THE BAND GAP OF SEMICONDUCTORS IN A QUANTIZING MAGNETIC FIELD.....106

BEXZOD JUMABOYEV QURONBOY O‘G‘LI, OTAXONOVA NAFISA OMONBOY QIZI, DAVLATOVA MAQSUDA MUXIDDIN QIZI, XUSHNUDBEK SAPAROV SHARIPBAYEVICH, ORTIKOVA DILNURA UMID QIZI // EFFECT OF HEIGHT ON THE EFFICIENCY OF A SILICON VERTICAL TUNNEL-JUNCTION CONCENTRATOR SOLAR CELL: TCAD MODELLING WITH A CALIBRATED TUNNEL JUNCTION MODEL 117

ISMAILOV SHIKHNAZAR RASHIDOVICH, KHASANOV AZIZBEK BAKHODIROVICH, ABDUKARIMOV NABIJON IBADULLAYEVICH // UNSTEADY FLOW IN A CAVITY WITH A CENTRAL CUTOUT 127

KUTLIYEV UCHKUN OTOBOYEVICH, BEKCHANOVA KUVONCH KUVONDIKOVNA // COMPUTER SIMULATION OF ANGULAR AND ENERGY DISTRIBUTIONS OF NE^{+} IONS SCATERRED FROM THE $SI_{0.25}GE_{0.75}$(100) SURFACE 136

UTAMURADOVA SHARIFA BEKMURADOVNA, FAYZULLAYEV QAHRAMON MAHMUDJONOVICH, STANCHIK ALIONA VIKTOROVNA, XAMIDOVA NIGORA A’ZAMJON QIZI // EDS ANALYSIS OF TI/CU/SN/NI PRECURSORS FOR THIN-FILM SOLAR CELLS 146

MATCHONOV KHUSNIDDIN JAMOLADDINOVICH // RAMAN SPECTROSCOPY AND CHEMICAL MAPPING ANALYSIS OF MANGANESE-DOPED SILICON STRUCTURES 151

MAVLYANOV ABDULAZIZ SHAVKATOVICH // X-RAY DIFFRACTION ANALYSIS OF SI <MN, S> SAMPLES 157

Section 1. MODERN PROBLEMS OF PEDAGOGY AND PSYCHOLOGY

UDC 023.5:378.046.4:004.056

PEDAGOGICAL MODEL FOR IMPROVING THE INFORMATION SECURITY COMPETENCE OF LIBRARY SPECIALISTS IN IN-SERVICE TRAINING: COMPARATIVE POSITIONING AGAINST EXISTING MODELS

Muxammadiyev G‘ayrat G‘aniyevich
Independent PhD Researcher, Uzbekistan State Institute of Arts and Culture Tashkent, Uzbekistan
gayratgm1213.gfu@gmail.com

Annotatsiya. Kutubxona xodimlari foydalanuvchilarning shaxsga doir ma’lumotlari, litsenziyalangan elektron resurslar va avtomatlashtirilgan kutubxona tizimlari bilan ishlaydi, biroq ularning axborot xavfsizligi (AX) bo‘yicha malaka oshirishi kamdan-kam hollarda shu kasbga mo‘ljallangan pedagogik modelga tayanadi. Maqolada muallifning pedagogik modeli sakkizta mavjud model va tadqiqot bilan sakkiz mezon bo‘yicha qiyoslandi. Natijada “maqsad – mazmun – jarayon – natija” o‘zagi deyarli barcha modellarda takrorlanishi, diagnostika, lavozim bo‘yicha tabaqalash va takroriy monitoring esa faqat alohida tadqiqotlarda uchrashi hamda hech birida kutubxonaga xos AX mazmuni bilan birlashtirilmagani aniqlandi. Taklif etilgan model bu elementlarni malaka oshirish jarayonida birlashtiradi, kompetensiya tuzilmasini tashkiliy-huquqiy va kommunikativ-pedagogik komponentlar bilan to‘ldiradi hamda muallifniki va moslashtirilgan pedagogik shartlarni ajratib ko‘rsatadi.

Kalit so‘zlar: *axborot xavfsizligi kompetensiyasi; kutubxona mutaxassislari; malaka oshirish; pedagogik model; pedagogik shart-sharoitlar; qiyosiy tahlil.*

Аннотация. Сотрудники библиотек работают с персональными данными пользователей, лицензионными электронными ресурсами и автоматизированными библиотечными системами, однако их повышение квалификации в области информационной безопасности (ИБ) редко опирается на педагогическую модель, разработанную для этой профессии. В статье авторская модель сопоставлена с восемью существующими моделями и исследованиями по восьми критериям. Установлено, что ядро «цель – содержание – процесс – результат» повторяется почти во всех моделях, тогда как диагностика, дифференциация по должности и повторный мониторинг

встречаются лишь в отдельных исследованиях и нигде не объединены с библиотечно-специфическим содержанием ИБ. Предлагаемая модель объединяет эти элементы в процессе повышения квалификации, дополняет структуру компетентности организационно-правовым и коммуникативно-педагогическим компонентами и разграничивает авторские и адаптированные педагогические условия.

Ключевые слова: *компетентность в области информационной безопасности; библиотечные специалисты; повышение квалификации; педагогическая модель; педагогические условия; сравнительный анализ.*

Abstract. Library staff handle patron personal data, licensed electronic resources and automated library systems, yet their in-service information security (IS) training is rarely built on a pedagogical model designed for this profession. The article compares the author's model with eight existing models and studies using eight criteria. The "goal – content – process – result" core is shared by almost all models, whereas diagnosis, differentiation by position and repeated monitoring appear only in separate studies and are nowhere combined with library-specific IS content. The proposed model integrates these elements within in-service training, adds organisational-legal and communicative-pedagogical components to the competence structure, and distinguishes its original pedagogical conditions from adapted ones.

Key words: *information security competence; library specialists; in-service training; pedagogical model; pedagogical conditions; comparative analysis.*

Introduction

Libraries hold personal data of patrons, licensed electronic content and catalogue databases, and staff with very different duties work inside the same automated library system. Human-related weaknesses are therefore a central source of risk. A national survey of 388 Estonian librarians based on the knowledge–attitude–behaviour model concluded that the knowledge of library staff about information security rules and procedures, as well as their attitude towards them, is still not sufficient to ensure competent behaviour [1, p. 146]. In the same survey librarians described the available

cybersecurity training as "either too general and superficial or they assume a higher education in IT" [1, p. 146].

Research on security awareness stresses that programmes should be tailored to specific groups of employees [2, p. 3]. An analysis of 27 security competency models showed that many reduce the expert's profile to professional competencies, omitting social, personal and methodological ones [3, p. 25:1]. For library staff, who advise patrons and must comply with personal data legislation, such a reduction is particularly problematic.

The author's dissertation research developed a pedagogical model for improving the IS competence of library specialists in in-service training. Such a model can claim scientific novelty only if it is compared with existing models and its borrowed elements are separated from new ones. Without this comparison, a claim that "no model exists for librarians" is easily refuted, since studies of IS education for library employees [4] and of library specialists' professional development [5] already exist.

This article aims to position the proposed model against existing models using a transparent set of criteria. Three research questions were posed: (RQ1) which elements do existing models share and where do they differ; (RQ2) which elements of the proposed model are borrowed, adapted or new; (RQ3) which of its eight pedagogical conditions are original and which are adapted from earlier work.

Literature Review

Models for future teachers. Bogatyreva developed a methodical system for training future teachers to ensure schoolchildren's information security, with target, content, organisational, procedural and evaluative-result components [6, p. 260]; competence was represented as the unity of cognitive, motivational-activity and axiological components [6, p. 325], and the experimental work was carried out in 2010–2014 [6, p. 305]. Lomasko built a projective methodical system around a separate 74-hour course "Information Security" for future informatics teachers [7, p. 101], distinguishing cognitive, axiological, activity and reflexive aspects of IS competence [7, pp. 60–63], its legal, administrative, software-technical and socio-cultural constituents, and three levels of formation – low, medium and high [7, p. 70]. Nechay proposed a

conceptual model with target, procedural and result components and seven professional competences of a future informatics teacher, from acting in accordance with legislation to protecting the user in computer networks [8, pp. 80–81]; in the formative experiment the generalised level of preparation reached 97 % in the experimental group versus 37 % in the control group [8, p. 123].

Models for in-service teachers. Khlebnikova and Dolinina designed a model for forming teachers' IS competence in advanced training with target, methodological, content, criterial-diagnostic and result blocks [9, p. 4]; its content block comprises knowledge, value and behavioural components [9, pp. 4–5], while the criterial-diagnostic block only outlines criteria, diagnostic methods and levels of formation [9, p. 5]. Jumaniyozova's model for improving the creative competence of university teachers in continuous in-service training has target, technological-methodical, organisational, diagnostic and result blocks and three levels [10, p. 128], with conditions grouped as general pedagogical, methodical and specific [10, p. 120], but contains no IS content.

Studies of library staff development. Boris grounded the professional development of library specialists in contextual adult learning, continuous education and andragogy [5, p. 5] and identified seven innovative competences for library managers and nine for library staff [5, p. 7]. In her seminar-training technology, training needs are diagnosed during the preceding year and the session lasts five eight-hour working days [5, p. 21]; surveyed specialists preferred problem-oriented seminars of no more than ten days [5, p. 15]. San Nicolas-Rocca and Burkhard examined an online cybersecurity course for library employees based on NIST SP 800-53 and 800-60 and FIPS 199 and 200, ending with an organisational risk management project [4, p. 62]. All 22 surveyed employees reported acquiring knowledge of information security risks [4, p. 64], but only twelve had applied it in their libraries [4, p. 65]. Da Veiga and Martins showed that an organisation's information security culture can be improved through repeated assessment and follow-up actions: over eight years, four assessments in twelve countries raised the overall culture mean from 3.89 to 4.10 [11].

International guidance. The IFLA principles of continuing professional development require regular learning-needs assessment, modules from introductory to

advanced level, attention to training transfer and feedback, and follow-up evaluation of the effect on practice [12, pp. 1–3]. A review of gamified cybersecurity awareness for non-IT professionals found positive effects documented mainly for the short term, while long-term effectiveness, including habituation, remains unknown [13, p. 95].

Thus, all elements needed for a model for library specialists – IS content, competence structure, levels, differentiation by position, pedagogical conditions and repeated measurement – already exist, but in different works and for different target groups. The question is therefore not whether these elements are new, but whether and how they have been combined for library specialists.

Research Methodology

The study used a criterion-based comparative analysis of documents. Eight works were selected according to three rules: the work describes a model, methodical system or technology for developing IS competence or for the professional development of library staff with an explicit structure; the full text is available; the text is in Russian, Uzbek or English. The sample consists of three models for future teachers [6], [7], [8], two models for in-service teachers [9], [10] and three studies of library staff or organisational security culture [5], [4], [11].

Each work was described by eight criteria: C1 – target group; C2 – IS content; C3 – competence structure; C4 – levels of formation; C5 – differentiation by position; C6 – pedagogical conditions; C7 – block structure; C8 – delayed or repeated monitoring. The source page was recorded for every cell, and characteristics not described in a source were marked “not identified” (n/i) rather than inferred.

In the second step each block of the proposed model was compared with its closest analogue and classified as borrowed, adapted or new (RQ2); in the third step each of the eight pedagogical conditions was classified as the author’s own or adapted from a named source (RQ3). The study is limited to document analysis; the effectiveness of the model will be tested in the experimental stage, whose results are not reported here.

Analysis and Results

Comparison of models (RQ1). The results of the comparison are summarised in Table 1.

Table 1. Comparison of IS competence and library staff development models

Work	Target group	IS content	Competence structure	Levels	Position differentiation	Delayed monitoring
Bogatyreva [6]	future teachers	yes (pupils' IS)	3 components [6, p. 325]	initial to advanced [6, p. 274]	no	no
Lomasko [7]	future informatics teachers	yes (technical focus)	4 aspects [7, pp. 60–63]	3 [7, p. 70]	no	no
Nechay [8]	future informatics teachers	yes	7 competences [8, p. 81]	n/i	no	no
Khlebnikova, Dolinina [9]	in-service teachers	yes	3 components [9, pp. 4–5]	not detailed [9, p. 5]	no	no
Jumaniyozova [10]	university teachers, in-service	no	creativity indicators	3 [10, p. 128]	no	no
Boris [5]	library managers and staff	no	innovative competences	n/i	yes: 7 / 9 [5, p. 7]	no
San Nicolas-Rocca, Burkhard [4]	library staff (online course)	yes	4 transfer factors [4, p. 59]	n/i	no	one-off
Da Veiga, Martins [11]	employees of a financial institution	yes (culture)	culture dimensions	n/i	no	yes: four assessments over 8 years
Proposed model	library specialists, in-service	yes, library-specific	6 components	3	yes: 3 categories	yes: 2 weeks and 3–6 months

Note: compiled by the author; n/i – not identified in the analysed text. C6 and C7 are compared in Table 3 and Figure 1.

Three observations follow from Table 1. First, three of the eight works address students – future teachers – and only one combines in-service training with IS content [9], but its target group is school teachers. Second, the library studies cover the elements separately: Boris differentiates competences by position but without IS content [5], San Nicolas-Rocca and Burkhard address IS content and knowledge transfer but without levels or pedagogical conditions [4], and Da Veiga and Martins demonstrate a repeated assessment cycle at the level of organisational culture rather than individual competence [11]. Third, although block names differ, the core "goal – content – process – result" is

repeated in almost all models [6], [9], [10]; diagnosis is a separate block only in some of them [9], [10], whereas Boris treats diagnosis of training needs as part of the organisational stage [5, p. 21].

Competence structure. Table 2 compares the components of IS competence in the models that define them explicitly.

Table 2. Components of IS competence in the compared models

Component of the proposed model	Bogatyreva [6]	Lomasko [7]	Khlebnikova, Dolinina [9]	Proposed model
Cognitive	+	+	≈ knowledge	+
Operational-technological	≈ motivational-activity	≈ activity	≈ behavioural	+
Organisational-legal	–	– (legal constituent of content)	–	+
Axiological-ethical	+	+	≈ value	+
Communicative-pedagogical	–	–	–	+
Reflexive-adaptive	–	+	–	+

Note: "+" – the component is distinguished; "≈" – the closest analogue under another name; "–" – not distinguished. Lomasko treats legal issues as a constituent of content, not as a component of competence [7, p. 70].

The organisational-legal and communicative-pedagogical components are not distinguished as components of competence in any of the three models. For library specialists both are central: the first reflects work with patron personal data and licence conditions, the second reflects the double role of the librarian, who protects information and also explains safe digital behaviour to patrons. The reflexive-adaptive component is present only in Lomasko's structure [7, p. 63].

Borrowed and new elements (RQ2). Figure 1 shows the proposed model with the sources of its adapted elements. The component structure follows the tradition of Bogatyreva and Lomasko [6], [7]; the diagnostic block is adapted from Khlebnikova and Dolinina and from Jumaniyozova [9], [10]; the andragogic approach, short seminar-training forms and the idea of differentiating competences by position are taken from Boris [5]; the final real job task follows the organisational risk management project in the course studied by San Nicolas-Rocca and Burkhard [4, p. 62]; and the idea of a repeated assessment cycle follows Da Veiga and Martins [11].

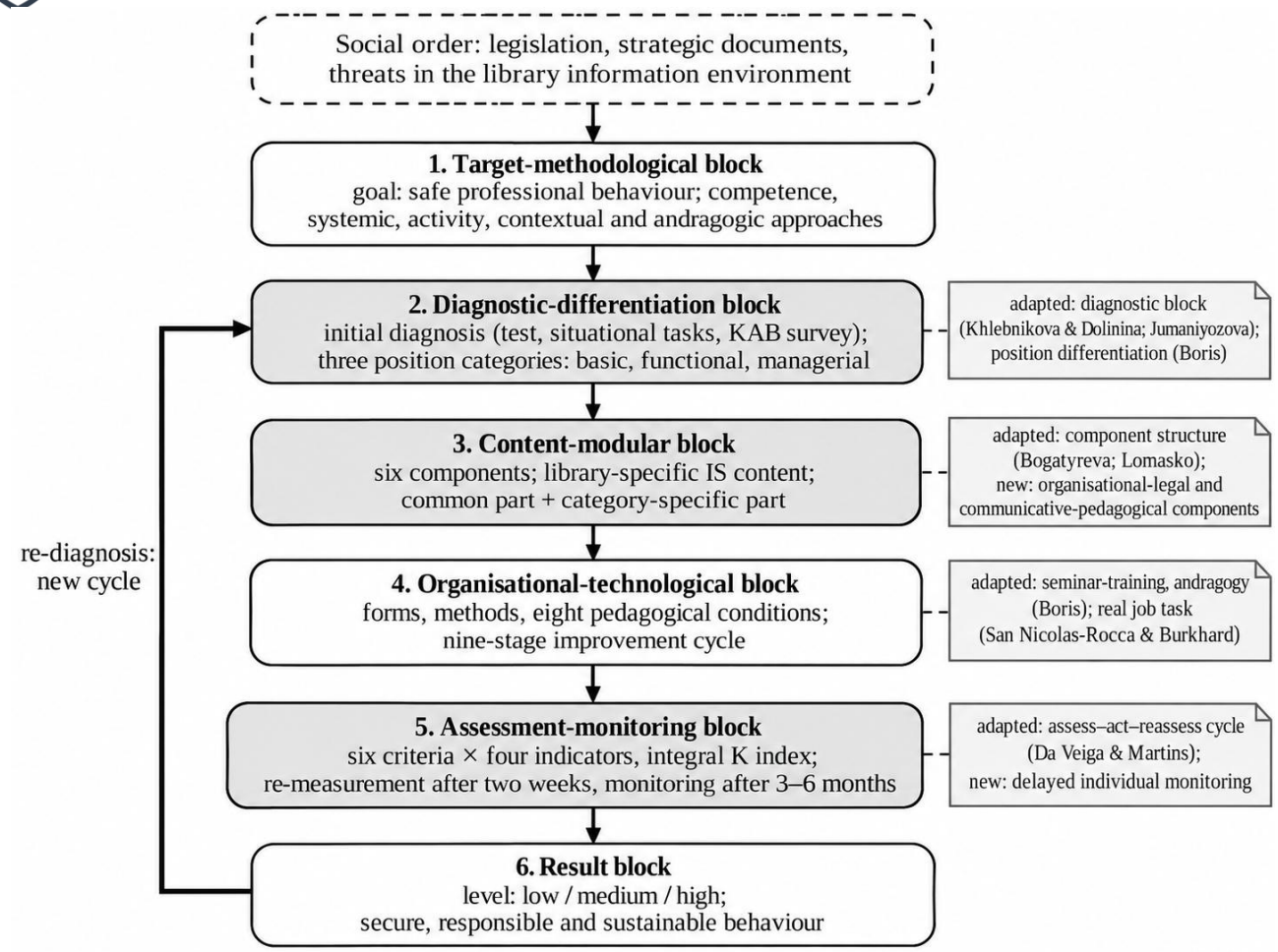


Figure 1. Pedagogical model for improving the IS competence of library specialists and sources of its adapted elements (grey – blocks containing new elements)

New in the model are four elements. (1) IS content is tied to library processes – the automated library system, electronic resources, patron data, copyright and the use of artificial intelligence services. (2) The competence structure contains six components, including the organisational-legal and communicative-pedagogical ones. (3) Content is differentiated into a common part for all employees and category parts for basic, functional and managerial positions. (4) Assessment uses six criteria with four indicators each and an integral K index, and the cycle is closed by re-measurement after two weeks and delayed monitoring after three to six months, which turns the result into the starting point of a new cycle. The fourth element responds to two findings of the review: knowledge acquired in a course is not always applied [4, pp. 64–65], and the long-term effect of awareness training remains insufficiently studied [13, p. 95].

Origin of the pedagogical conditions (RQ3). The model is implemented under eight pedagogical conditions grouped into content-methodical, psychological-pedagogical and organisational ones. Their origin is shown in Table 3.

Table 3. Pedagogical conditions of the model and their origin

No.	Condition	Group	Origin
1	Integration of training with real library work	content-methodical	author's development (based on IFLA principles [12])
2	Initial diagnosis	psychological-pedagogical	adapted from IFLA needs assessment [12, p. 1]
3	Individual and differentiated approach	psychological-pedagogical	adapted from IFLA [12, pp. 1–2] and Rakitskaya [14, p. 704]
4	Unity of theory and practice	content-methodical	adapted from Bogatyreva [6]
5	Safe learning and simulation environment	content-methodical	author's development
6	Institutional support	organisational	adapted from IFLA [12, pp. 1–2]
7	Reflection and feedback	psychological-pedagogical	adapted from Rakitskaya [14, pp. 704–705] and IFLA [12, pp. 1, 3]
8	Continuous professional development	organisational	adapted from IFLA [12, p. 1] and Jumaniyozova [10, p. 132]

Note: compiled by the author.

Two of the eight conditions are the author's development and six are adapted. Making this distinction explicit is important for the defence of the model: it shows that the contribution lies not in the number of conditions but in their selection for library work and in their link to the blocks of the model.

Results and Discussion

The comparison does not support the broad claim that no pedagogical model exists for librarians in the field of IS. It supports a narrower and verifiable claim: among the eight examined works, none combines library-specific IS content, a multi-component competence structure with levels, differentiation by position, explicitly substantiated pedagogical conditions and delayed monitoring within the in-service training of library specialists. This formulation is consistent with the conclusion of Bendler and Felderer that security competency models should not be reduced to professional competencies [3, p. 25:1], and with the IFLA requirement to evaluate the effect of training on practice [12, p. 3]. The analysis also has limitations: the sample

includes eight works, the classification of elements is the author's, and the effectiveness of the model has not yet been confirmed empirically.

Conclusion and Recommendations

The comparative analysis showed that existing models share the "goal – content – process – result" core but differ in target group, IS content and the treatment of diagnosis, differentiation and monitoring. The novelty of the proposed model lies in the combination of these elements for library specialists, in the organisational-legal and communicative-pedagogical components of competence, and in the closed cycle with delayed monitoring. On this basis the following recommendations are made:

1) when the novelty of a pedagogical model is claimed, the borrowed, adapted and new elements should be separated in a comparison table with page references, and the claim should be formulated as a combination of elements for a specific target group rather than as the absence of any model;

2) in-service IS training of library specialists should include, alongside technical content, organisational-legal tasks (patron personal data, licence conditions) and communicative-pedagogical tasks (explaining safe digital behaviour to patrons);

3) the effect of training should be measured not only at the end of the course but also after two weeks and after three to six months, so that the results become the basis for the next cycle of professional development;

4) the pedagogical conditions should be presented with their origin, so that the author's contribution and the adapted international and national experience can be assessed separately.

References:

[1]K.-R. Kont, "The role of libraries in creating a safer cyberspace: awareness of Estonian library employees in information security," International Information & Library Review, vol. 56, no. 2, pp. 135–149, 2024, doi: 10.1080/10572317.2024.2315630.

[2]O. Pahlavanpour and S. Gao, "A systematic mapping study on gamification within information security awareness programs," Heliyon, vol. 10, Art. no. e38474, 2024, doi: 10.1016/j.heliyon.2024.e38474.

[3] D. Bendler and M. Felderer, “Competency models for information security and cybersecurity professionals: analysis of existing work and a new model,” ACM Transactions on Computing Education, vol. 23, no. 2, Art. no. 25, 2023, doi: 10.1145/3573205.

[4]T. San Nicolas-Rocca and R. J. Burkhard, “Information security in libraries: examining the effects of knowledge transfer,” Information Technology and Libraries, vol. 38, no. 2, pp. 58–71, 2019, doi: 10.6017/ital.v38i2.10973.

[5]I. V. Boris, “Innovatsionnaya kompetentnost’ kak rezul’tat professional’nogo razvitiya bibliotechnogo spetsialista” [Innovative competence as a result of the professional development of a library specialist], Extended abstract of Cand. Sci. (Pedagogy) dissertation, St. Petersburg State University of Culture and Arts, St. Petersburg, Russia, 2010 (in Russian).

[6]Yu. I. Bogatyreva, “Podgotovka budushchikh pedagogov k obespecheniyu informatsionnoi bezopasnosti shkol’nikov” [Training future teachers to ensure the information security of schoolchildren], Dr. Sci. (Pedagogy) dissertation, Tula State University, Tula, Russia, 2014 (in Russian).

[7]P. S. Lomasko, “Metodicheskaya sistema podgotovki uchitelya informatiki v oblasti informatsionnoi bezopasnosti” [Methodical system for training informatics teachers in information security], Cand. Sci. (Pedagogy) dissertation, Krasnoyarsk State Pedagogical University named after V. P. Astafyev, Krasnoyarsk, Russia, 2009 (in Russian).

[8]A. A. Nechay, “Formirovanie professional’nykh kompetentsii budushchego uchitelya informatiki v oblasti informatsionnoi bezopasnosti v usloviyakh tsifrovizatsii obrazovaniya” [Formation of professional competences of future informatics teachers in information security under the digitalisation of education], Cand. Sci. (Pedagogy) dissertation, Pushkin Leningrad State University, St. Petersburg, Russia, 2023 (in Russian).

[9]M. A. Khlebnikova and I. G. Dolinina, “Model’ formirovaniya kompetentnosti informatsionnoi bezopasnosti pedagogov v protsesse povysheniya kvalifikatsii” [Model for the formation of information security competence of teachers in the process of advanced training], World of Science. Pedagogy and Psychology, vol. 8, no. 3, 2020.

[10] M. T. Jumaniyozova, O‘qituvchining kasbiy kreativligini takomillashtirish texnologiyalari [Technologies for improving the professional creativity of teachers]. Tashkent, Uzbekistan: Metodist nashriyoti, 2023 (in Uzbek).

[11] A. Da Veiga and N. Martins, “Improving the information security culture through monitoring and implementation actions illustrated through a case study,” Computers & Security, vol. 49, pp. 162–176, 2015, doi: 10.1016/j.cose.2014.12.006.

[12] J. Varlejs, Continuing Professional Development: Principles and Best Practices. The Hague, Netherlands: IFLA Continuing Professional Development and Workplace Learning Section, n.d.

[13] A. K. Gwenhure and F. S. Rahayu, “Gamification of cybersecurity awareness for non-IT professionals: a systematic literature review,” International Journal of Serious Games, vol. 11, no. 1, pp. 83–99, 2024, doi: 10.17083/ijsg.v11i1.719.

[14] L. M. Rakitskaya, “Metodicheskaya rabota po formirovaniyu informatsionnoi kompetentsii bibliotechnykh spetsialistov, rabotayushchikh s informatsionno-pravovymi sistemami” [Methodical work on the formation of information competence of librarians working with legal information systems], Bibliotekovedenie [Library and Information Science], vol. 65, no. 6, pp. 701–708, 2016 (in Russian).

UDC: 378.147:004.8

THE STRUCTURE OF COMPETENCE IN CREATING ARTIFICIAL INTELLIGENCE ELEMENTS AMONG FUTURE INFORMATICS SPECIALISTS AND A METHODOLOGICAL MODEL FOR ITS DEVELOPMENT

Ruziyeva Dilafruz Raupovna
Associate Professor, Department of Digital Technologies, Navoi State University
dilafruzruziyeva31@gmail.com

Annotatsiya. Maqolada oliy ta’lim muassasalarida bo‘lajak informatika mutaxassislarini sun’iy intellektdan faqat foydalanuvchi sifatida emas, balki uning elementlarini yaratuvchi sifatida tayyorlash zarurati asoslangan. “Sun’iy intellekt elementlarini yaratish kompetentligi” tushunchasiga mualliflik ta’rifi berilgan. Kompetentlikning motivatsion-qadriyatli, kognitiv, operatsion-texnologik va refleksiv-loyihaviy komponentlari hamda ularning ko‘rsatkichlari ajratilgan. Haqiqiy hududiy ma’lumotlar asosidagi loyihalarga tayangan to‘rt bosqichli metodik model va kompetentlik shakllanganligining uch darajali baholash mezonlari taklif etilgan.

Kalit so‘zlar: *sun’iy intellekt, kompetentlik, sun’iy intellekt elementlari, mashinali o‘qitish, loyihaviy ta’lim, haqiqiy ma’lumotlar, metodik model, informatika ta’limi.*

Аннотация. В статье обоснована необходимость подготовки будущих специалистов по информатике не только как пользователей искусственного интеллекта, но и как создателей его элементов. Дано авторское определение понятия «компетентность в создании элементов искусственного интеллекта». Выделены мотивационно-ценностный, когнитивный, операционно-технологический и рефлексивно-проектный компоненты компетентности и их показатели. Предложены четырёхэтапная методическая модель, опирающаяся на проекты с реальными региональными данными, и трёхуровневые критерии оценки сформированности компетентности.

Ключевые слова: *искусственный интеллект, компетентность, элементы искусственного интеллекта, машинное обучение, проектное обучение, реальные данные, методическая модель, обучение информатике.*

Abstract. The article substantiates the need to prepare future informatics specialists in higher education institutions not only as users of artificial intelligence but as creators of its elements. An original definition of the concept “competence in creating artificial intelligence elements” is proposed. The motivational-value, cognitive, operational-technological and reflective-project components of this competence and their indicators are identified. A four-stage methodological model based on projects with authentic regional data and three-level criteria for assessing the development of the competence are proposed.

Key words: *artificial intelligence, competence, artificial intelligence elements, machine learning, project-based learning, authentic data, methodological model, informatics education.*

Introduction

Artificial intelligence (AI) technologies have become an integral part of the economy, public administration, healthcare and water management. Resolution No. PQ-4996 of the President of the Republic of Uzbekistan of 17 February 2021 established conditions for the accelerated introduction of AI technologies [1]. Resolution No. PQ-358 of 14 October 2024 approved the Strategy for the development of AI technologies

until 2030 [2]. Both documents identify the training of qualified AI personnel as a priority task.

At the same time, higher education practice mostly teaches AI as a ready-made tool. Students learn to use chatbots, ready-made libraries and cloud services, but gain no experience in creative activities such as preparing data, choosing a model architecture, training the model and evaluating it. As a result, AI is perceived as a "black box": graduates know how to use it but do not understand its inner mechanism.

For a future informatics specialist this is not enough. The labour market needs specialists who design AI systems, adapt them to local problems and assess their reliability. There is therefore a pedagogical contradiction between the levels of "using AI" and "creating AI elements": the content of education is oriented towards the former, while the needs of society are oriented towards the latter.

The aim of the article is to determine the content and structure of the competence in creating AI elements among future informatics specialists and to develop a methodological model for its development. To achieve this aim, the following tasks were set: to define the concept; to identify the components of the competence and their indicators; to substantiate the blocks of the methodological model; and to establish criteria for assessing the levels of the competence.

Literature review

Foreign research on AI education focuses mainly on the concept of "AI literacy". D.Long and B.Magerko define AI literacy as a set of competencies that enable individuals to critically evaluate AI technologies, communicate effectively with them and collaborate with them [3]. D.Touretzky and co-authors identified "five big ideas" of AI for school education: perception, representation and reasoning, learning, natural interaction, and societal impact [4].

Having reviewed the literature on AI literacy, D.Ng and co-authors identified its four aspects: knowing and understanding, using and applying, evaluating and creating, and ethical issues [5]. The authors note that the "creating" level is the least studied area. M.Tedre and co-authors substantiated the need to shift from traditional programming to data-driven thinking when teaching machine learning [6].

In 2024 UNESCO published the AI competency framework for students, which distinguishes the levels of “understand”, “apply” and “create” [7]. The European Union DigComp 2.2 framework also includes interaction with AI systems in digital competence [8]. O.Zawacki-Richter and co-authors showed that most studies of AI in higher education focus on the technological side, while the pedagogical foundations remain insufficiently developed [9].

The general pedagogical foundations of the concept of competence are covered in the works of I.A.Zimnyaya and A.V.Khutorskoy [10; 11]. In Uzbekistan, the informatization of pedagogical processes and the professional competence of teachers have been studied by U.Sh.Begimkulov and N.A.Muslimov [12; 13]. However, the existing works do not treat the competence in creating AI elements as a separate pedagogical category, and neither its structure nor a methodology for its development has been elaborated. This gap defines the scientific problem of our research.

Research Methodology

The methodological basis of the research consists of the competence-based, activity-based and project-based approaches. The project-based approach draws on the ideas of learning through authentic problems substantiated by J.Krajcik and P.Blumenfeld [14]. The research used theoretical analysis, comparative analysis, systematization of concepts, pedagogical modelling, as well as observation and an expert survey conducted at Navoi State University.

Results and Discussion

1. Definition of the concept. In this research, an “AI element” is understood as a component of an AI system that can be designed and tested independently. These include a data collection and cleaning module, a feature engineering block, a classification or regression model, a neural network layer, a loss function and optimizer, evaluation metrics, the rule base of an expert system, and an interface that delivers model results to the user.

On this basis, the following original definition is proposed: **competence in creating AI elements** is an integrative personal and professional quality that expresses the readiness and ability of a future specialist to formulate a real problem as an AI task,

prepare data, design an AI element, implement it in software, evaluate its quality and apply it with ethical responsibility.

This definition differs from AI literacy in that its centre is the activity of creating rather than using. The student does not simply call a ready-made model but builds it, understanding each of its parts.

2. Structure of the competence. The competence consists of four interrelated components (Table 1).

Table 1. Components of the competence in creating AI elements

Component	Content	Key indicators
Motivational-value	Interest in creating AI, professional goals, ethical responsibility	Chooses a project independently; understands the social consequences of AI
Cognitive	Knowledge of the foundations of machine learning, statistics, linear algebra and optimization	Can explain the essence of algorithms; correctly identifies the type of problem
Operational-technological	Skills in working with tools such as Python, NumPy, pandas, scikit-learn and PyTorch	Prepares data; builds, trains and tunes a model
Reflective-project	Analysing own solution, identifying errors, defending the project	Evaluates the model using metrics; presents and justifies the result

The components are not hierarchical but systemically linked. The motivational component initiates the activity, the cognitive and operational-technological components carry it out, and the reflective-project component evaluates the result and generates new motivation for the next cycle.

3. Methodological model. The methodological model for developing the competence consists of target, content, process and outcome blocks. The target block derives from the state order and the professional standard. The content block is based on the integration of the courses “Fundamentals of Machine Learning”, “Artificial Intelligence and Expert Systems” and “Data Analysis”. The process block is implemented in four stages (Table 2).

Table 2. Stages of the process block of the methodological model

Stage	Aim	Forms and methods	Outcome
1. Motivational-orienting	Turning a real problem into an AI task	Problem-based lecture, case study, analysis of regional problems	Problem statement, project idea
2. Cognitive-instrumental	Mastering the essence of algorithms and the tools	"Writing from scratch" sessions: implementing an algorithm manually in NumPy first, then with a library	Understanding of the inner mechanism of the algorithm
3. Project-creative	Creating an AI element on authentic data	Small-group projects, collaboration via GitHub, Google Colab environment	A working AI element and a code repository
4. Reflective-evaluative	Evaluating and defending the result	Metric analysis, peer review, open defence	Project report, reflection journal

An important feature of the model is the use of authentic regional data. For example, using hydrological observation data of the Zarafshan River, students build a regression model that forecasts water discharge or a model that classifies the risk of water shortage. Unlike "clean" educational datasets, such data contain gaps, noise and seasonal variation, which require students to make real engineering decisions.

4. Levels of the competence. The outcome block contains criteria for assessing the levels of the competence (Table 3).

Table 3. Levels of development of the competence

Level	Description
Reproductive	Rebuilds a model from a ready-made example; finds it difficult to explain the effect of parameters
Partially exploratory	Independently selects and tunes an algorithm for a given problem; evaluates the result using metrics
Creative	Independently turns a real problem into an AI task; designs a new element and justifies its limitations and ethical aspects

The levels are assessed with a point system according to the indicators of each component. For this purpose, a set of test tasks, a project assessment rubric, code quality analysis and reflection journals is used.

The proposed structure differs from foreign AI literacy models in three respects. First, the models of D.Long and B.Magerko and of D.Touretzky are intended mainly for

school education and a broad audience [3; 4]. Our approach, by contrast, is aimed at professional training, that is, at a specialist who creates AI.

Second, the UNESCO framework defines the “create” level only in general terms and does not specify a methodology for reaching it [7]. The proposed model defines concrete stages, forms and methods, and assessment criteria for reaching this level. The “writing from scratch” principle is especially important: a student who first implements an algorithm manually then uses a library consciously and does not perceive AI as a “black box”.

Third, the use of authentic regional data connects learning with local problems. This develops the data-driven thinking emphasized by M.Tedre [6] and increases students’ professional motivation. Regional objects such as the Zarafshan basin show students the practical value of their work.

The model also has certain limitations. First, students differ in their mathematical preparation, which requires differentiated tasks at the cognitive-instrumental stage. Second, access to authentic data requires cooperation with industry organizations. Third, the teacher must have personal experience in creating AI elements.

Conclusion and Recommendations

The research led to the following conclusions:

1) in training future informatics specialists, it is necessary to move from the level of using AI to the level of creating AI elements, as required by the state strategy and the labour market;

2) the “competence in creating AI elements” is defined as an integrative quality expressing readiness to formulate a real problem as an AI task, prepare data, design an element, implement and evaluate it, and apply it responsibly;

3) the competence consists of motivational-value, cognitive, operational-technological and reflective-project components, which are systemically linked;

4) a methodological model consisting of target, content, process and outcome blocks has been developed; its process block includes four stages and relies on projects based on authentic regional data;

5) the reproductive, partially exploratory and creative levels of the competence and the tools for assessing them have been established.

Further research will test the effectiveness of the model through a pedagogical experiment and analyse the results using mathematical and statistical methods.

References:

[1] Resolution of the President of the Republic of Uzbekistan No. PQ-4996 “On measures to create conditions for the accelerated introduction of artificial intelligence technologies”. 17.02.2021. (In Uzbek)

[2] Resolution of the President of the Republic of Uzbekistan No. PQ-358 “On approval of the Strategy for the development of artificial intelligence technologies until 2030”. 14.10.2024. (In Uzbek)

[3] Long D., Magerko B. What is AI Literacy? Competencies and Design Considerations. Proceedings of the 2020 CHI Conference on Human Factors in Computing Systems, 2020, pp. 1–16. DOI: 10.1145/3313831.3376727.

[4] Touretzky D., Gardner-McCune C., Martin F., Seehorn D. Envisioning AI for K-12: What Should Every Child Know about AI? Proceedings of the AAAI Conference on Artificial Intelligence, 2019, vol. 33, no. 01, pp. 9795–9799.

[5] Ng D.T.K., Leung J.K.L., Chu S.K.W., Qiao M.S. Conceptualizing AI literacy: An exploratory review. Computers and Education: Artificial Intelligence, 2021, vol. 2, 100041.

[6] Tedre M., Toivonen T., Kahila J., Vartiainen H., Valtonen T., Jormanainen I., Pears A. Teaching Machine Learning in K–12 Classroom: Pedagogical and Technological Trajectories for Artificial Intelligence Education. IEEE Access, 2021, vol. 9, pp. 110558–110572.

[7] UNESCO. AI competency framework for students. Paris, UNESCO, 2024.

[8] Vuorikari R., Kluzer S., Punie Y. DigComp 2.2: The Digital Competence Framework for Citizens. Luxembourg, Publications Office of the European Union, 2022.

[9] Zawacki-Richter O., Marín V.I., Bond M., Gouverneur F. Systematic review of research on artificial intelligence applications in higher education – where are the educators? International Journal of Educational Technology in Higher Education, 2019, vol. 16, article 39.

[10] Zimnyaya I.A. Klyuchevye kompetentsii – novaya paradigma rezultata obrazovaniya [Key competences as a new paradigm of educational outcomes]. Vysshee obrazovanie segodnya, 2003, no. 5, pp. 34–42. (In Russian)

[11] Khutorskoy A.V. Klyuchevye kompetentsii kak komponent lichnostno-orientirovannoy paradigmy obrazovaniya [Key competences as a component of the student-centred paradigm of education]. Narodnoe obrazovanie, 2003, no. 2, pp. 58–64. (In Russian)

[12] Begimkulov U.Sh. Theory and practice of organizing and managing the informatization of pedagogical education processes. Doctoral dissertation (Pedagogy). Tashkent, 2007. (In Uzbek)

[13] Muslimov N.A., Usmonboyeva M.H., Sayfurov D.M., Turayev A.B. Innovative educational technologies. Tashkent, Sano-standart, 2015. (In Uzbek)

[14] Krajcik J.S., Blumenfeld P.C. Project-based learning. In: Sawyer R.K. (Ed.) The Cambridge Handbook of the Learning Sciences. Cambridge, Cambridge University Press, 2006, pp. 317–334.

Section 2. ACTUAL PROBLEMS IN MODERN TOURISM AND ECONOMICS

UDC: 911.3:338.46(575.12)

ASSESSING THE POTENTIAL FOR THE TERRITORIAL DEVELOPMENT OF SERVICE SECTORS IN THE SIRDARYO REGION

Altibayeva Muxayyo Begimqulovna
Associate Professor, Gulistan State University, Department of "Climate Change and Geoinformation Systems"
muhayyo.altibayeva@gmail.com

Annotatsiya: Sirdaryo viloyatida aholining o‘zini o‘zi band qilishida xizmat ko‘rsatish tarmoqlari o‘rni beqiyos. Ushbu jarayonni maydon birligi nisbatan kichik, ayniqsa, qulay iqtisodiy va transport geografik o‘rniga ega, aholi zichligi yuqori bo‘lgan hududda misolida ko‘rish mumkin. Sirdaryo viloyatida aholi bandligi, mehnat resurslarining shakllanishi va hududiy tarkibini takomillashtirishga yo‘naltirilgan chuqur ilmiy-tadqiqotlarni olib borish muhim ahamiyat kasb etadi.

Kalit so‘zlar: Xizmat turlari, hududiy tafovut, nomoddiy soha, yalpi hududiy mahsulot, oqilona foydalanish, muhofaza qilish, postindustrial.

Abstract. The role of services in self-employment of the population in the Syrdarya region is incomparable. This process can be seen in the example of an area with a relatively small area unit, especially with a favorable economic and transport geographical position, with a high population density. In the Syrdarya region, it is important to carry out in-depth research aimed at improving the employment of the population, the formation and territorial composition of labor resources

Key words: visual style, territorial difference, non-material sector, gross regional product, rational use, protection, post-industrial period.

Аннотация. Роль секторов обслуживания в самозанятости населения в Сырдарьинской области неоценима. Этот процесс можно проиллюстрировать на примере территории с высокой плотностью населения, где единица площади сравнительно невелика, особенно выгодно экономическое и транспортное географическое положение. В Сырдарьинской области важное значение

приобретает проведение углубленных научных исследований, направленных на улучшение занятости населения, формирования трудовых ресурсов и их территориальной структуры

Ключевые слова: Виды услуг, территориальные различия, нематериальный сектор, валовой региональный продукт, рациональное использование, защита, постиндустриальный период.

Introduction: On a global scale, geographical differences in service infrastructure are primarily closely linked to the level of natural, socio-economic development and demographic situation of the regions. While progress is the impetus for the development of many intangible industries, the demand of the population, which is their main consumer, increases the type of service offered as well as the number of producers. In research on such a topic, priority is given to carrying out an analysis of natural, economic, social, political, demographic, infrastructural factors that have a high impact on the territorial development of service networks, as well as improving the standard of living of the population, expanding the possibilities of the population to use services of modern and high quality.

In our republic, in recent years, a large-scale reform has been carried out on the territorial organization of services to the population and the development of new types of services, as well as increasing the employment level of the population. In particular, the new Uzbekistan development strategy for 2022-2026 sets the priorities for “development of the engineering and communication and social infrastructure system of Regions and the service and service sectors.” It is important to carry out in-depth research aimed at improving population employment, the formation and territorial composition of labor resources, especially in the Syrdarya region, which has a favorable economic and transport geographical position.

Leterature Review: Scientific geographical research work of territorial features of service areas, regional areas and mainly service areas M.Abramov, A.Alekseyev, S.Studied by such scientists as Kovalyov. In our republic, however, the areas of Service are studied relatively poorly geographically. In Uzbekistan, the areas of population

service are among the first geographically dissertation-level research work 1996 M.Territorial features of the Nazarov medical service, M. in 2021.Atajonov wore territorial features of social infrastructure. In 2024, M.Khidirov analyzed the problems of population employment in the field of services.

Research methodology: In the development of service networks in the cross-section of Regions, the priority is inextricably linked with the perfect planning of infrastructure elements in places. The activities of social sphere networks are constantly studied by the state and society. In particular, the assessment of medical services and educational opportunities by various social groups from the point of view of social justice assumes a clustered Organization of the activities of these networks by region. The expansion of the coverage of these industries largely depends on these factors:

- improvement of the territorial structure of the service infrastructure, based on the economic specialization of the regions;

- low funding and time required for people to attend service institutions;

- it is also necessary to create conditions for the recreation of the population, in which it is necessary to perfectly analyze the conditions and opportunities for improving the economic activities of the region.

The role of services in self-employment of the population in the Syrdarya region of our republic is incomparable. This process can be seen precisely on the example of providing transport services to the population. Boisi noted above that in the study, work and other tasks of the population to the regional center, it is possible to see mainly the high daily traffic regime, since the regional area is small, and the district centers to the Regional Center have a radius of 15 - 65 km, which necessitates the rapid development of passenger transport in the area.

Results and Discussion: Among service sectors, there is the advantage of household service, the possibility that each individual can organize for little money, depending on their own intellectual potential and interest. In this network, it is necessary to develop household services in the region, taking into account the greater possibility of self-employment of the population and a number of advantages. It should be noted that the existing household service facilities in the area, for example, catering outlets are

denser in regional and district centers. There are also beauty salons, sartoroshchas, shoe repair, among others.

The development of the domestic service sector in the region requires the creation of sufficient conditions and the creation of conditions below to increase the share of this sector in ensuring employment of the population:

- provision and improvement of household services networks by Regions;
- development of improving the quality of services in a way that meets certain requirements of the population;
- placement of domestic service institutions based on their geographical features and arming them with modern equipment;

-full use of the production forces, transport and system of services operating with the specialization of a large part of the population in the service sectors and adaptation to the market economy, ensuring standard and technical response of the created services, improving the management system of the industry and adapting it to the market economy;

-it consists in bringing the quality of household services in villages closer to the level of the city.

-The improvement of production potential is of great importance in the organization of household services to the population. The capacity and volumes of enterprises are related to the amount of adequate provision of services to the population. The development of these is due to the influence of the following factors:

- increasing the position of household service in self-employment of the population;
- improving the quality of services provided on the basis of a complex structure of household services;
- Creation of premises of domestic service institutions of a new type in a new type;
- determination of the maximum size of household service enterprises.

It should be noted that the increase and stabilization of the level of domestic services in the region will necessitate the improvement of the territorial characteristics

of this network on the basis of the development of small business and private entrepreneurship.

In recent years, the SWOT - analysis method has been widely used in scientific research. Using this method, it assumes the determination of the strengths, weaknesses, opportunities and threats of the territory under study As a result, the ways to achieve the competitiveness of this object are determined. This method can also be said to be an analysis - diagnosis method. The main thing is that the weak side and opportunities are also focused on it, the threat is definitely taken into account, and on this basis future prospects and development paths are also determined[3].

The SWOT analysis reveals that, while the Syrdarya region benefits from a favorable transport-geographical location including the significance of the road network connecting the country's various regions the roadside infrastructure remains inadequate. Furthermore, the proximity of district centers to the regional capital, and the short distances between them, mean that the population's demand for various types of services is met primarily through the regional center. This indicates that the districts are lagging behind the regional center in terms of living and working conditions. The region's limited endowment of mineral resources restricted primarily to raw materials for construction constrains the development of the manufacturing industry. Furthermore, a range of challenges regarding employment arises from several factors: the inefficient use of labor resources, high levels of outward labor migration, underdeveloped roadside service infrastructure, a lack of budgetary funds for the development of this sector, a scarcity of innovative solutions for the commercialization of infrastructure, relatively low investor activity, and a failure to effectively capitalize on investment opportunities.

In developing the socio-economic development forecast for the region, it is essential to minimize, as much as possible, the regional disparities within the service sectors. This requires making effective use of the unique geographical locations of the Sardoba and Oqoltin districts. For instance, the daily traffic volume on the M-39 and A-373 highways passing through the Oqoltin district reaches 32,492 vehicles. Such figures serve as a key factor in the establishment and development of various types of services. Yet, along this road which is of national significance one finds only fuel stations.

Table 1.

	Strength	**Weak point**	
Geographical location	Favorable transport-geographical location, the significance of the road connecting the republic's regions, the proximity of district centers to the regional center, and the short distances between them.	The impact of proximity to the republic's center on the territorial mobility of the labor force toward the capital.	**Geographical location**
Natural resources	Availability of favorable agro-climatic resources. Good provision of water resources, and the existence of conditions suitable for agrotourism.	High levels of soil salinity in the region. Among raw material resources, only construction materials are available.	**Natural resources**
Labor resources	A steady increase in the number of labor resources in the region. The existence of opportunities for developing service sectors.	Inefficient use of labor resources and high levels of outward labor migration.	**Labor resources**
Innovative activity	The existence of opportunities for the innovative development of service infrastructure in the region.	A lack of innovative developments in the commercialization of infrastructure.	**Innovative activity**
Investment activity	The existence of a favorable investment climate, as well as targeted programs and roadmaps.	Relatively low level of investor activity; failure to effectively utilize investment opportunities.	**Investment activity**
	Opportunity	**Opportunity**	
Ecotourism potential	The fact that tourism is a highly profitable sector, the presence of recreational resources and sites of historical significance in the region, and the existence of opportunities to develop cultural tourism and riverside ecotourism.	Ecological interventions, the degradation of the riparian ecosystem, and the impact on the balance of the *tugai* (riparian forest) landscape.	**Ecotourism potential**
Innovative activity	The growing need for innovation within state institutions and enterprises with state participation, and the availability of innovative opportunities for developing service infrastructure.	The relatively limited number of state measures to support innovative entrepreneurship.	**Innovative activity**
Demographic development	Relatively high birth rates, an increasing share of young people, a rise in the number of employed individuals, and improvements in the living conditions of the population in the regions.	The presence of unresolved problems in the local labor market, the low level of participation of the bulk of the labor force in economic sectors, and a high proportion of the population living in low-income conditions.	**Demographic development**
Investment activity	The existence of opportunities to enhance the region's investment attractiveness and develop service infrastructure by leveraging its favorable geographical location and conditions.	Low level of investor activity; failure to properly utilize the investment environment.	**Investment activity**

Conclusion and Recommendations: It should be particularly noted that the region's natural ecological condition is a primary factor negatively affecting the operations of this sector. The high water table with groundwater located close to the surface combined with inadequate sewage infrastructure, has given rise to a number of problems in the region that await resolution.

Given the ecological conditions of the Syrdarya region, special attention should be paid to the following issues when improving the territorial structure of service infrastructure:

- enhancing the provision of sewage networks in residential areas based on the natural ecological conditions and socio-demographic characteristics of these territories as well as developing and implementing new model projects for sanitation and public utility facilities.

- There are numerous unresolved issues regarding the provision of sewage systems in multi-story residential buildingsconstructed based on model designs in the regional center (Guliston) and district centers. Given the high demand for utility services in the region, it is essential to expand the utility infrastructure as much as possible to address these challenges.

- Develop and expand agrotourism by leveraging the region's agro-climatic resources specifically in areas with high soil salinity to cultivate melons (including the famous Syrdarya melons, renowned throughout the republic).

References

[1]. Item 2 of the Development Strategy of the Republic of Uzbekistan for 2022–2026.

[2]. Altibayeva M.B., Madrahimova Z.N., Umrzaqov O.A. “Research on Sectoral and Territorial Approaches in Economic Geography” (Monograph), approved by the Scientific Council of GulSU (Gulistan State University), Protocol No. 10, dated May 29, 2023.

[3]. Safarova N.I., Altibayeva M.B., Toymbayeva D.A., Territorial Development of Service Sectors in Uzbekistan (The Case of Sirdaryo Region). “O‘zbekiston zamini” [Land of Uzbekistan] Scientific-Practical and Innovative Journal, 4/2022, pp. 97–99.

[4]. Safarova N.I., Safarov U.H., Service Sectors in the Republic of Uzbekistan and Territorial Disparities in Their Development. Bulletin of Tashkent State Pedagogical University, Tashkent, 2021, No. 11, pp. 156–164.

[5]. Shadibekova D.A., Developing the Service Sector in Uzbekistan: Problems and Solutions. Monograph, Tashkent, 2020, pp. 8–9.

[6]. Soliyev A.S., Nazarov M.I., Qurbonov Sh.B., Socio-Economic Development of the Regions of Uzbekistan. Monograph, Tashkent, Mumtoz So‘z, 2010.

Section 3. ACRUAL PROBLEMS IN MODERN TECHNICAL SCIENCES

UDC: 004.056.5:004.85

ADAPTIVE DETECTION OF SPAM IN UZBEK-LANGUAGE MESSAGES: EVALUATION UNDER DATA-PROVENANCE SHIFT AND DRIFT-TRIGGERED RETRAINING

Atajonov Muzaffar Ne'matjon o'g'li
Teacher of Informatics, Jaloliddin Manguberdi Military Academic Lyceum, Uzbekistan
Muzaffar19910627@gmail.com

Annotatsiya. O'zbek tilidagi xabarlarda spamni aniqlash tekshirilgan korpuslarning yetishmasligi va spam usullarining o'zgarishi tufayli murakkab. 8 203 xabarli korpus tahlil qilinib (67,8 foizi sintetik, bosqichli yoki tarjima; barcha spam shu guruhlarda), moslashuvchan detektor taklif etildi: o'zbek matnini normallashtirish, TF-IDF va 16 ta struktur belgi, stacking ansambli (LR, NB, SVM; LightGBM meta-o'rganuvchi) va DDM/EDDM bilan qayta o'qitish. Tasodifiy bo'lishda to'qqiz modelning barchasi F1 > 0,99 beradi (stacking 0,9993), biroq tarjima qilingan xabarlarda F1 0,27–0,58 ga tushadi. Rejim o'zgarganda 200 ta yorliqli xabar bilan DDM orqali qayta o'qitish oxirgi 500 xabarda F1 ni 0,397 dan 0,966 ga oshiradi va davriy qayta o'qitish natijasini 7,5 baravar kam yorliq bilan beradi.

Kalit so'zlar: *spamni aniqlash; o'zbek tili; stacking; kontseptual dreyf; DDM; EDDM.*

Аннотация. Обнаружение спама в узбекских сообщениях затруднено нехваткой проверенных корпусов и изменением приёмов спамеров. Проанализирован корпус из 8 203 сообщений (67,8 % синтетические, поэтапно сгенерированные или переведённые; весь спам — в этих группах) и предложен адаптивный детектор: нормализация узбекского текста, TF-IDF и 16 структурных признаков, стековый ансамбль (LR, NB, SVM; мета-обучающийся LightGBM) и переобучение по сигналу DDM/EDDM. При случайном разбиении все девять моделей дают F1 > 0,99 (ансамбль — 0,9993), но на переведённых сообщениях F1 снижается до 0,27–0,58. После смены режима переобучение по

DDM на 200 размеченных сообщениях повышает F1 на последних 500 сообщениях с 0,397 до 0,966 и даёт результат периодического переобучения при в 7,5 раза меньшей разметке.

Ключевые слова: *обнаружение спама; узбекский язык; стековый ансамбль; дрейф концепции; DDM; EDDM.*

Abstract. Spam filtering for Uzbek messages is hampered by scarce verified corpora and changing spam tactics. We audit an 8,203-message corpus (67.8% synthetic, staged or translated; all spam in these groups) and propose an adaptive detector: Uzbek text normalization, TF-IDF with 16 structural features, a stacked ensemble (LR, NB, SVM; LightGBM meta-learner) and DDM/EDDM-triggered retraining. On a random split all nine models exceed 0.99 F1 (stack 0.9993), but on held-out translated messages F1 falls to 0.27–0.58. After a regime change, DDM-triggered retraining on 200 labelled messages raises F1 on the last 500 messages from 0.397 to 0.966, matching periodic retraining with 7.5 times fewer labels.

Key words: *spam detection; Uzbek language; stacked ensemble; concept drift; DDM; EDDM.*

Introduction

Unwanted messages remain a main carrier of fraud and phishing. In Uzbekistan the problem is amplified by the parallel use of Latin and Cyrillic alphabets, mixed Uzbek–Russian text and deliberate obfuscation of words. Filters for English-language e-mail and SMS are mature [2]–[4], and fine-tuned transformers report accuracies around 0.996 on a combined public corpus [6]. For low-resource languages datasets are small and often mix collected, generated and translated text [7], [8], so two questions are rarely asked together: how trustworthy is the evaluation, and how does a deployed filter keep up when spam changes? This paper addresses both on an Uzbek corpus collected by the author. Its contributions are: (i) a provenance audit showing that 67.8% of messages are synthetic, staged or translated, that all spam belongs to these groups and that a label-revealing field

was present in 400 messages; (ii) a pipeline with Uzbek normalization, 16 structural features and a stacked ensemble, compared with eight other models; (iii) an evaluation under provenance shift with ROC/PR analysis, learning curves and exact significance tests; and (iv) drift-triggered retraining with explicit thresholds and label budget (DDM, EDDM).

Literature Review

Early filters were probabilistic: Sahami et al. showed that a Bayesian model of message text separates junk from legitimate e-mail [2], and Cormack and Dada et al. systematised filtering methods and open problems, among them the change of spam characteristics over time [3], [4]. Boosted trees such as LightGBM [13] and stacked generalisation [12] are now standard components. Jamal et al. fine-tuned BERT-family models for phishing and spam e-mail with consistent gains [5]; Asliyuksek et al. combined DistilBERT with structural features on 81,586 e-mails and found that all models degraded on modern spam, the transformer least, calling for continually learning systems [6]. For low-resource languages, BangalaBarta offers 2,772 Bangla messages in normal, promotional and smishing classes [7], and Kuriyozov et al. released text-classification resources for Uzbek [8]; an earlier study by the author addressed spam detection with artificial intelligence [1]. Most such works use a random split of one corpus. Concept drift is central because senders adapt to filters [11]: the Drift Detection Method (DDM) signals a warning and a drift when the online error rate rises significantly above its minimum [9], and the Early Drift Detection Method (EDDM) uses the distance between consecutive errors [10]. Published studies rarely state how many labelled messages must be collected before retraining; this budget is studied here. Authentication standards (SPF, DKIM, DMARC) need message headers that this corpus lacks and are left for future work.

Data. The corpus contains 8,203 Uzbek messages (3,819 spam, 46.6%; 4,384 legitimate) with a text, a binary label, a source field and an annotation note. From the notes and subset names each message was assigned to a provenance group (Table 1): synthetic (“Sintetik …”); four subsets named after construction stages (marketing_stage2,

daily_stage3, phishing_stage4, gmail_style_stage5); translated ("tarjima"); and the rest, called collected-style because nothing in its annotation marks it as generated or translated.

Table 1. Composition of the corpus by provenance group

Provenance group	Source / annotation	Legit.	Spam	Total	%
Collected-style	SMS, e-mail, Telegram, bank/service notices, personal	2,644	0	2,644	32.2
Synthetic	"Sintetik" spam SMS, e-mail, Telegram, web ads	0	2,039	2,039	24.9
Staged subsets	marketing_stage2, daily_stage3, phishing_stage4, gmail_style_stage5	1,150	1,250	2,400	29.3
Translated	"tarjima" (chat-style messages and SMS)	590	530	1,120	13.7
Total		**4,384**	**3,819**	**8,203**	**100**

No spam message belongs to the collected-style group, so a classifier could separate the classes by generator style; a model that sees only the source field reaches accuracy 0.630. Four problems were handled: (i) in 400 e-mail-format messages a line "Turi: email-spam/email-nospam" states the class and was removed together with "Ref:" lines; (ii) four exact duplicates were removed (8,199 messages remain); (iii) after normalization 25.0% of messages equal an earlier one and 46.8% have a near-duplicate (character-n-gram cosine ≥ 0.9); (iv) the notes show that the corpus is not a sample of natural traffic. A random split therefore puts near-identical templates into both training and test sets.

Research Methodology

Figure 1 shows the pipeline: a message is normalised, converted to TF-IDF vectors and structural features, and classified by a stacked ensemble; the error stream feeds a drift detector that starts label collection and retraining. Normalization (Eq. 1) composes four operators: ν unifies apostrophes and lower-cases; τ removes emoji and repeated punctuation; ω transliterates Cyrillic to Uzbek Latin (қ → q, ғ → g‘, ў → o‘); ρ repairs obfuscation (a.k.s.i.y.a → aksiya; 1→i, 0→o, 3→e, 4→a, @→a inside words; letter runs ≥ 3 shortened) and replaces numbers by 0. With $f_{t,j}$ the count of term j in message t, n training messages and n_j containing term j, TF-IDF weights are computed with sublinear term

frequency and smoothed inverse document frequency and L2-normalised (Eq. 2); word 1–2-grams and character 2–5-grams give x^w_t and x^c_t, and $z_t = [x^w_t; x^c_t]$.

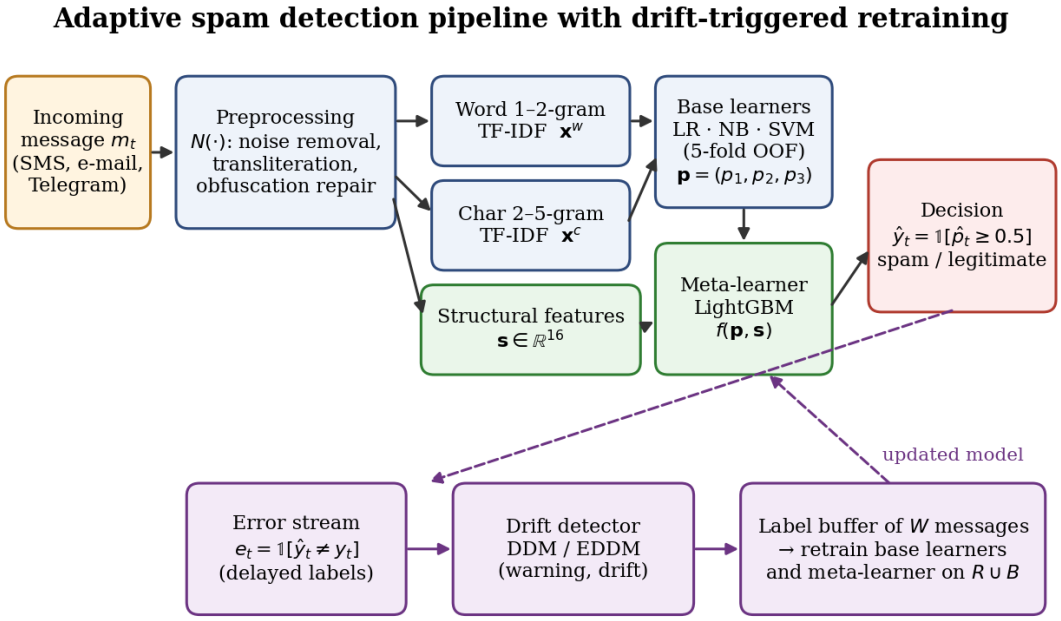


Figure 1. Architecture and data flow of the adaptive spam detection pipeline.

$$\tilde{m}_t = \mathcal{N}(m_t) = (\rho \circ \omega \circ \tau \circ \nu)(m_t) \qquad (1)$$

The structural vector $s_t \in$ R^16 holds the logarithms of message length in characters and words; the shares of digits, upper-case letters, punctuation and Cyrillic letters; the counts of "!", "?" and [link]; the presence of "@"; the number of long digit sequences, letter runs and tokens mixing letters with digits; a currency mention; a header-style line; and the mean word length.

$$w_{t,j} = \left(1 + \ln f_{t,j}\right)\left(\ln \frac{1+n}{1+n_j} + 1\right) \quad \mathbf{x}_t = \frac{\mathbf{w_t}}{\|\mathbf{w_t}\|_2} \qquad (2)$$

Three base learners give spam probabilities p = (p_1, p_2, p_3) (Eq. 3): logistic regression on z_t (C = 10), multinomial naive Bayes on x^w_t and a Platt-calibrated linear SVM on z_t. To prevent leakage the meta-learner is trained on out-of-fold probabilities from five stratified folds, after which the base learners are refitted on all training data. A LightGBM meta-learner (300 trees, 15 leaves, learning rate 0.05) maps (p, s_t) to the final probability (Eq. 4). The comparison models are naive Bayes, logistic regression, linear SVM, random

forest (300 trees), XGBoost (300 trees, depth 6), LightGBM (400 trees), CatBoost (500 iterations, depth 6) and an MLP (256 hidden units); seed 42, scikit-learn 1.8.0, LightGBM 4.7.0, XGBoost 3.4.1, CatBoost 1.2.10.

$$p_1 = \sigma(\mathbf{u}^\top \mathbf{z} + b),\ p_2 = \frac{P(y=1)\prod_j P(j|1)^{x_j}}{\sum_{c\in\{0,1\}} P(y=c)\prod_j P(j|c)^{x_j}},\quad p_3 = \sigma(Ag(\mathbf{z}) + B) \qquad (3)$$

$$\hat{p}_t = f_\theta(p_1, p_2, p_3, \mathbf{s}_t) \quad \hat{y}_t = \mathbf{1}[\hat{p}_t \geq 0.5] \qquad (4)$$

Let $e_t = 1[\hat{y}_t \neq y_t]$ be the error once the label arrives. DDM tracks the error rate with a Laplace correction (Eq. 5), without which one error after an error-free period would raise a false alarm. After 30 messages it stores the minimum of $\pi_t + \sigma_t$ as (π_{min}, σ_{min}) and applies the thresholds of Eq. 6 (k_w = 2, k_d = 3). EDDM computes from the distances between consecutive errors the ratio r_t of Eq. 7 and signals a warning below α = 0.95 and a drift below β = 0.90 after at least 30 errors.

$$\pi_t = \frac{e_t+1}{n_t+2} \quad \sigma_t = \sqrt{\frac{\pi_t(1-\pi_t)}{n_t}} \qquad (5)$$

$$\pi_t + \sigma_t \geq \pi_{\min} + k_w\sigma_{\min}\ \text{(warning)},\quad \pi_t + \sigma_t \geq \pi_{\min} + k_d\sigma_{\min}\ \text{(drift)} \qquad (6)$$

$$r_t = \frac{\bar{d}_t + 2s_{d,t}}{\max_{\tau\leq t}(\bar{d}_\tau + 2s_{d,\tau})},\quad r_t < \alpha\ \text{(warning)}\quad r_t < \beta\ \text{(drift)} \qquad (7)$$

Algorithm 1 states the policy: after a drift signal at t_d the next W = 200 messages are labelled (the label budget), then the base learners and the meta-learner are refitted on R ∪ B (R is the training set, B the buffer) and the detector is reset. The periodic baseline retrains every 200 messages on R and all labelled messages seen so far; the oracle retrains once at the true change point. Protocol A is a stratified 80/20 split of the deduplicated corpus (6,559 training, 1,640 test messages, 764 spam). Protocol B withholds one provenance group at a time; the five groups with both classes (translated, phishing_stage4, marketing_stage2, daily_stage3, gmail_style_stage5) are scored by F1, and two stress tests withhold all synthetic spam (recall) or all collected-style legitimate messages (specificity). Protocol C

is a stream of 800 in-distribution messages followed by the 1,116 translated messages, which the model has never seen, in five random orders; it is a controlled regime change defined by provenance, not a record of spam evolution in time.

Algorithm 1. Drift-triggered retraining

```
Input: model M trained on R; detector D (DDM or EDDM); budget
W
1 for t = 1, 2, … do
2 output ŷ_t ← M(m_t);  when y_t arrives: e_t ← 1[ŷ_t ≠ y_t]
3 if not collecting then  state ← D.update(e_t)
4 if state = drift then  t_d ← t;  collecting ← true
5 if collecting and t = t_d + W then
6 B ← {(m_i, y_i): t_d < i ≤ t_d + W};  M ← fit(R ∪ B);
D.reset();  collecting ← false
```

We report accuracy, precision, recall, F1 of the spam class, ROC-AUC and PR-AUC (the PR curve is more informative for unbalanced classes [14]), 95% bootstrap intervals for F1 and the exact McNemar test [15]; for the stream, post-change F1, tail F1 (last 500 messages), retrainings, labels used, detection delay and false alarms.

Results and Discussion

Random split. All models are near the ceiling (Table 2). The stack reaches F1 = 0.9993 (one false positive, no false negative), logistic regression 0.9987, linear SVM and LightGBM 0.9980; the weakest models reach 0.9915. ROC and PR curves coincide except in the extreme corner (Figure 2a, b). McNemar's test does not separate the stack from logistic regression (p = 1.00), linear SVM or LightGBM (p = 0.63); only the MLP differs significantly (p = 0.012). F1 rises Provenance shift. When a group is withheld the picture changes (Table 3). On the translated subset F1 lies between 0.265 and 0.580 and accuracy between 0.586 and 0.704, although the same models exceed 0.99 on the random split. Logistic regression, linear SVM and CatBoost still rank messages reasonably (ROC-AUC 0.84–0.85, Figure 2c, d) but their threshold misclassifies most new messages; the other

models have ROC-AUC of 0.65–0.68. from 0.954–0.978 with 5% of the training data to 0.998–0.999 with all of it (Figure 3b).

Table 2. Random stratified split (n = 1,640; 764 spam)

Model	Acc.	Prec.	Rec.	F1	F1, 95% CI	ROC-AUC	PR-AUC
Naive Bayes	0.9921	0.9908	0.9921	0.9915	0.986–0.996	0.9995	0.9995
Logistic regression	0.9988	0.9987	0.9987	0.9987	0.997–1.000	1.0000	1.0000
Linear SVM	0.9982	0.9974	0.9987	0.9980	0.996–1.000	1.0000	1.0000
Random forest	0.9927	0.9883	0.9961	0.9922	0.988–0.997	0.9999	0.9999
XGBoost	0.9921	0.9934	0.9895	0.9915	0.987–0.996	0.9996	0.9996
LightGBM	0.9982	0.9987	0.9974	0.9980	0.995–1.000	0.9999	0.9999
CatBoost	0.9921	0.9947	0.9882	0.9915	0.987–0.996	0.9996	0.9996
MLP	0.9939	0.9961	0.9908	0.9934	0.989–0.997	0.9999	0.9999
Proposed stack	0.9994	0.9987	1.0000	0.9993	0.998–1.000	1.0000	1.0000

The stack has the highest F1 (0.580) and is right more often than logistic regression where they disagree (93 vs 15 cases, $p < 10^{-14}$), but its ranking is weaker (ROC-AUC 0.679 vs 0.849), so part of its advantage is threshold calibration. More training data does not close the gap: F1 on the translated subset stays between 0.28 and 0.43 for all training sizes (Figure 3c). Macro-F1 ranges from 0.626 (XGBoost) to 0.896 (stack). In the stress tests the models recognise only 3–32% of synthetic spam without it, and 19–58% of collected-style legitimate messages: unfamiliar style is treated as evidence for the other class. Ablation. On the random split normalization raises the F1 of logistic regression from 0.9934 to 0.9987, and the structural features alone reach F1 = 0.894 but add little to the stack (0.9974 without, 0.9993 with). Under shift the effects are unfavourable: logistic regression on raw lower-cased text scores higher on the translated subset (F1 0.508, ROC-AUC 0.872) than on normalized text (0.405, 0.849), and removing the structural features does not hurt the stack (F1 0.592 vs 0.580). The normalization rules and structural features thus seem to capture regularities of the generated messages, and we do not claim that they improve robustness here. Drift-triggered retraining. Before the change the model is almost error-free (accuracy 0.999 on 800 messages); afterwards a static model stays at F1 = 0.398 (Table 4, Figure 4). DDM signals drift after 4.8 messages on average (range 2–10), EDDM after 80.6 because it needs 30 errors.

Table 3. F1 of the spam class when one provenance group is withheld (groups of 1,116, 700, 600, 700 and 400 messages); last two columns: stress tests

Model	Transl.	phish.	market.	daily	gmail	Macro F1	AUC (transl.)	Recall synth.	Spec. coll.
Naive Bayes	0.557	0.994	0.824	1.000	0.974	0.870	0.662	0.228	0.515
Logistic regression	0.405	0.942	0.932	1.000	1.000	0.856	0.849	0.144	0.564
Linear SVM	0.433	0.943	0.986	1.000	0.997	0.872	0.852	0.157	0.583
Random forest	0.443	0.874	0.578	1.000	0.741	0.727	0.818	0.060	0.238
XGBoost	0.324	0.455	0.895	0.750	0.704	0.626	0.651	0.082	0.190
LightGBM	0.308	0.748	0.882	0.889	0.867	0.739	0.683	0.073	0.276
CatBoost	0.265	0.801	0.867	0.750	0.893	0.715	0.841	0.029	0.401
Proposed stack	**0.580**	**0.996**	**0.945**	**1.000**	**0.958**	**0.896**	**0.679**	**0.317**	**0.568**

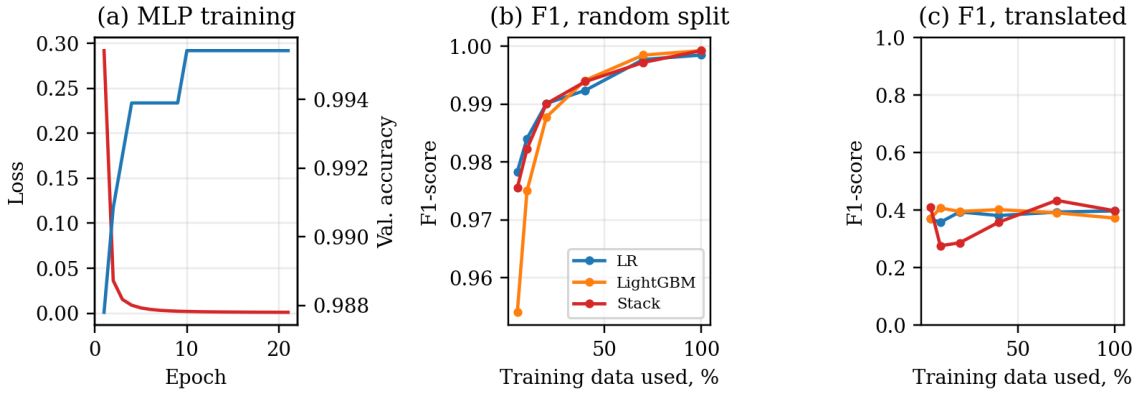


Figure 3. Learning dynamics: (a) MLP loss and validation accuracy; F1 on (b) the random-split test set and (c) the translated subset versus the share of training data.

Neither gave a false alarm before the change, nor in a control stream of 1,416 in-distribution messages. DDM-triggered retraining attains the post-change F1 of periodic retraining (0.891) with 240 labelled messages on average instead of 1,800 (7.5 times fewer) and is close to the oracle (0.896); periodic retraining reaches a higher tail F1 (0.986 vs

0.966) because it keeps adding labels, and EDDM adapts later (0.863). With W = 100 the detector fired twice and post-change F1 rose to 0.936; with W = 400 it fell to 0.825 because the first 400 messages are classified by the outdated model; lowering k_d to 2.5 advanced the signal by one message. A budget of 100–200 labelled messages is a reasonable start when the pre-change error rate is below 1%.

Limitations

By the corpus's own annotations about two thirds of the messages are synthetic, staged or translated and all spam belongs to these groups; the results describe the methods on this corpus, not on live Uzbek traffic, and the near-perfect random-split accuracy reflects redundancy. The stream simulates a regime change, not gradual evolution, and ignores label delay. Transformers were not trained and hyperparameters were set once. Header evidence (SPF, DKIM, DMARC) requires full messages and is future work; a held-out set of genuinely collected spam is the most important next step.

Conclusion and Recommendations

On a random split all nine models reach F1 above 0.99 and the stacked ensemble is best (0.9993), but the split is dominated by templated near-duplicates. When a provenance group is withheld F1 on translated messages falls to 0.27–0.58, and normalization and structural features do not improve robustness. DDM-triggered retraining with 200 labelled messages detects the change after 4.8 messages, raises F1 on the last 500 messages from 0.397 to 0.966 and matches periodic retraining with 7.5 times fewer labels. Uzbek spam filters should therefore be evaluated with an origin-controlled protocol, label-bearing fields and template duplicates removed before splitting, and an error-rate drift detector with a budget of 100–200 labels deployed. Data availability: the annotated corpus and code can be provided by the corresponding author on reasonable request. Conflict of interest: none declared.

References:

[1] Normatov I.X., Atajonov M.N. Suniy intellekt yordamida spamni aniqlash jarayoni // Educational Research in Universal Sciences. – 2024. – Vol. 3, Special Issue 2. – P. 262–266.

[2] Sahami M., Dumais S., Heckerman D., Horvitz E. A Bayesian approach to filtering junk e-mail // AAAI-98 Workshop on Learning for Text Categorization. – 1998. – P. 55–62.

[3] Cormack G.V. Email spam filtering: a systematic review // Foundations and Trends in Information Retrieval. – 2008. – Vol. 1, No. 4. – P. 335–455.

[4] Dada E.G., Bassi J.S., Chiroma H., et al. Machine learning for email spam filtering: review, approaches and open research problems // Heliyon. – 2019. – Vol. 5, No. 6. – e01802.

[5] Jamal S., Wimmer H., Sarker I.H. An improved transformer-based model for detecting phishing, spam and ham emails: A large language model approach // Security and Privacy. – 2024. – Vol. 7, No. 5. – e402. DOI: 10.1002/spy2.402.

[6] Asliyuksek H., Tonkal Ö., Kocaoglu R. A comparative evaluation of a multimodal approach for spam email classification using DistilBERT and structural features // Electronics. – 2025. – Vol. 14, No. 19. – Art. 3855. DOI: 10.3390/electronics14193855.

[7] Shahriyar M.F., Tanbhir G. BanglaBarta: A benchmark dataset for spam and smishing SMS detection in mobile communication // 2024 13th Int. Conf. on Electrical and Computer Engineering (ICECE). – IEEE, 2024. – P. 57–62.

[8] Kuriyozov E., Salaev U., Matlatipov S., Gómez-Rodríguez C. Text classification dataset and analysis for Uzbek language // arXiv:2302.14494. – 2023.

[9] Gama J., Medas P., Castillo G., Rodrigues P. Learning with drift detection // Advances in Artificial Intelligence – SBIA 2004, LNCS 3171. – Springer, 2004. – P. 286–295.

[10] Baena-García M., del Campo-Ávila J., Fidalgo R., Bifet A., Gavaldà R., Morales-Bueno R. Early drift detection method // 4th Int. Workshop on Knowledge Discovery from Data Streams. – 2006. – P. 77–86.

[11] Lu J., Liu A., Dong F., Gu F., Gama J., Zhang G. Learning under concept drift: A review // IEEE Transactions on Knowledge and Data Engineering. – 2019. – Vol. 31, No. 12. – P. 2346–2363.

[12] Wolpert D.H. Stacked generalization // Neural Networks. – 1992. – Vol. 5, No. 2. – P. 241–259.

[13] Ke G., Meng Q., Finley T., et al. LightGBM: A highly efficient gradient boosting decision tree // Advances in Neural Information Processing Systems 30. – 2017. – P. 3146–3154.

[14] Saito T., Rehmsmeier M. The precision-recall plot is more informative than the ROC plot when evaluating binary classifiers on imbalanced datasets // PLoS ONE. – 2015. – Vol. 10, No. 3. – e0118432.

[15] Dietterich T.G. Approximate statistical tests for comparing supervised classification learning algorithms // Neural Computation. – 1998. – Vol. 10, No. 7. – P. 1895–1923.

UDC: 621.391.8:519.876.5

EVALUATING THE SURVIVAL OF HYBRID TELECOMMUNICATION NETWORKS CONSIDERING COMMON CAUSED FAULTS AND PHYSICAL RESOURCE LIMITS

Matyokubov Utkir Karimovich
PhD, docent, Urgench State University named after Abu Rayhan Biruni,
otkir_matyokubov89@mail.ru
Davronbekov Dilmurod Abdujalilovich
DSc, professor, t University of Information Technologies named after Muhammad al-Khwarizmi,
d.davronbekov@gmail.com
Muradov Muhammad Murod ugli
PhD, docent, Urgench State University named after Abu Rayhan Biruni
muradov.muhammad1414@gmail.com

Annotatsiya. Gibrid telekommunikatsiya tarmog‘ining uzatish, hisoblash va xizmat segmentlari o‘rtasidagi bog‘lanishlar tadqiq etildi. Tadqiqotning maqsadi yashovchanligini baholashda va tiklash chora-tadbirlarini tanlashda qaysi bog‘liqliklarni saqlash zarurligini aniqlashdan iborat. Ilmiy ishlar, arxitektura hujjatlari va e’lon qilingan patentlarning predmetli tahlili o‘tkazilib, baholash obyekti, hisobga olinadigan resurslar va tekshiriladigan texnik natija solishtirildi. Birlamchi buzilish sabablaridan xizmat ko‘rsatish shartlariga o‘tish sxemasi taklif etildi; unda mantiqiy ulanishlar qo‘shimcha fizik resurs hosil qilmaydi. Ikki zaxira yo‘lli analitik misolda umumiy sababni mustaqil uzilishlar bilan almashtirish xizmat ko‘rsatish ehtimolini oshirib ko‘rsatishi isbotlandi: ortiqcha baholash $\Delta = q(1-q)(1-p_1)(1-p_2)$ ifodasi bilan aniqlanadi (asosiy holatda 0,0094; mustaqil modelda uzilish ehtimoli taxminan 8,95 marta kam baholanadi). Besh segmentli modelli tajribada (30 takror, har birida 10^6 sinov; natijalar aniq sanab chiqish bilan tasdiqlandi) xizmatning ko‘rsatilmaslik ehtimoli mustaqil modelda 0,51 %, umumiy sabab hisobga olinganda

2,15 %, sig‘im cheklovi qo‘shilganda 3,91 %, energiya va vaqt bo‘yicha o‘tish jarayoni qo‘shilganda 4,28 % bo‘ldi. Natijalar tiklash xotirasi, sifatni tasdiqlash, energetik joizlik va bashoratli boshqarishga qo‘yiladigan talablarni asoslaydi. Hisoblashlar modelli ma’lumotlarda bajarilgan.

Kalit so‘zlar: *gibrid tarmoq; yashovchanlik; umumiy sabab bilan uzilish; fizik resurs; muhim xizmat; Monte-Karlo usuli.*

Аннотация. Исследованы связи между передаточным, вычислительным и сервисным сегментами гибридной телекоммуникационной сети. Целью исследования является определение зависимостей, которые необходимо сохранить при оценке выживаемости и выборе восстановительных мероприятий. Проведен предметный анализ научных работ, архитектурной документации и опубликованных патентов, сопоставлен объект оценки, учитываемые ресурсы и проверяемый технический результат. Предложена схема перехода от первичных причин отказа к условиям обслуживания, в которой логические соединения не создают дополнительного физического ресурса. В аналитическом примере с двумя резервными путями доказано, что замена общей причины независимыми отключениями повышает вероятность оказания услуг: переоценка определяется выражением $\Delta=q\,(1-q)\,(1-p_1)\,(1-p_2)$ (в основном случае 0,0094; в независимой модели вероятность отключения оценивается примерно в 8,95 раза меньше). В пятисегментном модельном эксперименте (30 повторений, по 10^6 испытаний в каждом; результаты подтверждены точным подсчетом) вероятность непредоставления услуги в независимой модели составила 0,51%, с учетом общей причины - 2,15%, с учетом ограничения емкости - 3,91%, с учетом процесса перехода по энергии и времени - 4,28%. Результаты обосновывают требования к восстановительной памяти, подтверждению качества, энергетической допустимости и прогнозному управлению. Расчеты выполнены на модельных данных.

Ключевые слова: *гибридная сеть; жизнеспособность; разрыв по общей причине; физический ресурс; важная услуга; Метод Монте-Карло.*

Abstract. The connections between the transmission, computing, and service segments of a hybrid telecommunications network were investigated. The aim of the study is to determine which dependencies should be maintained when assessing survival and selecting recovery measures. A substantive analysis of scientific works, architectural documentation, and published patents was conducted, comparing the valuation object, the resources taken into account, and the technical result being verified. A scheme for transitioning from primary failure causes to service conditions is proposed, where logical connections do not generate additional physical resources. In the analytical example with two backup paths, it was proven that replacing the general cause with independent interruptions increases the probability of service delivery: the overestimation is determined by the expression $\Delta=q\ (1-q)\ (1-p_1)\ (1-p_2)$ (in the main case, 0.0094; in the independent model, the probability of interruption is estimated to be approximately 8.95 times lower). In the five-segment model experiment (30 repetitions, 10^6 trials in each; results were confirmed by precise counting), the probability of the service not being provided was 0.51% in the independent model, 2.15% taking into account the general cause, 3.91% when the capacity limit was added, and 4.28% when the energy and time transition process was added. The results justify the requirements for recovery memory, quality assurance, energy permissibility, and predictive control. Calculations were performed on model data.

Keywords: *hybrid network, viability, interruption due to a common cause, physical resource, critical service, Monte Carlo method.*

Introduction

The development of digital services increases the user's dependence on the coordinated operation of the transmission network, computing, and software functions. The

International Telecommunication Union's (ITU) “Facts and Figures 2025” report notes a growing use of digital services [1]. Such data reflects the scale of infrastructure use, but does not determine the frequency of outages and does not replace operational logs.

In addition to fiber-optic networks (Fiber-Wireless, FiWi) combining optical and radio access, modern service also depends on IP (Internet Protocol) transport, computing resources, and the availability of the service function. Therefore, the capacity of an individual line is not equal to the availability of the entire service. In this work, a hybrid network is understood as an integrated network that combines optical, wireless, and IP transport segments, as well as computing and control segments, through coordinated control and resource allocation. This is a working definition of the object, not a literal quotation from the standard.

Reviews of network viability and recovery models provide a framework for studying the consequences of damage [4, 5]. Research on coordinated configuration updates [7, 8], virtual function migration [9, 10], and prediction and migration management [11, 12] ensures the correctness of certain processes. Patent documents show that the ideas of restoration, standby power nodes, telemetry-based prediction, and function transfer are already well-known [13-16]. The unresolved problem for a specific engineering installation is to reconcile the assumptions of these approaches: which resources are common, what determines the completion of restoration, and what actions are permissible in transition mode.

The aim of the study is to construct a system of such dependencies and determine the limitations of the applicability of certain directions in a verifiable form. The following tasks were set: (I) comparison of the object of evaluation, the resources taken into account, and the verifiable result of existing approaches based on subject analysis; (II) derive an analytical expression that distinguishes a break due to a common cause from an independent break; (III) Quantitative estimation of their contribution to service probability by sequentially introducing constraints on the overall cause, physical capacity, and transition process in a five-segment model experiment.

The following hypotheses were tested. H1: the independence hypothesis regularly increases the probability of service at the same marginal disconnection probabilities. H2: checking for a single connection when logical backups share the same physical capacity further increases the likelihood of service. H3: The presence of a final configuration does not guarantee the admissibility of the transition process to it.

Materials and methods

1. Method of literature analysis

Subject commentary was applied with predetermined selection criteria. Included sources directly describing network architecture, service dependency on losses, coordinated configuration upgrades, function migration, or predictive calibration. Bibliographic data were compared with DOI, publishing pages, and document texts. The work does not claim bibliometric completeness and does not use the number of found publications as a measure of scientific significance.

A technical problem was taken as the unit of comparison. For each group, the control object, necessary information, resource limitation, and verifiable output were determined. The general cause directly affecting several objects and the cascade that arises after a change in regime were considered separately. The simultaneous arrival of accident reports does not prove any of these mechanisms.

2. Common cause two backup path model

In the analytical study, the local lesions of the two alternative pathways were independent, and the probabilities were assumed to be equal to p_1 and p_2. A common cause is likely to disrupt both paths. The probability that there is at least one healthy path is expressed as follows:

$$P = (1 - q)\,(1 - p_1 p_2), \qquad (1)$$

where P is the probability of at least one healthy path; q is the probability of a common cause; p_1, p_2 - probabilities of independent local lesions in the absence of a common cause. The presence of a road does not yet guarantee sufficient capacity and functionality readiness.

For an invalid independent model, the marginal damage probability of each path is maintained:

$$f_i = q + (1-q)\,p_i, \quad i = 1,2; \qquad P_{must} = 1 - f_1 f_2, \qquad (2)$$

where f_i is the probability of total damage to the i-th track; P_must is the service probability assuming the roads are independent. The equality of the boundary probabilities prevents the dependence from being replaced by a change in the reliability of the individual path.

Confirmation. If 0<q<1, overestimate:

$$\Delta = P_{must} - P = q(1-q)(1-p_1)(1-p_2) \qquad (3)$$

and is strictly positive for p_1, p_2<1.

Proof. According to $1 - P = q + (1-q)p_1p_2$. According to (2) $f_1f_2 = q^2 + q(1-q)(p_1+p_2) + (1-q)^2p_1p_2$. Thus, $\Delta = (1-P) - f_1f_2 = q(1-q) + (1-q)p_1p_2\,[\,1-(1-q)\,] - q(1-q)(p_1+p_2) = q(1-q)\,(1-p_1-p_2+p_1p_2)$, which is equal to (3). ▫

Bundan ikki xulosa kelib chiqadi. Birinchidan, Δ ning q bo‘yicha maksimumi $q = 1/2$ da erishiladi va $(1-p_1)(1-p_2)/4$ ga teng. Ikkinchidan, kichik q va kichik p_i da $\Delta \approx q$, ya’ni xato umumiy sabab ehtimoli bilan bir xil tartibda bo‘ladi. Demak, zaxiralangan yo‘llarni mustaqil deb hisoblash xatosi umumiy sabab ehtimolidan kichik bo‘lmaydi.

Two conclusions follow from this. First, the maximum of Δ with respect to q is reached at $q = 1/2$ and is equal to $(1-p_1)(1-p_2)/4$. Second, for small q and small p_i, Δ≈q, i.e., the error is in the same order as the general causal probability. Consequently, the error of counting backed-up paths as independent will not be less than the overall causal probability.

3. Five-segment service model

The proposed five-segment service model (Fig. 1) represents the connections between root causes, segments, a unified physical resource registry, and the joint provision of a critical service. The arrows indicate dependencies, not the direction of the packets. The

register represents the principle of "one physical object - one capacity": if several logical connections pass through the same physical object, they do not create additional capacity.

For the quantitative verification of the circuit by quality, it was determined that the critical service requires the sequential execution of five segments: optical (O), wireless (W), IP-transport (T), computational (C), and control (K). Each segment consists of two reserved units (e.g., O1 and O2), and the segment runs when at least one unit is running. The unit is considered interrupted in the following cases: local independent damage (possibly p_u) or the occurrence of a common group of causes to which it belongs (possibly q_g). Connection service availability indicator:

$$\mathbb{1}_{con} = \prod_{s=1}^{5}(1 - x_{s1}x_{s2}), \qquad (4)$$

where x_sj∈{0,1} is an indicator indicating that the j-th unit of the s-segment is interrupted. The parameters are presented in Tables 1 and 2. All values are sample assumptions selected by the researcher and do not represent any operator network. Two additional conditions are included in the coupling condition. We check the capacity condition when the primary unit (index 1) is disconnected in the O, W, and T segments and switches to the backup unit (index 2):

$$c + b_s \leq C, \qquad (5)$$

where c~U (2;8) is the required critical service bandwidth; b_s~U (0;6) is the available critical load in the reserve unit; C=10 is the physical capacity of the reserve unit (in conventional units). This condition is absent only in the model that verifies the presence of a road.

We check the condition of the transition process in the G3 event (when the network power supply is interrupted at site A, when the equipment is running on a battery) to transfer the computational function to site B:

$$T_m = \frac{8S}{B_r} \leq \min(T_d,\ T_b), \qquad T_b = \frac{3600\,E_b}{P_A}, \qquad (6)$$

where T_m is the transfer time, s; S~U (20;200) is the volume of the state, GB; B_r~U (2;10) is the residual bandwidth, Gbit/s; T_d=120 s is the permissible service restoration period; T_b is the battery life, s; E_b~U (10;60) is the usable energy of the battery, W·h; P_A~U (300;600) - site power, W. If there is insufficient power or the timeout period is exceeded during the migration, the service will not be restored even if the final configuration is available.

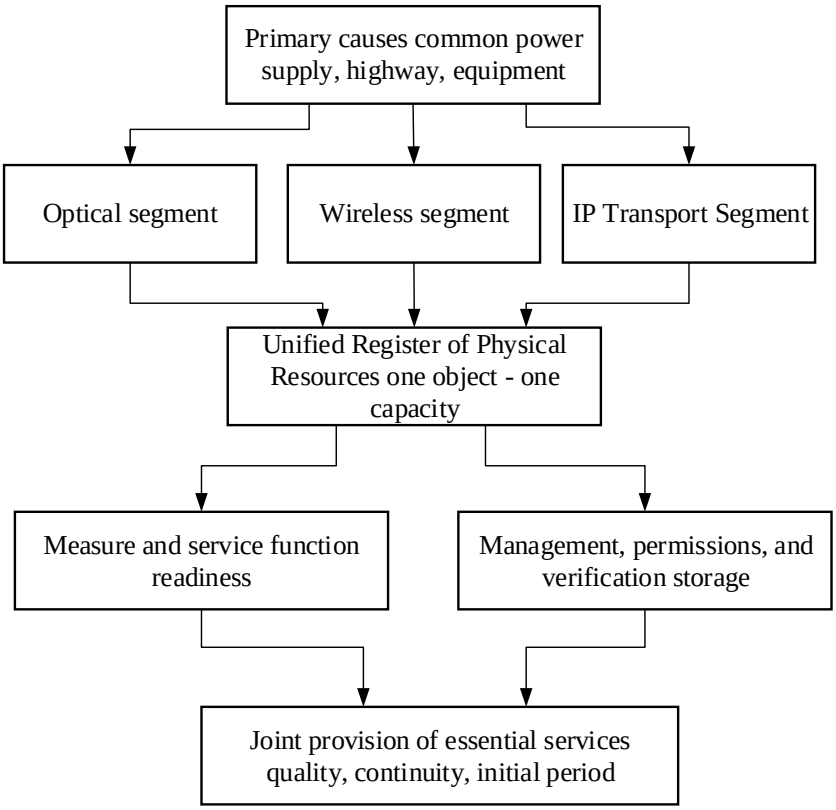


Fig. 1. The relationship between root causes, physical resources, and service delivery

Table 1. Units of the model and common causal groups

Segment	Units	Local probability p_u	Boundary disconnection probability f_u
Optical (O)	O1, O2	0,02	0,0376
Wireless (W)	W1, W2	0,03	0,0358
IP Transport (T)	T1, T2	0,02	0,0337
Calculation (C)	C1, C2	0,02	0,0298
Control (K)	K1, K2	0,01	0,0199

Common cause group	q_g	Exposed units
G1: Common Optical Path	0,008	O1, O2
G2: General power supply of radio sites	0,006	W1, W2
G3: Site A power outage	0,010	O1, T1, C1, K1
G4: Site B power outage	0,010	O2, T2, C2, K2
G5: Common IP Route	0,004	T1, T2

4. Model options and calculation protocol

Four variants were compared sequentially to separate the contributions of the components:

M0 - independent interruptions; the boundary probability of each unit is the same as M1 ($f_u = 1 - (1 - p_u)\prod_{g \ni u}(1 - q_g)$), except for the dependence (4);

M1 - common causal groups are taken into account, only association;

M2 - M1 and capacitance condition (5);

M3 - M2 and transition process condition (6) (full model).

For each variant, 30 independent repetitions were performed; 10^6 tests were conducted in each repetition. The results were presented with a 95% confidence interval based on the mean and Student's t-distribution. The initial value of the random number generator has been recorded. The Monte Carlo results for M0 and M1 were verified by the precise counting of 15 binary variables (2^{15} cases). In the sensitivity analysis, all q_g values were multiplied by the coefficient $\lambda \in \{0;0.25;0.5;1;2;4\}$ (10 repetitions, $5 \cdot 10^5$ trials each); for the transition process, the allowable displacement fraction was calculated using a grid of E_{max} and T_d values ($2 \cdot 10^6$ trials). Codes and result tables are provided as supplementary materials.

Analysis and Results

1. Subject comparison of approaches

The results of the comparison of directions are presented in Table 2, and the technical characteristics of the patent documents are presented in Table 3.

Table 2. Subject comparison of research directions

Direction	The main issue	Additional review required
FiWi and energy efficiency [2, 6]	Combined use of optics and radio	Common service chain readiness
Network viability models [5]	Service change after damage	Incomplete recovery storage
Agreed updates [7, 8]	The correctness of the transition between configurations	Resources and initial service life
Transfer of functions [9, 10]	Select transfer and positioning state	Energy and power of the entire transition
Forecasting and migration [11, 12]	Crash prevention and motion selection	Calibration and independent technical clearance

Table 3. Technical features of published patents

Document	Solution under consideration	Limit of comparison
US8964535B2 [13]	Restore traffic to a new path by managing the network	Joint access of critical services requires a separate submission
US9647494B2 [14]	Network reconstruction using backup power nodes	The presence of a battery does not necessarily mean that there is enough power for a full transfer.
US11153178B2 [15]	Tunnel damage prediction telemetry	Predictive control command not allowed
US12265843B2 [16]	Feature migration in case of server environment failure	The power supply and relocation time already belong to a certain technical level.

The classification distinguishes three types of reconciliation. The first links the logical architecture to a single physical quota. The latter attributes the damage to a user event, including quality and validation. The third relates the selected final configuration to the permissible process of achieving it. In the absence of any of these three links, an optimistic assessment arises even if the individual segment model is correct. This conclusion will be quantified in Sections 3.2–3.5.

2. Example with two backup paths

In the main case (q=0.01; p_1=0.02; p_2=0.03) according to (1) P_{must}=0.98941, according to (2) P_{must}=0.99882, therefore Δ=0.00941 corresponds to expression (3). Repeated Monte Carlo calculations confirmed the analytical values: P=0.98941±0.00004 and P_{must}=0.99881±0.00001. The probability of not being served is 0.01059 (with a common cause) and 0.00118 (independent model), with a ratio of 8.95.

Table 4. The influence of the general causal probability q (p_1=0.02; p_2=0.03; analytical calculation)

q	P	P_{must}	Δ	$(1-P)/(1-P_{must})$
0	0,99940	0,99940	0,00000	1,00
0,001	0,99840	0,99935	0,00095	2,46
0,005	0,99440	0,99913	0,00473	6,45
0,01	0,98941	0,99882	0,00941	8,95
0,02	0,97941	0,99804	0,01863	10,52
0,05	0,94943	0,99458	0,04515	9,34
0,1	0,89946	0,98501	0,08555	6,71

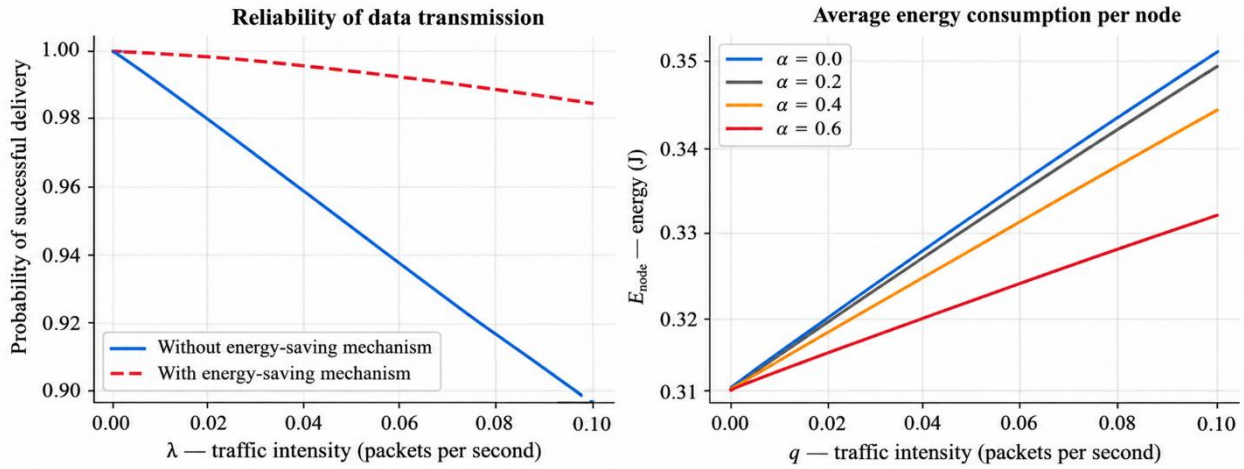


Fig. 2. In the two-step example, the overall causal effect is: a) the dependence of P and P_{must} on q; b) the dependence of Δ on q and p_i.

As shown in Table 4 and Figure 2, both models overlap at q=0, and Δ increases linearly as q increases. The ratio of the probability of failure is not monotonous: it reaches its

maximum value (by a factor of 10.5) around q ≈ 0.02, then as q increases, P_{must} also decreases, and the ratio decreases. As the probability of local damage increases, Δ decreases (Fig. 2b), as the side effect of the general cause is less pronounced against the background of local disruptions. Thus, hypothesis H1 was confirmed (analytically).

3. Five-segment model: component contributions

Monte Carlo results were consistent with the exact count: the exact presence for M0 was 0.994898, Monte Carlo 0.994873 ± 0.000025; For M1, 0.978547 and 0.978549 ± 0.000055, respectively. In both cases, the difference is within the confidence interval.

Table 5. Service availability by model variants (30 repetitions, 95% confidence interval)

Variant	Presence	Probability of not showing	Increase compared to the previous variant, p.p.
M0: independent	0,99487 ± 0,00002	0,51 %	-
M1: + common cause	0,97855 ± 0,00005	2,15 %	+1,63
M2: + capacity register	0,96090 ± 0,00007	3,91 %	+1,76
M3: + transition process	0,95723 ± 0,00008	4,28 %	+0,37

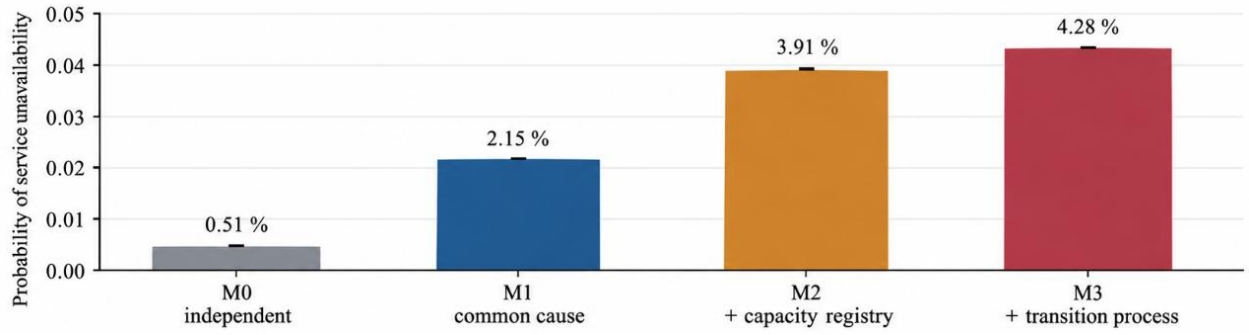


Fig. 3. Probability of non-service provision by model variants (error lines - 95% confidence interval).

The M0 model overestimates availability by 3.76 percentage points (0.99487 and 0.95723) compared to the full M3 model, indicating an 8.3-fold lower probability of non-disclosure (0.51% and 4.28%). The two largest contributions are due to the general cause

(+1.63 p.p.) and the physical capacity condition (+1.76 p.p.); the contribution of the transition process condition is smaller (+0.37 p.p.), but significantly higher than the confidence interval, which means it is statistically distinct. Hypotheses H1 and H2 were confirmed within the framework of the model. The magnitude of the capacity condition contribution depends on the selected load distribution ($c \sim U(2;8)$, $b_s \sim U(0;6)$, $C=10$): in this distribution, the condition (5) is not met in approximately 22% of the transition to the reserve.

4. Sensitivity to common cause probabilities

Table 6. Probability of non-service provision (%) by the overall cause probability scale λ

λ	M0	M1	M2	M3
0	0,222	0,219	1,719	1,719
0,25	0,276	0,706	2,281	2,375
0,5	0,351	1,184	2,816	3,003
1	0,510	2,130	3,906	4,276
2	0,935	4,069	6,084	6,799
4	2,210	7,875	10,342	11,683

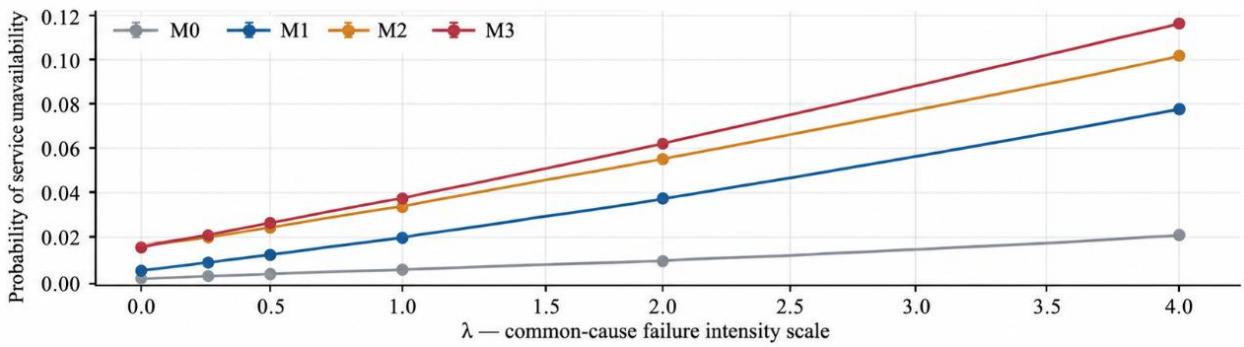


Figure 4. Sensitivity to the overall cause probability scale λ.

At λ=0, M0 and M1 practically overlap (0.222% and 0.219%; the difference is within the confidence interval), as there is no common cause. At this point, models M2 and M3 yield 1.72%: this indicates an independent effect of the existing capacity constraint and differs from the general cause. As λ increases, the discrepancy between M0 and M3 expands: 11.68% for M3 at λ=4, and 2.21% for M0. Thus, the optimistic error of the

independent model is not only maintained when the total causal proportion increases, but also increases in absolute value.

5. Admissibility of a transition process

In the event of G3, the allowable share of the computational function shift depends on E_{max} and T_d (Fig. 5). The criterion checking the final configuration always considers the displacement to be permissible in this case (share 1.00), while the full transition criterion gives 0.38 at E_{max}=60 W·h and T_d=120 s. When the time is extended to 600 s and E_{max} = 200 W·h, the fraction reaches 0.92. At T_d=60 s, the fraction is practically independent of E_{max} (0.14): in this case, the transfer time itself is the limiting factor. Increasing the battery energy from 20 to 200 W·h at T_d=120 s changes the fraction only from 0.34 to 0.39, i.e., the duration is more restrictive than the energy in these parameters.

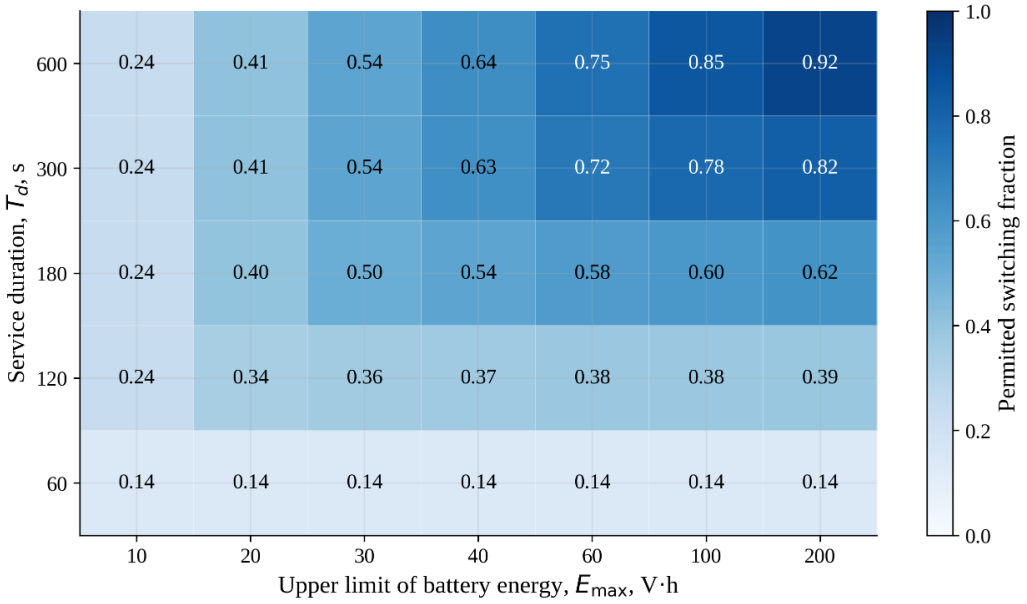


Fig. 5. Allowable displacement fraction: by battery energy E_{max} and service life T_d ($E_b \sim U(10; E_{max})$).

This result supports the H3 hypothesis: the presence of a backup unit at site B does not ensure the completion of the migration process.

Discussion

The results showed that all three links of the classification in section 3.1 are of quantitative significance. The probability of non-provision of services, excluding the general cause, was assessed as less than four times (0.51% vs. 2.15%); Expression (3) gives

a closed view of this error and clearly indicates its source: even if the marginal reliability is the same, the combination of interruptions reduces the backup effect. The largest contribution was made by the calculation of capacity from a single register, since the transition to a backup road requires not only the discovery of a road, but also a sufficient amount of its free capacity. The transition process condition made a relatively small contribution to these parameters, but it was associated only with the G3 event (q=0.01); although such an event was unlikely, the transition within it was in many cases inadmissible.

Division into five segments does not imply their statistical independence and does not correspond to the seven levels of the OSI model. A single hardware node can perform several functions simultaneously; conversely, a single service can pass through several independent sites. Therefore, the composition of the model should be determined not by the names of levels, but by supporting resources.

Energy efficiency and viability are related, but the criteria are different. Reducing average power may reduce backup, and migration will require additional resources until a new mode is reached. Similarly, high accuracy in classifying injuries does not guarantee that taking action in advance is beneficial. The full cost of preparation and the same conditions of comparison must be maintained during the evaluation.

Limitations. (I) All numerical results were obtained in model data; probabilities, loads, battery, and displacement parameters were selected by the researcher and were not measured on the actual operator network. Therefore, absolute values (for example, 0.51% and 4.28%) are not generalized; only the trend between model variants and the analytical conclusion of expression (3) are of more general significance. (II) The model is static: the time process of interruption and recovery, the repair duration, and the cascades are not modeled separately. (III) Each segment consists of two units, real topologies are more complex. (IV) Predictive calibration and recovery memory have not been quantified in this work, they are the task of the next stage. (V) The independent model is deliberately chosen as a simple theoretical basis; real operators often partially account for common causes;

therefore, a comparison with M0 shows the magnitude of the error of neglecting the relationship rather than evaluating their actual methods. (VI) The results have not been confirmed in industrial conditions.

Conclusion and Recommendations

A research object has been substantiated, uniting the five segments through common resources and service requirements. A classification of dependencies has been proposed, allowing for the reconciliation of architectural characteristics, the phenomenon of failure, and the restoration process. It has been proven that the independence hypothesis increases the probability of service by $\Delta=q\ (1-q)\ (1-p_1)\ (1-p_2)$ in a two-path backup model. In the five-segment model experiment, it was shown that the optimistic error of the independent model (4.28% vs. 0.51% of the probability of non-service) consists of the contributions of the common cause (+1.63 p.p.), the capacity register (+1.76 p.p.), and the transition process (+0.37 p.p.), these values are characteristic of the selected parameters. The main directions of further investigation are the assessment of the causes of general damage from real operational data, verified recovery, the permissibility of full transition, and the serviceability of the forecast. These directions form the engineering verifiable basis for viability models and algorithms.

References

[1] International Telecommunication Union, Measuring digital development: Facts and Figures 2025. Geneva: ITU, 2025. ISBN 978-92-61-41501-3. [Onlayn]: https://www.itu.int/dms_pub/itu-d/opb/ind/D-IND-ICT_MDD-2025-3-PDF-E.pdf

[2] N. Ghazisaidi, M. Maier, and C. Assi, “Fiber-wireless (FiWi) access networks: A survey,” IEEE Communications Magazine, vol. 47, no. 2, pp. 160–167, 2009. DOI: 10.1109/MCOM.2009.4785396.

[3] J. Halpern and C. Pignataro, Eds., “Service Function Chaining (SFC) Architecture,” RFC 7665, 2015. https://www.rfc-editor.org/rfc/rfc7665.html

[4] J. P. G. Sterbenz, D. Hutchison, E. K. Çetinkaya, A. Jabbar, J. P. Rohrer, M. Schöller, and P. Smith, “Resilience and survivability in communication networks: Strategies, principles, and survey of disciplines,” Computer Networks, vol. 54, no. 8, pp. 1245–1265, 2010. DOI: 10.1016/j.comnet.2010.03.005.

[5] P. E. Heegaard and K. S. Trivedi, “Network survivability modeling,” Computer Networks, vol. 53, no. 8, pp. 1215–1234, 2009. DOI: 10.1016/j.comnet.2009.02.014.

[6] J. Lorincz, Z. Klarin, and D. Begušić, “Advances in improving energy efficiency of fiber–wireless access networks: A comprehensive overview,” Sensors, vol. 23, no. 4, art. 2239, 2023. DOI: 10.3390/s23042239.

[7] M. Reitblatt, N. Foster, J. Rexford, C. Schlesinger, and D. Walker, “Abstractions for network update,” in Proc. ACM SIGCOMM, 2012, pp. 323–334. DOI: 10.1145/2342356.2342427.

[8] K.-T. Foerster, S. Schmid, and S. Vissicchio, “Survey of consistent software-defined network updates,” IEEE Communications Surveys & Tutorials, vol. 21, no. 2, pp. 1435–1461, 2019. DOI: 10.1109/COMST.2018.2876749.

[9] V. Eramo, M. Ammar, and F. G. Lavacca, “Migration energy aware reconfigurations of virtual network function instances in NFV architectures,” IEEE Access, vol. 5, pp. 4927–4938, 2017. DOI: 10.1109/ACCESS.2017.2685437.

[10] C. Clark, K. Fraser, S. Hand, J. G. Hansen, E. Jul, C. Limpach, I. Pratt, and A. Warfield, “Live migration of virtual machines,” in Proc. USENIX NSDI, 2005, pp. 273–286. https://www.usenix.org/conference/nsdi-05/live-migration-virtual-machines

[11] T. Sun, H. Hu, and S. Zhang, “Load-balanced dynamic SFC migration based on resource demand prediction,” Sensors, vol. 24, no. 24, art. 8046, 2024. DOI: 10.3390/s24248046.

[12] H. Hu, Z. Liu, and F. Wu, “RL-PMO: A reinforcement learning-based optimization algorithm for parallel SFC migration,” Sensors, vol. 26, no. 1, art. 242, 2026 (onlayn nashr: 30.12.2025). DOI: 10.3390/s26010242.

[13] US 8,964,535 B2, “Methods, apparatus and communication network for providing restoration survivability,” nashr sanasi: 24.02.2015. https://patents.google.com/patent/US8964535B2/en

[14] US 9,647,494 B2, “Fast network formation using a battery-backed network backbone,” nashr sanasi: 09.05.2017. https://patents.google.com/patent/US9647494B2/en

[15] US 11,153,178 B2, “Piggybacking control and data plane telemetry for machine learning-based tunnel failure prediction,” nashr sanasi: 19.10.2021. https://patents.google.com/patent/US11153178B2/en

[16] B. Lemoine, J.-F. Boussardon, A. Niculescu, and J. Penhoat, “Method and device for migrating a virtualized function in the event of a failure in the technical server environment,” US 12,265,843 B2, Orange, nashr sanasi: 01.04.2025. https://patents.google.com/patent/US12265843B2/en

UDC: 621.391:519.24

A MODEL FOR ASSESSING CONFIRMED RECOVERY OF CRITICAL TELECOMMUNICATIONS SERVICES USING TIME CONSTRAINTS AND EPISODE MEMORY

Matyokubov Utkir Karimovich
PhD, dotcent, Urgench State University named after Abu Rayhan Biruni,
otkir_matyokubov89@mail.ru

Annotatsiya. Aloqa tarmog‘i tiklanganda odatda liniya yoki marshrutning yoqilgan lahzasi qayd etiladi, biroq muhim xizmat bu paytda hali ishlamasligi mumkin. Maqolada texnik uzatish imkoniyatining tiklanishi bilan xizmatning tasdiqlangan tiklanishi o‘rtasidagi farq o‘rganilgan. Xizmat hodisasining boshlanish lahzasini va uzluksiz sifat tasdig‘ining xotirasini saqlaydigan model taklif etilgan: takroriy buzilish tasdiqlash oynasini nolga qaytaradi, lekin ruxsat etilgan muddatni uzaytirmaydi. Birgalikdagi xizmat, mavjud vaqt ulushi, eng uzoq uzilish va shartli tiklanish ehtimoli bir tizimda ko‘rib chiqilgan; to‘liq bo‘lmagan kuzatuvlar uchun quyi va yuqori indikatorlar kiritilgan. Natijalar deterministik izlarda va 10 000 ta realizatsiyali modelli Monte-Karlo seriyasida olingan (real operator o‘lchovlari ishlatilmagan). Mavjud vaqt ulushi 0,9333 ga teng bo‘lgan uch trayektoriyada eng uzoq uzilish 40, 10 va 2 s bo‘lgani ko‘rsatildi. Deterministik izda tasdiqlash oynasi 5 s bo‘lganda tasdiq 19-soniyada ro‘y berib, 18 s lik muddatni buzdi. Modelli seriyada (D = 40 s) muddatda tasdiqlangan tiklanish ulushi θ = 0 da 95,2 % dan θ = 20 s da 50,4 % gacha pasaydi; muddatni takroriy buzilishdan qayta hisoblash qoidasi bu ulushni 79,6 % gacha oshirib yuboradi. Kuzatuvlarning 20 % i yo‘qolganda natijalarning 17,6 % i noaniq bo‘lib qoladi. Natija tiklash usullarini solishtirishda ishlatiladigan ko‘rsatkichlarning mosligini ta’minlaydi.

Kalit so‘zlar: *muhim xizmat; sifat tasdig‘i; tiklanish muddati; uzluksizlik; to‘liq bo‘lmagan kuzatuvlar; Monte-Karlo modellashtirish.*

Аннотация. При восстановлении сети связи обычно фиксируется момент включения линии или маршрута, однако важная служба в это время может быть еще недоступна. В статье исследуется разница между восстановлением технической передачи и подтвержденным восстановлением

обслуживания. Предложена модель, которая сохраняет момент начала служебного события и память непрерывного подтверждения качества: повторный сбой сбрасывает окно подтверждения, но не продлевает допустимый срок. Совместная служба, доля доступного времени, вероятность наибольшего отключения и условного восстановления рассматриваются в одной системе; для неполных наблюдений включены нижний и верхний индикаторы. Результаты получены в детерминированных следах и в модельной серии Монте-Карло с 10 000 реализациями (измерения реальных операторов не используются). Показано, что на трех траекториях с долей времени, равной 0,9333, самый длинный разрыв составил 40, 10 и 2 с. В детерминированной траектории, когда окно подтверждения было 5 с, подтверждение произошло на 19-й секунде, нарушив 18-секундный срок. В модельной серии (D = 40 с) доля восстановления, подтвержденная в срок, снизилась с 95,2% при θ = 0 до 50,4% при θ = 20 с; правило пересчета срока от повторного нарушения увеличивает эту долю до 79,6%. При потере 20% наблюдений 17,6% результатов оказываются неточными. Результат обеспечивает соответствие показателей, используемых при сравнении методов восстановления.

Ключевые слова: *важная услуга; подтверждение качества; срок восстановления; непрерывность; неполные наблюдения; Моделирование Монте-Карло.*

Abstract. Network recovery usually records the moment the line or route is turned on, but a critical service may not be available at that time. The article examines the difference between the restoration of technical transmission capability and the confirmed restoration of service. A model is proposed that stores the start moment of the service event and the memory of continuous quality assurance: a repeated failure resets the assurance window to zero but does not extend the allowable timeframe. Joint service, share of available time, probability of the longest interruption and conditional recovery are considered in one system; lower and upper indicators are included for incomplete observations. The results

are obtained in deterministic traces and in the Monte Carlo series with a model of 10,000 implementations (measurements of the real operator are not used). It was shown that in three trajectories with a time fraction of 0.9333, the longest interruptions were 40, 10, and 2 s. In the deterministic trace, when the confirmation window was 5 s, the confirmation occurred at 19 s, breaking the 18 s deadline. In the model series (D = 40 s), the proportion of confirmed recovery decreased from 95.2% at θ = 0 to 50.4% at θ = 20 s; the rule for recalculating the duration from repeated failure increases this proportion to 79.6%. When 20% of observations are lost, 17.6% of the results become inaccurate. The result ensures the consistency of the indicators used in the comparison of recovery methods.

Keywords: *essential service; quality assurance; recovery period; continuity; incomplete observations; Monte Carlo simulation.*

Introduction

When the network is restored, the moment the line or route is turned on is often recorded. However, the service may not be available yet due to a queue, an unresolved feature, or a session status that has not been fully restored. Therefore, it is necessary to distinguish between hardware indicators and user service indicators [1, 2]. In reliability theory, this distinction is not new: in [1], service failure is separated from the concepts of internal failure and error, while in [7], systems that can operate with degradation are evaluated by the levels of efficiency achieved from the user's perspective.

Work on network survival and resilience provides a wide range of methods for modeling recovery: Heegaard and Trivedi have reviewed approaches to survival modeling, [2] Sterbenz et al. have systematized strategies and principles of resilience, [3] Chołda et al. have reviewed approaches to differentiating resilience by service classes. Practical observations show that network interruptions are a common phenomenon: an analysis of failures in the IP trunk network revealed that approximately one-fifth of them occur during a weekly maintenance window, and failures are concentrated on a small number of lines [8], while in data center networks, despite high availability, downtime is unevenly distributed by device type [9]. In the service function chain (SFC) architecture[4], the service is implemented through ordered functions, so

the readiness of functions in the chain is a separate condition from the recovery of the route. Three practical issues remain unresolved in the existing approaches. First, the time-average availability [3] indicator does not determine the number and duration of interruptions, so trajectories with the same fraction but different continuity do not differ from each other. Second, a short-term improvement does not prove that the service has been restored, but voluntary waiting after each reconnection distorts the assessment; the confirmation window and its reset rule must be set in advance. Thirdly, the resumption of the permitted period in the event of a repeated violation artificially increases the recovery rate. An additional difficulty arises from the incompleteness of the observations: the missing measurements make the result indeterminable. The aim of the work is to construct an iterative rule for processing trajectories that does not change the initial requirements after a distortion occurs, and to evaluate its properties experimentally. The study seeks to answer the following questions: RQ1. Does the same share of available time mean the same continuity of service?

RQ2. How do the duration of the confirmation window and repeated deterioration affect the probability of recovery within the allowed timeframe, and what deviation does the timeframe restart rule provide? RQ3. How should the result be expressed in incomplete observations, and when is the probability of conditional recovery not determined? The contribution of the work is as follows: (I) an episode model that stores the start moment of an event and a continuous affirmative memory, with a boundary coincidence rule; (II) a system of indicators linking joint service, available time share, and the longest interruption; (III) lower and upper indicators for incomplete observations, as well as a three-result classification; (IV) repeated experiments: deterministic traces and a model series with 10,000 implementations. The novelty of this work is not confirmed by a complete systematic review of the literature; the author does not make a claim that it is “first” or “only”; the contribution is limited to the aforementioned specific mechanisms and their experimentally verified properties.

Materials and methods

1. Service requirements and indicator

For each service s, the minimum speed, latency, latency variation, and loss share threshold values, function chain readiness, allowable recovery time D (s), and confirmation window θ (s) are predetermined. These values are research conditions and are not declared as a general norm for all operators. Table 1 presents the standard requirements adopted in the study. The indicator I (s,t) is equal to one only when all requirements are met simultaneously.

Table 1. Example of predefined service requirements (research terms)

Service	Minimum, Mbps	Delay, ms	Loss fraction	Expiration / approval, s
Speech	0,06	150	0,01	15 / 2
Emergency messages	0,099	500	0,001	30 / 2
Situational video	0,99	300	0,01	60 / 2

2. Episode model

The start of the failure is recorded at the moment t_0 and is maintained in the model state until verification is complete. If a new deterioration occurs, the accumulated time of continuous good quality is reduced to zero, but t_0 does not change. Failure following a successfully completed approval will unlock a new episode. If the breakdown and confirmation moments coincide, the breakdown is processed first; this rule must be explicitly specified in the event handler. The disturbance interval [a, b] is taken as half-open, and the confirmation window [t−θ, t] is checked as a closed segment.

The confirmed recovery moment is given by equation (1), and the condition for adhering to the time limit is given by inequality (2):

$$T(s) = \inf\{t \geq t_0 + \theta(s) : I(s,u) = 1 \quad \forall u \in [t - \theta(s), t]\} \tag{1}$$

Where T (s) is the confirmed recovery moment; θ (s) is the required duration of continuous good quality; u is the time in the window. If there is no corresponding interval, then T (s) = ∞.

$$T(s) - t_0 \leq D(s) \tag{2}$$

Here, D (s) is the permissible recovery duration given before the experiment. The technical recovery of the resource and the waiting for confirmation are noted separately. The logic of the event handler is given by the following algorithm.

Algorithm 1. Sequential event processing (per service).

1) Input: consecutive observations (time, I), θ, D. Status: episode open/closed, t_0, g (the moment when continuous good quality begins).

2) If I = 0: the episode is opened and the current moment t_0 = is recorded; if open, t0 is not changed; g is cleared (reset to zero).

3) If I = 1 and g is empty: g = current moment.

4) If the episode is open, g is specified, and the current moment is − g ≥ θ: T = current moment, the episode is closed, and the result is written as “in time” (T − t0 ≤ D) or “after time”.

5) In instantaneous events, the distortion is processed before confirmation.

3. Metrics

To characterize the level of service not only by the average share but also by the structure of interruptions, expression (3) and its additional indicators are used:

$$A(s) = 1 - \frac{1}{T_{obs}} \int_0^{T_{obs}} [1 - I(s,t)]dt \tag{3}$$

Here, A (s) is the fraction of the optimal service life in the [0, T_{obs}] period; T_{obs} - duration of observation. This metric does not determine the number of interruptions or the longest interruption. Therefore, the discontinuities are denoted as [a_k, b_k], k = 1, ..., N_{int}, and the additions $L_{max} = \max_k (b_k - a_k)$ and N_{int} are noted. When multiple services need to be restored together, a conservative joint indicator, window, and timeframe are removed:

$$I_\Sigma(t) = \prod_{s \in S} I(s,t), \quad \theta_\Sigma = \max_{s \in S} \theta(s), \quad D_\Sigma = \min_{s \in S} D(s) \tag{4}$$

Here, s ∈ S is the set of services considered together. Taking the maximum window and the minimum time at the same time makes the result protective: joint success is no higher than success for each service individually.

4. Incomplete observations

If the measurement is lost at certain moments, the true I is unknown, but is limited to the following values: lost observations are considered broken at the lower indicator (0), and good at the higher indicator (1). Then relation (5) holds:

$$I^-(s,t) \le I(s,t) \le I^+(s,t) \quad \Rightarrow \quad T^+(s) \le T(s) \le T^-(s) \tag{5}$$

In this case, T^- is calculated from the lower indicator, and T^+ is calculated from the upper indicator using equation (1). The result is divided into three classes: "confirmed" if $T^- - t_0 \le D$; $T^+ - t_0 > D$ – "not restored (proven)"; in other cases – "uncertain". Recovery according to the higher indicator is possible but not proven.

The conditional recovery probability is determined only when the initial failure probability V is positive:

$$P_{\text{rec}}(D) = P(T - t_0 \le D \mid V), \quad \hat{P}_{\text{rec}} = \frac{N_{\text{ok}}}{N_V} \tag{6}$$

Here, N_V is the number of broken episodes in the sample, and N_{ok} is the number of confirmed episodes within the timeframe. If $N_V = 0$, the estimate is undefined and cannot be taken as equal to one.

5. Model properties

Property 1 (monotonicity to the mirror). If $\theta_1 \le \theta_2$, then $T(\theta_1) \le T(\theta_2)$. Proof: every moment t that is permissible for θ_2 is also permissible for θ_1, since $[t-\theta_1, t] \subset [t-\theta_2, t]$ and $t \ge t_0+\theta_2 \ge t_0+\theta_1$. Consequently, the set of allowable moments for θ_2 is a part of the allowable set for θ_1, and its exact lower bound is not small.

Property 2 (unilateral shift of the reset period). If the countdown begins from the moment $t_0' \ge t_0$ instead of t_0 (e.g., when the last repeated failure ends), then $T - t_0' \le T - t_0$; therefore, each implementation of the "on-time" event is preserved under this rule, and the success rate cannot decrease. At the same time, $T \ge R$ (R is the moment when the indicator first becomes equal to one), so the share of technical recovery is not less than the share of confirmation.

Property 3 (boundaries of uncertainty). Relationship (5) is proved in the same way as property 1: if $I^- \le I \le I^+$, the sets of allowable moments are nested. These properties were verified experimentally for each implementation (Section 3).

6. Experimental design

The experiments were performed in Python 3 (NumPy, SciPy); the code uses precise counting in continuous time for E_1–E_3 and discrete observations with a 1 s step for E_4. In all experiments, the seed of the generator was recorded, and the comparable rules were evaluated in the same implementations (common random numbers).

E_1 is a deterministic trace. Failure is in the range [0, 10], repeated failure is in the range [12, 14]; D = 18 s; θ ∈ {0, 1, 2, 3, 5, 8} s. Verify the accuracy of the target time processing. E_2 - identical fraction, different structure. Total 40 s of interruption: one 40 s interruption, four 10 s interruptions, and twenty 2 s interruptions (at equal intervals). E_3 is a model of the Monte Carlo series. The total damage occurs at $t_0 = 0$. Technical readiness R is the maximum of three resource recovery times: the route (lognormal, median 6 s, σ = 0.6), the chain of functions (lognormal, median 12 s, σ = 0.7), and the session state (exponential, average 8 s). Recurrent deterioration after preparation occurs with a Poisson process (λ = 0.02 s−1), the duration of which is exponential (on average 3 s). These parameters are assumptions adopted for experimental purposes and are not derived from real operator data. N = 10,000 realizations for each pair (D, θ); D ∈ {20, 40, 60, 90, 120} s, θ ∈ {0, 2, 5, 10, 20} s. Three rules were compared: (P) the proposed rule; (Q) in the event of a repeated violation, a rule according to which the calculation of the term begins from the moment the last repeated violation ends; (C) only technical recovery (without confirmation). A 95% Wilson confidence interval was calculated for the shares [10]; the presentation of model experiment results was conducted according to the recommendations of Morris et al. (seed, number of implementations, confidence interval) [11]. Additional sensitivity: λ ∈ {0.005; 0.01; 0.02; 0.05} s−1, D = 40 s. E_4 - incomplete observations. E_3 trajectories were discretized with a step of 1 s (D = 40 s, θ = 5 s). Each observation q ∈ {0; 0.05; 0.1; 0.2; 0.4} probability were independently eliminated, lower and higher indicators were constructed, and the results were divided into three classes. E_5 is the denominator of the conditional probability equal to zero. The probability of failure in each of the observation intervals n = 200 is p ∈ {0.005; 0.01; 0.02; At 0.05}, the probability of no disturbance in the sample was estimated by (1−p) n and 20,000 model samples.

Analysis and Results

1. Same proportion, different continuity (E_2)

Table 2 shows three trajectories. In all of them, the available time share is A = 0.933333 (560/600), but the longest interruptions are 40, 10, and 2 s, and the number of

interruptions is 1, 4, and 20. Thus, A does not define continuity; for example, if it is required that the longest service interruption does not exceed 15 s (this requirement is absent from Table 1, taken for illustrative purposes only), only the third trajectory meets the requirement. Figure 1 shows the experimental results.

Table 2. Difference in the structure of interruptions over the same available time period (T_{obs} = 600 s)

Path	Available time share A	Longest interruption, s	Number of interruptions
One break, 40s	0,933333	40	1
Four interruptions, 10s each	0,933333	10	4
Twenty interruptions, 2 s each	0,933333	2	20

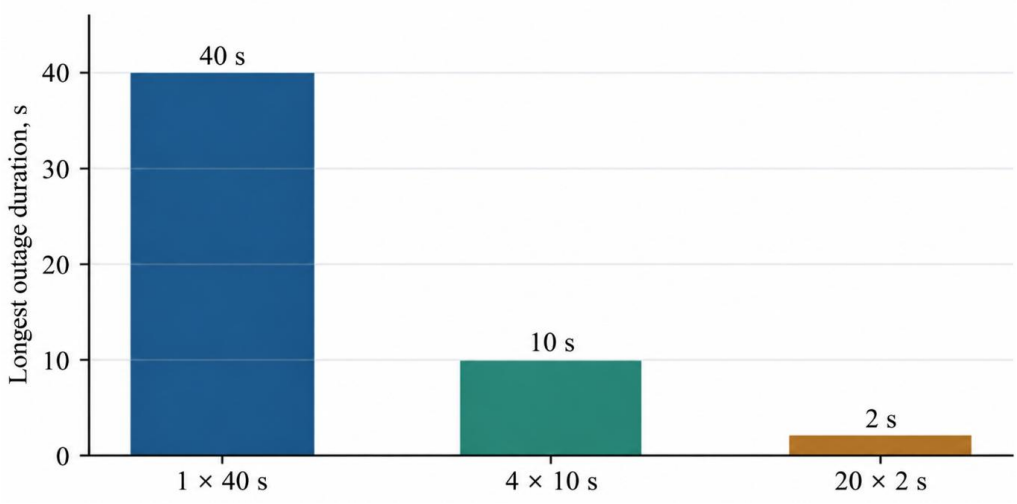


Fig. 1. Longest discontinuity on trajectories with available time fraction equal to 0.9333

2. Effect of continuous approval on the first episode (E_1)

Table 3 and Fig. 2 provide the results of the deterministic trace.

When the failure lasts up to 10 s and repeats within 12-14 s, if the window is 1 s, the first confirmation occurs at 11 s. If the window is 2 s, the coincidence with the distortion at 12 seconds is not counted as a confirmation, and the confirmation is at 16 seconds.

When the window is 5 s, the affirmation shifts to 19 s and breaks the original 18 s timeout. Moving the time count to 14 seconds (Rule Q) would yield a successful result for all windows; this is an erroneously positive result for 5 and 8 s windows.

Table 3. Effect of continuous validation on the first episode (duration D = 18 s)

Window θ, s	First statement T, s	Compliance with deadlines (Rule P)	Calculating the time from 14 s (Q)
0	10	Yes	Yes
1	11	Yes	Yes
2	16	Yes	Yes
3	17	Yes	Yes
5	19	No	Yes
8	22	No	Yes

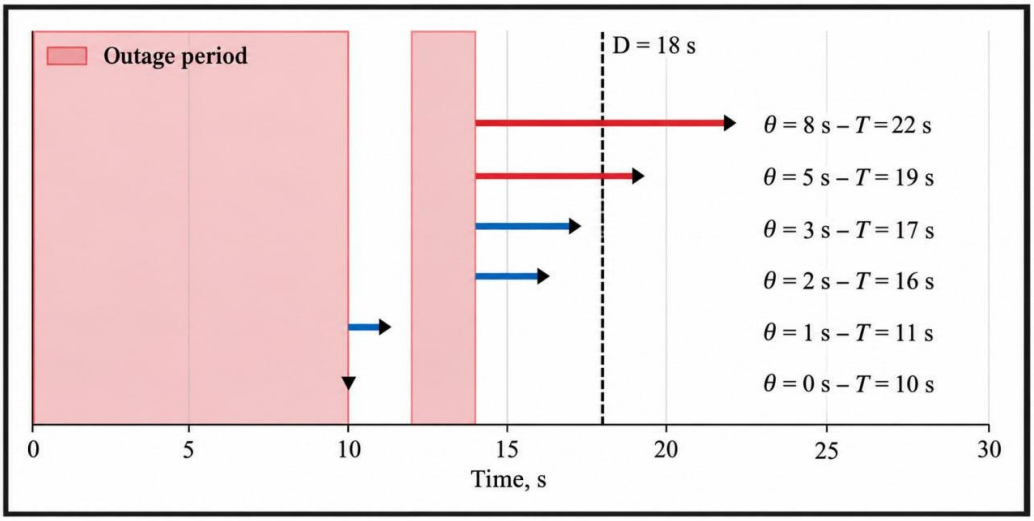


Figure 2. The moment of confirmation for various confirmation windows on the deterministic trace (thick line - confirmation window, ▼ - T). Pink areas - disorders

3. Model series: combined effect of time and window (E_3)

For technical readiness time R, the mean in the model series was 18.0 s, the median was 15.0 s, and the 90th and 99th percentiles were 31.9 s and 61.4 s. At θ = 0, the proposed rule corresponds only to technical readiness, and the proportion must be equal to the distribution function of R; analytical calculation using the product of three independent distribution functions (0.6885; 0.9501; 0.9886; 0.9980; 0.9995, D = 20, 40, 60, 90, 120 s) corresponded to the model results (the first column of Table 4) with a difference of no more than 1.9 standard errors. This was part of the code validation. Furthermore, properties 1 and 2 were not violated in all 10,000 implementations.

Table 4. Proportion of recovery approved within the timeframe (proposed rule, N = 10,000)

Duration D, s	θ = 0 s	θ = 2 s	θ = 5 s	θ = 10 s	θ = 20 s
20	0,6973	0,6209	0,4722	0,1874	0,0000
40	0,9517	0,9423	0,9190	0,8441	0,5041
60	0,9890	0,9872	0,9841	0,9723	0,8566
90	0,9978	0,9974	0,9971	0,9956	0,9797
120	0,9998	0,9998	0,9998	0,9994	0,9970

Note: At θ = 20 s and D = 20 s, the proportion is zero because T ≥ t0 + θ = 20 s, and equality is only possible at R = 0 (zero probability).

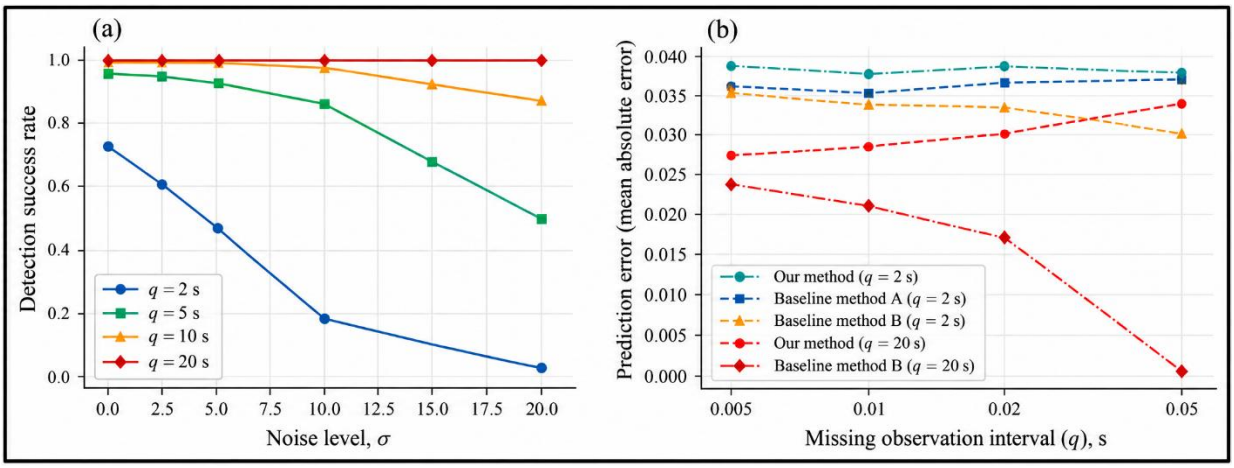


Fig. 3. (a) Dependence of successful recovery rate on confirmation window (shaded areas - 95% Wilson range); (b) sensitivity to the intensity of recurrent deterioration, D = 40 s (interlinear - proposed rule, dashed - period restart rule)

As shown in Table 4 and Figure 3 (a), the fraction decreases as the window lengthens, and the decrease is stronger when the period is shorter: at D = 20 s, the fraction decreases from 0.6973 at θ = 0 to 0.1874 at θ = 10 s, and at D = 40 s from 0.9517 to 0.8441; At D = 120 s, the change does not exceed 0.0004 until θ = 10 s. The proportion of episodes requiring confirmation after repeated failure at θ = 2, 5, 10, and 20 s was 4.1%, 9.8%, 18.1%, and 33.8%, respectively, while the mean confirmation moment was 18.0, 20.2, 23.6, 29.8, and 44.3 s.

Table 5 compares the three rules. The time restart rule (Q) yields at least a fraction of the proposed rule (P), which is consistent with property 2. The difference increases as the window lengthens and recurrent deterioration becomes more frequent: at D = 40 s and θ = 20 s, P is 50.4%, Q is 79.6%, and C is 95.2%. In the sensitivity

analysis (Figure 3 (b)) at $\lambda = 0.05$ s−1 and $\theta = 10$ s, P = 75.5%, Q = 92.5% (difference 17.0 percentage points), and at $\lambda = 0.005$ s−1, the difference is only 1.5 percentage points. For the proposed rule, the fraction generally decreases as λ increases (at $\theta = 2$ s, it is not monotonous, the differences are small); For Q, at $\theta = 10$ s, it increases, as with a large number of repeated failures, the counting start time is delayed, and the measured duration is reduced.

Table 5. Comparison of the three rules: P - proposed, Q - resumption of the term, C - only technical recovery (N = 10,000).

D, s	θ, s	P	Q	C
20	2	0,6209	0,6440	0,6973
20	5	0,4722	0,5502	0,6973
20	10	0,1874	0,3655	0,6973
20	20	0,0000	0,2910	0,6973
40	2	0,9423	0,9455	0,9517
40	5	0,9190	0,9323	0,9517
40	10	0,8441	0,9021	0,9517
40	20	0,5041	0,7963	0,9517

4. Incomplete observations (E_4)

At all levels of realization and loss, correlation (5) was maintained: violations of $T^+ \le T \le T^-$ were recorded 0 times (at 10,000 per q). The confirmed share in full observation was 91.8% (D = 40 s, $\theta = 5$ s, 1 s step). Table 6 and Figure 4 show that as the share of losses increases, the share of the “uncertain” class increases from 1.8% (q = 0.05) to 63.7% (q = 0.4), while the share of the “confirmed” class decreases accordingly; The “unrestored (proved)” class remained virtually unchanged (from 8.2% to 6.9%).

Table 6. Percentage of outcome classes when observations are lost (D = 40 s, $\theta = 5$ s)

Lost share q	Approved	Unclear	Not restored (proven)
0,0 %	0,9181	0,0000	0,0819
5,0 %	0,9008	0,0177	0,0815
10,0 %	0,8696	0,0501	0,0803
20,0 %	0,7452	0,1762	0,0786
40,0 %	0,2935	0,6373	0,0692

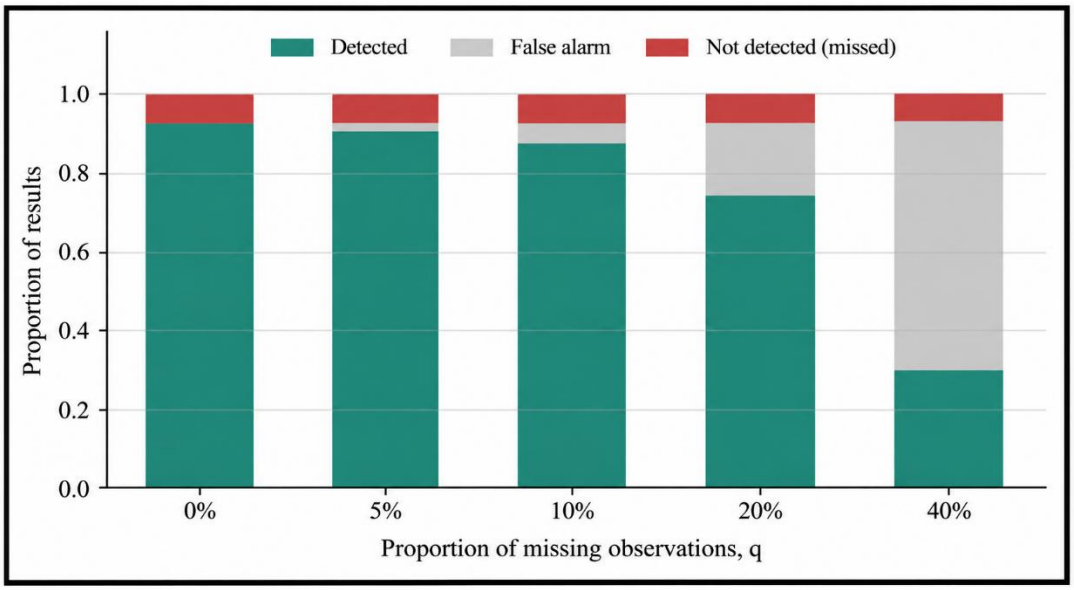


Fig. 4. Distribution of outcome classes by percentage of missing observations

5. The cross-section of services and the zero value of the conditional probability denominator (E_3, E_5).

When the time and window values (θ = 2 s) in Table 1 were applied separately for each service, the confirmed recovery rate in the E3 trajectories was 38.8% for "Speech" (D = 15 s) (95% range: 37.8-39.7%), 85.4% for "Emergency Messages" (D = 30 s), and 98.7% for "Situational Video" (D = 60 s). Taking into account only technical recovery, the shares would be 50.1%, 88.3%, and 98.9%; especially in short-term service, the unconfirmed price is significantly inflated. This result only applies to accepted model parameters.

The results of E5 are presented in Table 7: with a probability of distortion of 0.005 in an observation interval of 200 observations, approximately 37% of the sample do not experience any distortion, and the (6) -score is not determined; at a probability of 0.01, this proportion is approximately 13%. The model and analytical values coincided.

Table 7. Proportion of sample without distortion (the denominator is zero), n = 200

Failure probability p	Model estimate (20,000 samples)	Analytical $(1-p)^n$
0,005	0,3724	0,3670
0,01	0,1336	0,1340
0,02	0,0178	0,0176
0,05	0,0001	0,0000

Discussion

The extension of the confirmation window does not accelerate the recovery when the trajectory is unchanged; it only delays the moment of confirmation of the recovery (property 1). Therefore, the decrease in Table 4 is a consequence of the affirmation requirement, not the deterioration. However, a very small window increases the risk of mistaking a short-term improvement for a sustained service: at $\theta = 0$, no repeated failure is taken into account (the same result as rule C in section 3.3). The choice of window should take into account the frequency of observation and the physical content of the service; it is not correct to choose it based on the best result for the method being compared.

The error of the time restart rule (Q) is unilateral (property 2), and its magnitude depends on the intensity of repeated deterioration and the length of the window. In the short window ($\theta = 2$ s), the difference is less than 1 percentage point at D = 40 s and 2.3 percentage points at D = 20 s (Table 5); in the long window, it increases sharply: 29.2 percentage points at D = 40 s and $\theta = 20$ s, $\lambda = 0.05$ s^{-1} and 17.0 percentage points at $\theta = 10$ s (Figure 3 (b)). Consequently, the magnitude of the error is strongly dependent on the parameters and cannot be considered small in advance; the rule for the countdown moment must be clearly recorded. For Q, an increase in the fraction by λ indicates a logical flaw in the rule: the more repeated failures, the “faster” the recovery is.

The suggested episode memory cannot be reduced to three states, such as “good”, “broken”, and “restoring”. The moment of the initial disturbance, the accumulated affirmation, and the state of unfinished actions must be preserved. For non-exponential durations, the age or phase of the operation is also required; such a memoryless calculation would not properly account for repeated disruptions. The order of boundary events must be maintained during the discretization of observations: the 1 s step in E_4 therefore yielded almost the same fraction as the continuous calculation above (0.9181 and continuous 0.9190).

The E_4 results show how the incompleteness of the observations makes the result unreliable: at a loss share of 20%, 17.6% of cases are neither confirmed nor denied. Hiding this uncertainty and reducing it to an average or "good" value reduces the

reliability of the result. Similarly, equating the probability of conditional recovery to 1 in a sample with a small number of disturbances would be unjustified in all cases specified in E_5 (up to 37% at 0.005 probability).

1. Limitations

First, all E_3–E_5 results were obtained in model data; the recovery and recurrent deterioration distributions were assumed to be approximate and were not confirmed by real operator measurements. Secondly, the indicator is binary and generated in a ready state; The speed, latency, loss, and function chain requirements in Table 1 are not modeled at the packet level. Third, a protective rule (4) was used for the joint service, which did not take into account separate repeated disruptions of services and connections between resources. Fourthly, the boundaries and window values in Table 1 are the conditions of the study, and to conclude on their compliance with the requirements of a specific organization, agreed technical requirements and operational data are required. Fifth, the literature review is not systematic and is selective.

Conclusion

The approved recovery specification matches quality, process memory, and initial duration. In model experiments, it was shown that the same share of available time does not mean the same continuity (the longest interruption is 40, 10 and 2 s). Recurrent deterioration should not extend the allowable duration until confirmation is complete: the reset rule never decreases the recovery rate, but often increases it; the difference increases with window length and the intensity of recurrent deterioration (up to 29 percentage points in the model series, at $D = 40$ s and $\theta = 20$ s). In incomplete observations, the result should be divided into “confirmed”, “unconfirmed”, and “uncertain” classes without averaging; in a sample without distortion, the conditional probability should be considered undetermined. This allows for the comparison of recovery actions for a single service event.

Subsequent work: evaluation of recovery and recurrent failure distributions from real operational logs; simulation of a quality indicator at the package level; introduction of dependencies between resources and an episode phase into the model for non-exponential durations.

References:

[1]. Avižienis A., Laprie J.-C., Randell B., Landwehr C. Basic concepts and taxonomy of dependable and secure computing // IEEE Transactions on Dependable and Secure Computing. 2004. Vol. 1, no. 1. P. 11–33. DOI: 10.1109/TDSC.2004.2.

[2]. Heegaard P. E., Trivedi K. S. Network survivability modeling // Computer Networks. 2009. Vol. 53, no. 8. P. 1215–1234. DOI: 10.1016/j.comnet.2009.02.014.

[3]. Trivedi K. S., Bobbio A. Reliability and Availability Engineering: Modeling, Analysis, and Applications. Cambridge University Press, 2017. DOI: 10.1017/9781316163047.

[4]. Halpern J., Pignataro C. (eds.) Service Function Chaining (SFC) Architecture. RFC 7665, IETF, 2015. URL: https://www.rfc-editor.org/rfc/rfc7665.html.

[5]. Sterbenz J. P. G., Hutchison D., Çetinkaya E. K., Jabbar A., Rohrer J. P., Schöller M., Smith P. Resilience and survivability in communication networks: Strategies, principles, and survey of disciplines // Computer Networks. 2010. Vol. 54, no. 8. P. 1245–1265. URL: https://eprints.lancs.ac.uk/id/eprint/56825.

[6]. Chołda P., Mykkeltveit A., Helvik B. E., Wittner O. J., Jajszczyk A. A survey of resilience differentiation frameworks in communication networks // IEEE Communications Surveys & Tutorials. 2007. Vol. 9, no. 4. P. 32–55. DOI: 10.1109/COMST.2007.4444749.

[7]. Meyer J. F. On evaluating the performability of degradable computing systems // IEEE Transactions on Computers. 1980. Vol. C-29, no. 8. P. 720–731. DOI: 10.1109/TC.1980.1675654.

[8]. Markopoulou A., Iannaccone G., Bhattacharyya S., Chuah C.-N., Ganjali Y., Diot C. Characterization of failures in an operational IP backbone network // IEEE/ACM Transactions on Networking. 2008. Vol. 16, no. 4. P. 749–762. DOI: 10.1109/TNET.2007.902727.

[9]. Gill P., Jain N., Nagappan N. Understanding network failures in data centers: Measurement, analysis, and implications // Proc. ACM SIGCOMM 2011. Toronto, 2011. DOI: 10.1145/2018436.2018477.

[10]. Wilson E. B. Probable inference, the law of succession, and statistical inference // Journal of the American Statistical Association. 1927. Vol. 22, no. 158. P. 209–212. DOI: 10.1080/01621459.1927.10502953.

[11]. Morris T. P., White I. R., Crowther M. J. Using simulation studies to evaluate statistical methods // Statistics in Medicine. 2019. DOI: 10.1002/sim.8086.

UDC: 004.8:81'32

DESIGN AND EVALUATION PROTOCOL OF THE SEMANTIC SIMILARITY ANALYZER FOR AUTOMATIC DETECTION OF SEMANTIC SIMILARITY IN UZBEK TEXTS

Jurakulov Tolib Tokhirovich
Associate Professor, Navoi State University, Navoi, Uzbekistan
jamshidbektoxirov2021@gmail.com

Annotatsiya. Ushbu maqolada o‘zbek tilidagi matnlarni taqqoslash uchun mo‘ljallangan «Semantic Similarity Analyzer» (Semantik o‘xshashlikni tahlil qilish tizimi)ning takomillashtirilgan matematik modeli bayon etilgan. Muallifning ma’lumotlariga ko‘ra, dasturiy ta’minot ishlab chiqilgan va hozirda tajriba-sinov jarayonidan o‘tkazilmoqda. Biroq, ushbu tahrir uchun dasturiy ta’minotning birlamchi ishlash jurnallari (log fayllari) hamda mustaqil ekspertlar tomonidan belgilangan baholash natijalari taqdim etilmagan. Maqolada Navoiy viloyatidagi axborot-resurs markazlariga kelib tushadigan qidiruv so‘rovlari asosida shakllantirilgan shaffof, sun’iy keys-tadqiqot ma’lumotlar to‘plami taqdim etiladi, aniq belgilangan leksik bazaviy model hisob-kitob qilinadi hamda tizim faoliyatidagi diagnostik xatolik holatlari tahlil etiladi. Keltirilgan hisob-kitoblar amaliyotga joriy etilgan dasturiy ta’minot natijalari hisoblanmaydi va uning empirik aniqligini tasdiqlamaydi. Maqolada tizimni muassasa miqyosida ishonchli baholashni amalga oshirish uchun zarur bo‘lgan ma’lumotlar va hujjatlar ro‘yxati ham aniqlashtirilgan.

Kalit so‘zlar: *o‘zbek tili; semantik matn o‘xshashligi; morfologik tahlil; tillararo transfer; gap embeddinglari; baholash protokoli.*

Аннотация. В данной статье представлена усовершенствованная математическая модель системы «Semantic Similarity Analyzer», предназначенной для сравнения текстов на узбекском языке. Согласно информации, предоставленной автором, программное обеспечение разработано и в настоящее время проходит апробацию в реальных условиях. Однако первичные журналы работы приложения (лог-файлы), а также результаты

независимой экспертной разметки для данной редакции статьи представлены не были. В статье предлагается прозрачный набор синтетических данных для практического исследования, сформированный на основе поисковых запросов, поступающих в информационно-ресурсные центры Навоийской области. Выполнены расчёты с использованием чётко определённой базовой лексической модели, а также проанализированы диагностические случаи ошибок. Представленные иллюстративные расчёты не являются результатами работы внедрённого программного обеспечения и не подтверждают его эмпирическую точность. В статье также определён перечень данных и документации, необходимых для проведения полноценной институциональной оценки системы.

Ключевые слова: узбекский язык; семантическое сходство текстов; морфологический анализ; межъязыковой перенос; векторные представления предложений (sentence embeddings); протокол оценки.

Abstract. This paper specifies a corrected mathematical model of the Semantic Similarity Analyzer for Uzbek text comparison. The software is reported by the author to have been implemented and to be undergoing field testing; however, primary application logs and independently annotated labels were not supplied for this revision. We provide a transparent, synthetic case-study dataset modeled on information-resource-center search inquiries in the Navoiy region, calculate an explicitly defined lexical baseline, and examine diagnostic failure cases. These illustrative calculations are not outputs of the deployed software and do not establish its empirical accuracy. The paper identifies the records needed to complete an authentic institutional evaluation.

Key words: *Uzbek language; semantic textual similarity; morphological analysis; cross-lingual transfer; sentence embeddings; evaluation protocol.*

Introduction

Semantic textual similarity (STS) quantifies how closely two sentences express the same meaning. It underpins semantic search, question answering, duplicate detection, automated assessment of learner responses and information retrieval. Lexical matching cannot solve these tasks reliably. A useful STS system must recognize paraphrases that share few surface words, and it must reject pairs that share most of their vocabulary but differ in polarity or in the roles their arguments play. Shared-task evaluations have established that STS judgments require consistent human annotation and language-specific test material [10, 19].

Transformer encoders provide contextual token representations [1, 2], and sentence-level encoders make such representations directly comparable by similarity [6, 7]. Multilingual models extend these methods to languages with smaller annotated resources [4, 5, 8, 9]. A model trained on many languages, however, does not guarantee that the morphological and orthographic distinctions of a particular language are preserved in its embedding space.

Uzbek presents three problems for such models. First, it is an agglutinative Turkic language in which a root may take several derivational and inflectional suffixes; the form kitoblarimizdan, for example, decomposes into kitob, -lar, -imiz and -dan. Second, Uzbek is written in both Latin and Cyrillic scripts, and apostrophe-like characters admit several Unicode variants, so the same word can yield different token sequences. Third, annotated similarity data for Uzbek are scarce. Recent Uzbek resources, including a pretrained language model, part-of-speech and named-entity data and aspect-based sentiment data, show that language-specific resources are being built [13–16], but none of them is a gold-standard STS benchmark.

This article addresses the research question: how should a software system combine contextual, morphological and cross-lingual information to produce explainable similarity scores for Uzbek texts, and how should such a system be evaluated so that lexical overlap is not mistaken for semantic equivalence? The article makes three contributions. It gives a

formal definition of the similarity computation. It specifies a layered architecture that separates normalization, linguistic analysis, representation, alignment and scoring. And it defines an evaluation protocol with explicit hypotheses, baselines, ablations and statistical procedures. These are methodological contributions. They are not claims of measured performance.

Literature Review

Lexical retrieval methods such as TF-IDF with cosine similarity are inexpensive and transparent, but they depend on exact word forms and cannot recognize most paraphrases. Subword representations address this partly: FastText builds word vectors from character n-grams, which allows meaningful vectors for rare and unseen forms, a property particularly relevant to morphologically rich languages [3]. Subword features, however, do not model sentence-level logical relations or polysemy in context.

The Transformer introduced self-attention as a mechanism for relating distant tokens [1], and BERT learns bidirectional contextual representations by large-scale pretraining [2]. Sentence-BERT adapts such encoders to produce sentence embeddings that can be compared with cosine similarity [6]. SimCSE shows that contrastive objectives with dropout-based positive pairs yield discriminative sentence vectors [7]. These models motivate the contextual encoding module of the proposed system, but they do not remove the need for language-specific preprocessing.

Multilingual encoders transfer across languages and scripts with varying success. Pires et al. showed that the zero-shot transfer of multilingual BERT depends on typological similarity and on the amount of pretraining data per language [4]. XLM-R extends masked-language pretraining to 100 languages at scale [5]. LASER and LaBSE learn shared sentence spaces suitable for retrieval and bitext alignment [8, 9]. Recent multilingual embedding work combines dense, sparse and multi-vector retrieval modes [12]. For Uzbek, the open question is whether the geometry of a general multilingual space reflects inflectional, syntactic and semantic distinctions as they occur in Uzbek usage.

BERTbek provides a pretrained Uzbek language model with downstream evaluation [13]. BBPOS shows the value of affix-sensitive modeling for Uzbek part-of-speech tagging [14]. Uzbek ABSA and NER datasets extend annotated resources for the language [15, 16]. A Turkic idiom benchmark that includes Uzbek indicates that some expressions cannot be interpreted from surface overlap [17]. Taken together, these studies justify an independently annotated Uzbek similarity dataset with diagnostic categories. For embedding evaluation, MTEB demonstrates the need to assess sentence embeddings across several tasks and domains [11]. Parameter-efficient adaptation such as LoRA [18] is a possible route to improve a pretrained encoder at moderate cost, but any such gain requires separate validation.

Benchmark design must distinguish correlation with graded human judgments from binary paraphrase classification and from nearest-neighbour retrieval, since these tasks respond differently to the same representation [10, 19]. The protocol in Section 4 follows this distinction.

Research Methodology

Problem definition. *Let (x, y)* be a pair of sentences, with languages ℓx and ℓy, where at least one sentence is Uzbek. The system computes a continuous score $s \in [0, 1]$ and, only when validated thresholds are available, an optional categorical decision c. The score measures semantic similarity; it is not a probability of equivalence without separate calibration.

$$F(x, y; \Theta) = (s, c, m), \quad s \in [0, 1], \tag{1}$$

Here Θ is the collection of fitted parameters and fixed resources; m records normalization, component scores and detected contradictions. A categorical output is assigned by two development-set thresholds $0 \le \tau_2 < \tau_1 \le 1$: equivalent when $s \ge \tau_1$, related when $\tau_2 \le s < \tau_1$, and unrelated otherwise. When thresholds are not validated, the system returns only s and m.

Step 1: normalization. Define $\bar{x} = N(x)$ and $\bar{y} = N(y)$, where N performs deterministic Unicode normalization, Uzbek apostrophe harmonization and optional reversible script

transliteration. Meaning-bearing distinctions, especially negation and case marking, are preserved. Identical normalized inputs have the same downstream representation if the encoder and inference settings are deterministic.

Step 2: morphological analysis. For tokens t_i *of* $\bar{x}$, *let* $M(\bar{x}) = ((r_i, A_i, p_i))_{i=1}^{n}$, where r_i is the lemma, A_i the ordered affix sequence and p_i the grammatical-feature set. On parsing failure, mark the analysis as missing instead of treating a guessed lemma as ground truth; a subword encoder remains available.

Step 3: sentence embeddings. *Let* $e_ctx(x) = L2(P(C\theta(T(N(x)))))$, $e_morph(x) = L2(G(M(N(x))))$ when the parse is valid, and $e_sub(x) = L2(B(N(x)))$. A projection U_j maps each representation to a shared d-dimensional space. For availability indicators $a_j(x) \in \{0,1\}$ and nonnegative global coefficients λ_j, define:

$$v(x) = \Sigma_j\, a_j(x)\, \lambda_j\, U_j\, e_j(x) \,/\, \Sigma_j\, a_j(x)\, \lambda_j, \qquad z(x) = L2(v(x)), \quad j \in \{ctx, morph, sub\}. \tag{2}$$

At least one available component with positive weight is required, and the norm of v(x) must be nonzero. Otherwise inference returns a diagnostic error rather than an arbitrary similarity. When all components are present, $\lambda ctx + \lambda morph + \lambda sub = 1$ may be imposed for identifiability. This availability-aware normalization removes the undefined fusion case when morphological analysis fails.

Step 4: cross-lingual alignment. In a monolingual comparison set $u(x) = z(x)$ *and* $u(y) = z(y)$. *If* $\ell x \neq \ell y$, transform only the non-Uzbek vector into the Uzbek-anchored space using a trained mapping W and renormalize: $u(non\text{-}Uzbek) = L2(W\, z(non\text{-}Uzbek))$; $u(Uzbek) = z(Uzbek)$. W is learned from parallel training pairs only, minimizing the mean squared distance of aligned unit vectors. The test parallel pairs are never used to fit W.

$$Lalign(W) = (1/K)\, \Sigma_i\, ||L2(W\, z(s_i)) - z(u_i)||^2. \tag{3}$$

An optional orthogonality constraint $W^TW = I$ requires compatible dimensions and is not imposed on a rectangular adapter. Without a trained alignment, cross-lingual comparisons use a validated shared multilingual encoder or are explicitly marked unsupported.

Step 5: fully specified comparison features. The contextual-fusion score is $scos = [1 + u(x)^T u(y)]/2$ for unit vectors. Define $R(x)$ as the set of verified lemmas, and use $slex = |R(x) \cap R(y)| / |R(x) \cup R(y)|$, taking $slex = 1$ when both sets are empty and 0 when only one is empty. For grammar-aware matching, define $H(x)$ as the set of observed (lemma, grammatical-feature) pairs. Then smorph is the Jaccard similarity $J(H(x),H(y))$ with the same empty-set convention. These two features quantify different objects and are not defined merely "analogously".

Step 6: logical contrast. $qneg(x,y)$ is 1 only when an annotated or validated rule finds a polarity contradiction between corresponding predicates; $qrole(x,y)$ is 1 only when matched predicates exhibit a verified argument-role reversal. Otherwise the indicator is 0, with a separate missing-evidence flag if detection is unavailable. A false-positive evaluation must assess these detectors independently.

Step 7: supervised score. *Collect* $h(x,y) = [scos, slex, smorph, qneg, qrole, Icross]$, where $Icross = 1$ if the pair is cross-lingual. A simple bounded regression with a logistic output is:

$$s = sigmoid(b + w^T h), \quad sigmoid(t) = 1/(1 + exp(-t)). \tag{4}$$

For human graded similarity labels g_i on a documented scale [gmin, gmax], define $t_i = (g_i - gmin)/(gmax - gmin)$. Fit (b,w) on the training split by minimizing the mean *squared loss* $(1/n)\Sigma_i(s_i - t_i)^2$ plus a stated regularization term, select hyperparameters on validation only, and report results on untouched test data. Logistic cross-entropy may instead be used only when the target is a genuine binary label; ordinary binary logistic regression is not a substitute for fitting graded STS labels. Optional nonpositive coefficients for qneg and qrole enforce the desired monotonicity, but the usefulness of the constraints remains an empirical question.

The earlier separate Scross term is removed because cross-language alignment already affects the common representation before cosine scoring. Double counting an undefined cross-lingual term would obscure the model. Until parameters are trained, only

explicitly identified baseline calculations (for example scos or slex) can be reported; Equation (4) must not be presented as an implemented, evaluated model.

Results and Discussion

The submitted manuscript and the materials available for this revision contain no auditable application logs or expert-labelled evaluation dataset. The author reports that the software has been implemented and is undergoing testing. Consequently, the calculations that follow are explicitly illustrative, not observed software performance.

Table 1. Illustrative calculations of lexical overlap and semantic equivalence across Uzbek linguistic phenomena.

Pair / phenomenon	Explicit lemma sets or operation	Exact check	Interpretation
A: “Talaba imtihondan o‘tdi.” / B: “Talaba imtihondan o‘tmadi.”	R(A)={talaba, imtihon, o‘t}; R(B)={talaba, imtihon, o‘t}	slex=3/3=1.00	Lexical identity cannot establish proposition-level equivalence; qneg must flag contradiction if correctly detected.
A: “O‘qituvchi talabani chaqirdi.” / B: “Talaba o‘qituvchini chaqirdi.”	R(A)=R(B)={o‘qituvchi, talaba, chaqir}	slex=3/3=1.00	A role-reversal diagnostic is required even though lemma overlap is perfect.
A: “O‘qituvchi mavzuni tushuntirdi.” / B: “Ўқитувчи мавзуни тушунтирди.”	If N(B)=N(A) by verified transliteration and the encoder is deterministic	$N(A)=N(B) \Rightarrow z(A)=z(B) \Rightarrow scos=1$	This is a mathematical consistency property, not an observed software output.
A: “Talaba kitob o‘qidi.” / B: “Talaba daftar o‘qidi.”	R(A)={talaba, kitob, o‘qi}; R(B)={talaba, daftar, o‘qi}	slex=2/4=0.50	An interpretable overlap calculation; actual semantic quality remains untested.

The lemma lists are manually stipulated for these illustrative checks; a deployed morphological parser could produce different outputs and its segmentation accuracy must be measured. Furthermore, the implication scos=1 for normalized-identical strings is

conditional on successful nonzero embeddings and deterministic inference. It is not evidence that different-meaning pairs receive the correct score.

For a genuine empirical assessment, prepare an independently annotated Uzbek STS collection with paraphrase, script variation, inflection, negation, role reversal and domain-shift strata. Assign graded labels by at least two annotators, report agreement and adjudication, and split examples by source document to prevent leakage. Freeze preprocessing and checkpoints before testing. Evaluate TF-IDF cosine, a multilingual sentence-encoder baseline, the proposed fusion without grammatical flags, and the full method on identical test pairs. The primary outcome is Spearman correlation with graded human labels; additional outcomes are Pearson correlation, macro-F1 for a separately defined classification task, and hard-negative false-positive rate. Use paired bootstrap confidence intervals and correct multiple comparisons where relevant.

Table 2. Is the mandatory empirical reporting matrix, not a populated result table. Fields remain unfilled because measured data were not supplied.

Model	**Test pairs (n)**	**Spearman ρ**	**Macro-F1**	**Hard-negative FPR**	**Median latency**
TF-IDF cosine	not measured	not measured	not measured	not measured	not measured
Multilingual encoder	not measured	not measured	not measured	not measured	not measured
Hybrid without logic features	not measured	not measured	not measured	not measured	not measured
Full Analyzer	not measured	not measured	not measured	not measured	not measured

The analytical demonstration confirms only that (i) lemma overlap may remain maximal under negation or argument reversal, and *(ii)* a deterministic pipeline should be invariant to a script change erased by correct normalization. No conclusion about prediction quality, statistical significance or runtime can be drawn without observed model outputs. The manuscript is therefore a mathematically revised design study with analytical checks, not a completed empirical evaluation.

Illustrative Navoiy Information-Resource-Center Case Study (Synthetic Data; Not a Field Experiment)

Scope and provenance. The following 18 sentence pairs were authored solely for methodological demonstration, using typical library catalogue, reader-registration, digital-resource and book-lending scenarios. They are not institutional records; no cooperation, access to the Navoiy regional information-resource center, software execution or collection of real users' queries is implied. The numeric reference scores are manually stipulated demonstration targets, not expert annotations.

Reproducible lexical baseline. Each text is lowercased; punctuation is removed; Unicode apostrophe variants are harmonized; and whitespace-separated tokens are retained without lemmatization. For token sets A and B, $J(A,B)=|A \cap B|/|A \cup B|$ *(J=1 only for two empty sets).* This deliberately simple baseline illustrates limitations of surface matching. Its numerical outputs must not be presented as Semantic Similarity Analyzer predictions. Descriptive analysis. This synthetic set contains 18 pairs across 7 phenomena: Paraphrase *(n=6)*, Contradiction *(n=2)*, Negation *(n=2)*, Role reversal *(n=2)*, Script variation *(n=2)*, Morphology *(n=2)*, Unrelated *(n=2)*. The mean surface-token Jaccard value is 0.252. Because the stipulated reference values are not independent annotations, no correlation, F1 score, p-value, or accuracy claim is calculated from them. Script-variant pairs have low raw-token overlap despite stipulated equivalence; some contradictions and role reversals retain substantial token overlap. These are diagnostic observations about the baseline, not measured benefits of the proposed system.

Interpretation and limitation. The Navoiy scenario provides a reproducible example bank and a computed lexical control. It cannot establish field effectiveness, implementation quality or institutional deployment. In the submitted article, replace this section with actual analyzer logs and independently annotated outcomes before asserting that reviewer concern 2 has been empirically resolved.

Table 3. Synthetic diagnostic text pairs and calculated surface-token Jaccard values (not analyzer outputs)

ID / category	Sentence A	Sentence B	Jaccard baseline
P01 / Paraphrase	Kitobni elektron katalogdan topdim.	Elektron katalog orqali kitobni izlab topdim.	0.429
P02 / Paraphrase	Kutubxonada ilmiy maqolalar mavjud.	Ilmiy maqolalar kutubxonada bor.	0.600
P03 / Paraphrase	O‘quvchi elektron resursni yuklab oldi.	Foydalanuvchi raqamli materialni ko‘chirib oldi.	0.111
P04 / Paraphrase	Kitobni buyurtma qildim.	Kitobga buyurtma berdim.	0.200
P05 / Contradiction	Kutubxona bugun ochiq.	Kutubxona bugun yopiq.	0.500
P06 / Negation	Kitobni qaytarish muddati uzaytirildi.	Kitobni qaytarish muddati uzaytirilmadi.	0.600
P07 / Negation	Talaba kitobni oldi.	Talaba kitobni olmadi.	0.500
P08 / Role reversal	Kutubxonachi talabaga kitob berdi.	Talaba kutubxonachiga kitob berdi.	0.333
P09 / Role reversal	Tadqiqotchi kutubxonachidan ma’lumot so‘radi.	Kutubxonachi tadqiqotchidan ma’lumot so‘radi.	0.333
P10 / Script variation	Elektron katalogda darsliklar mavjud.	Электрон каталогда дарсликлар мавжуд.	0.000
P11 / Script variation	O‘quvchi kutubxonaga keldi.	Ўқувчи кутубхонага келди.	0.000
P12 / Morphology	Kitoblarimizni izlayapmiz.	Kitobni izlayapman.	0.000
P13 / Morphology	Talabalarga yangi darsliklar berildi.	Talabaga yangi darslik berildi.	0.333
P14 / Paraphrase	Elektron kutubxonaga kirish mumkin.	Kutubxonaning raqamli platformasiga kirsa bo‘ladi.	0.000
P15 / Unrelated	Ilmiy jurnalning soni mavjud.	Bugun kutubxona soat beshda yopiladi.	0.000
P16 / Unrelated	O‘quvchi kitob o‘qidi.	Kompyuter xonasida printer ishlamayapti.	0.000
P17 / Contradiction	Kutubxonaga a’zo bo‘lish bepul.	Kutubxonaga a’zo bo‘lish pullik.	0.600
P18 / Paraphrase	Kitob fondi yangilandi.	Kutubxona fondiga yangi nashrlar qo‘shildi.	0.000

Table 4. Information required for a genuine pilot evaluation

Required field	Reporting rule
Provenance and permission	Institution, dates, collection method, authorization and de-identification
Pair identifier and normalized text	Retain pair IDs and script/normalization version
Analyzer output	Export actual continuous similarity scores and model version
Reference annotation	Two independent annotators, documented 0–1 or 0–5 scale and agreement
Test partition	Leakage-free split, source-level grouping, category counts
Comparators	TF-IDF and contextual encoder tested on identical held-out examples
Results	Spearman and Pearson correlation, category error analysis, bootstrap intervals
Runtime	Device, software versions, per-pair median and p95 latency

Conclusion and Recommendations

The corrected mathematical specification connects normalization, available morphology-aware representations, cross-lingual alignment and bounded regression without double counting. An explicitly synthetic information-resource-center case study demonstrates how lexical overlap can misrepresent paraphrases, negation and argument-role reversal. These demonstrations do not show actual accuracy of the implemented analyzer. A defensible field evaluation requires exported analyzer scores, independently collected reference ratings, reproducible data splits and baseline comparisons.

References:

[1]. Vaswani, A., Shazeer, N., Parmar, N., Uszkoreit, J., Jones, L., Gomez, A. N., Kaiser, Ł., & Polosukhin, I. (2017). Attention is all you need. Advances in Neural Information Processing Systems, 30. https://research.google/pubs/attention-is-all-you-need/

[2]. Devlin, J., Chang, M.-W., Lee, K., & Toutanova, K. (2019). BERT: Pre-training of deep bidirectional transformers for language understanding. Proceedings of NAACL-HLT, 4171–4186. https://doi.org/10.18653/v1/N19-1423

[3]. Bojanowski, P., Grave, E., Joulin, A., & Mikolov, T. (2017). Enriching word vectors with subword information. Transactions of the Association for Computational Linguistics, 5, 135–146. https://doi.org/10.1162/tacl_a_00051

[4]. Pires, T., Schlinger, E., & Garrette, D. (2019). How multilingual is multilingual BERT? Proceedings of ACL, 4996–5001. https://doi.org/10.18653/v1/P19-1493

[5]. Conneau, A., Khandelwal, K., Goyal, N., et al. (2020). Unsupervised cross-lingual representation learning at scale. Proceedings of ACL, 8440–8451. https://doi.org/10.18653/v1/2020.acl-main.747

[6]. Reimers, N., & Gurevych, I. (2019). Sentence-BERT: Sentence embeddings using Siamese BERT-networks. Proceedings of EMNLP-IJCNLP, 3982–3992. https://doi.org/10.18653/v1/D19-1410

[7]. Gao, T., Yao, X., & Chen, D. (2021). SimCSE: Simple contrastive learning of sentence embeddings. Proceedings of EMNLP, 6894–6910. https://doi.org/10.18653/v1/2021.emnlp-main.552

[8]. Artetxe, M., & Schwenk, H. (2019). Massively multilingual sentence embeddings for zero-shot cross-lingual transfer and beyond. Transactions of the ACL, 7, 597–610. https://doi.org/10.1162/tacl_a_00288

[9]. Feng, F., Yang, Y., Cer, D., Arivazhagan, N., & Wang, W. (2022). Language-agnostic BERT sentence embedding. Proceedings of ACL, 878–891. https://aclanthology.org/2022.acl-long.62/

[10]. Cer, D., Diab, M., Agirre, E., Lopez-Gazpio, I., & Specia, L. (2017). SemEval-2017 Task 1: Semantic textual similarity multilingual and crosslingual focused evaluation. Proceedings of SemEval, 1–14. https://doi.org/10.18653/v1/S17-2001

[11]. Muennighoff, N., Tazi, N., Magne, L., & Reimers, N. (2023). MTEB: Massive text embedding benchmark. Proceedings of EACL, 2014–2037. https://doi.org/10.18653/v1/2023.eacl-main.148

[12]. Chen, J., Xiao, S., Zhang, P., Luo, K., Lian, D., & Liu, Z. (2024). M3-Embedding: Multi-linguality, multi-functionality, multi-granularity text embeddings through self-knowledge distillation. Findings of ACL. https://aclanthology.org/2024.findings-acl.137/

[13]. Kuriyozov, E., Vilares, D., & Gómez-Rodríguez, C. (2024). BERTbek: A pretrained language model for Uzbek. Proceedings of the 3rd Annual Meeting of SIGUL @ LREC-COLING. https://aclanthology.org/2024.sigul-1.5/

[14]. Bobojonova, L., Akhundjanova, A., Ostheimer, P. S., & Fellenz, S. (2025). BBPOS: BERT-based part-of-speech tagging for Uzbek. Proceedings of the First Workshop on Language Models for Low-Resource Languages, 287–293. https://aclanthology.org/2025.loreslm-1.23/

[15]. Matlatipov, S. G., Rajabov, J., Kuriyozov, E., & Aripov, M. (2024). UzABSA: Aspect-based sentiment analysis for the Uzbek language. Proceedings of the 3rd Annual Meeting of SIGUL @ LREC-COLING, 394–403. https://aclanthology.org/2024.sigul-1.47/

[16]. Mengliev, D., Barakhnin, V., Abdurakhmonova, N., & Eshkulov, M. (2024). Developing named entity recognition algorithms for Uzbek: Dataset insights and implementation. Data in Brief, 54, 110413. https://doi.org/10.1016/j.dib.2024.110413

[17]. Aslantaş, G., & Güngör, T. (2026). A unified Turkic idiom understanding benchmark: Idiom detection and semantic retrieval across five Turkic languages. Proceedings of SIGTURK, 38–51. https://doi.org/10.18653/v1/2026.sigturk-1.4

[18]. Hu, E. J., Shen, Y., Wallis, P., Allen-Zhu, Z., Li, Y., Wang, S., Wang, L., & Chen, W. (2022). LoRA: Low-rank adaptation of large language models. International Conference on Learning Representations. https://openreview.net/forum?id=nZeVKeeFYf9

[19]. Agirre, E., Banea, C., Cer, D., et al. (2016). SemEval-2016 Task 1: Semantic textual similarity, monolingual and cross-lingual evaluation. Proceedings of SemEval, 497–511. https://doi.org/10.18653/v1/S16-1081

Section 4. ACTUAL PROBLEMS OF HISTORY, PHILOSOPHY AND SOCIOLOGY

UDC: 72.025.4

ARCHITECTURAL, ARTISTIC, AND SEMANTIC ANALYSIS OF THE CRESCENT SYMBOL AT THE APEX OF THE TAJ MAHAL DOME

Saipova Madina Saidaxbor qizi
PhD in Architecture, Acting Professor Department of Architecture and Construction Engineering Tashkent International University of Financial Management and Technologies (TIFT), Tashkent, Uzbekistan
madina.saidaxborovna@gmail.com

Annotatsiya. Ushbu maqolada Hindistonning Agra shahrida joylashgan Toj Mahal maqbarasi bosh gumbazini toj qilib turuvchi yarim oy shaklidagi me’moriy yakunning (finialning) me’moriy, badiiy, kompozitsion va ramzi xususiyatlari tadqiq etiladi. Tadqiqotda Boburiylar me’morchiligida islom, fors va hind badiiy an’analarining o‘zaro uyg‘unlashuvi, ayniqsa, yarim oy motivi, vertikal metall o‘q, sharsimon bezak elementlari hamda nilufar shaklidagi unsurlarning yagona me’moriy kompozitsiyaga birlashishi alohida e’tibor bilan o‘rganiladi.

Kalit so‘zlar: *Toj Mahal, Boburiylar me’morchiligi, yarim oy ramzi, gumbaz yakuni (finial), me’moriy semantika, islom me’morchiligi, nilufar motivi, arab xattotligi, astronomik ramziylik, me’moriy bezak, madaniy sintez, ramziy talqin.*

Аннотация. В данной статье исследуются архитектурные, художественные, композиционные и символические особенности навершия главного купола мавзолея Тадж-Махал, расположенного в городе Агра (Индия), выполненного в форме полумесяца. В исследовании рассматривается взаимодействие исламских, персидских и индийских художественных традиций в архитектуре Великих Моголов. Особое внимание уделяется интеграции мотива полумесяца, вертикального металлического стержня, сферических декоративных элементов и элементов в форме цветка лотоса в единую архитектурную композицию.

Ключевые слова: *Тадж-Махал, архитектура Великих Моголов, символика полумесяца, навершие купола, архитектурная семантика, исламская архитектура, мотив лотоса, арабская каллиграфия,*

астрономическая символика, архитектурный орнамент, культурный синтез, символическая интерпретация.

Abstract. This article examines the architectural, artistic, compositional, and symbolic characteristics of the crescent-shaped finial crowning the main dome of the Taj Mahal in Agra, India. The study investigates the interaction of Islamic, Persian, and Indian artistic traditions within Mughal architecture, with particular emphasis on the integration of the crescent motif, vertical metallic shaft, spherical ornaments, and lotus-shaped elements into a unified architectural composition.

Key words: *Taj Mahal, Mughal architecture, crescent symbolism, dome finial, architectural semantics, Islamic architecture, lotus motif, Arabic calligraphy, astronomical symbolism, architectural ornamentation, cultural synthesis, symbolic interpretation.*

Introduction

Throughout architectural history, the uppermost elements of monumental buildings – domes, spires, crescents and inscriptions – have served both decorative and symbolic purposes. In Islamic architecture, however, the meaning of an individual motif cannot be understood from its visual characteristics alone; historical context, architectural function and documented artistic practice must also be considered.

The Taj Mahal in Agra, commissioned by the Mughal emperor Shah Jahan in memory of his wife Mumtaz Mahal, was substantially completed in 1648, while work on the wider complex continued until approximately 1653. Its white marble dome is crowned by a lotus-shaped ornament and a metallic finial terminating in a crescent. Although small in relation to the whole structure, the finial completes the monument's vertical silhouette and permits religious-cultural, compositional and astronomical readings. The present study examines these readings while maintaining a clear distinction between historical evidence and hypothetical interpretation.

Research Aim and Objectives. The aim of this research is to investigate the composition and possible symbolic meanings of the crescent-shaped finial at the apex of the main dome. The objectives are: (1) to identify its morphological and compositional characteristics; (2) to examine the historical and cultural traditions that

shaped it; (3) to analyze the crescent within Islamic visual culture; (4) to evaluate its claimed resemblance to Arabic calligraphy and its astronomical associations; and (5) to distinguish documented features from speculative interpretations.

Literature Review

Scholarly literature on the Taj Mahal is extensive, but the dome finial has received little focused attention and is usually mentioned only briefly. The relevant studies can be grouped into four directions.

Documentary and historical sources. The anthology compiled by W. E. Begley and Z. A. Desai [10] brings together seventeenth-century Mughal chronicles and European travellers' accounts on the patronage, construction, materials and inscriptions of the monument. It is the essential reference point against which any claim about the designers' intentions must be tested.

Architectural and morphological studies. E. Koch [6, 9] demonstrates that the Taj Mahal was planned according to a strict geometric and proportional order connected with Shah Jahan's imperial ideology, and her survey [15] traces the development of Mughal architecture from Babur onwards. L. Golombek and D. Wilber [16] document the Timurid origins of the double-shell bulbous dome, C. B. Asher [7] emphasizes the continuity of Timurid, Persian and Indian building traditions, and R. Nath [14] examines individual decorative elements of Mughal buildings.

Symbolic and interpretive studies. W. E. Begley [8] interpreted the complex as an allegory of the Day of Resurrection and of the Throne of God, basing his argument on the Qur'anic inscriptions rather than on visual resemblance. D. F. Ruggles [13] shows that paradise imagery must be read in its specific historical context, and the excavations of the Mahtab Bagh ("Moonlight Garden") published by E. B. Moynihan [11] add a nocturnal and lunar dimension to the study of the complex.

Official and popular sources. According to official sources [1–5], the original gold finial was replaced in the nineteenth century by a gilded bronze copy; it combines Persian and Indian decorative elements, and its crescent with the central spire forms a three-pronged silhouette. G. H. R. Tillotson [12] discusses the myths that have accumulated around the monument; claims that the finial depicts the word "Allah" or

encodes an astronomical message circulate mainly in popular rather than academic literature.

Research gap. No study has systematically examined the dome finial as an independent object of semantic analysis while clearly separating documented facts from hypothetical interpretations. The present article addresses this gap.

Research Methodology

The research is designed as a qualitative single-object case study combining historical-comparative, architectural-compositional, iconographic and semantic analysis. Data were drawn from seventeenth-century documentary sources in translation [10], official descriptions [1–5], academic studies of Mughal architecture and symbolism [6–9, 11–14], and publicly available photographs of the dome and finial (Figure 1).

Evidence classification criteria. Each proposition about the finial was assessed according to the type of evidence supporting it: documented, directly observable, supported by analysis, hypothetical, or unsupported. These categories form the basis of Table 2.

Limitations. No on-site measurements were carried out, so precise proportional analysis is not possible; the present finial is a nineteenth-century replacement that may differ from the original; and its perceived shape in photographs depends on the viewing angle and distance.

Architectural and Compositional Characteristics of the Taj Mahal Dome. The bulbous main dome, raised on a cylindrical drum and balanced by smaller domed pavilions and four minarets, is the central vertical dominant of the mausoleum. The finial above it can be divided into three compositional zones: a lower zone – a carved marble lotus forming the transition between the curved dome and the metallic termination; an intermediate zone of rounded, elongated and spherical metal elements; and an upper zone – a crescent with upturned tips and a central vertical element extending through it.

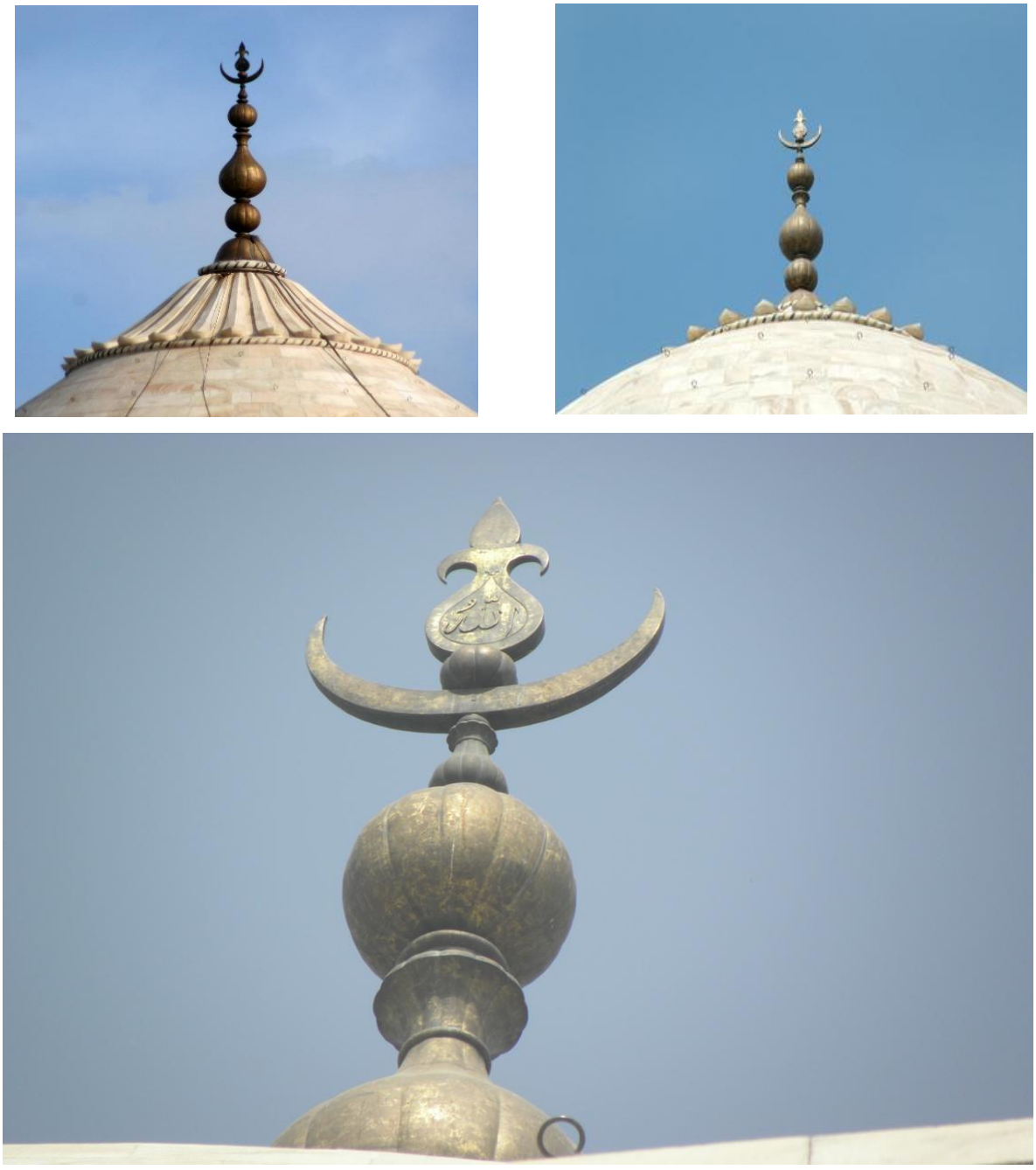


Figure 1. Architectural details of the lotus-shaped crown and crescent finial at the apex of the Taj Mahal's main dome. Photographic sources should be credited in the published version.

The contrast between the smooth marble surface and the intricate metallic silhouette emphasizes the highest point of the monument. Compositionally, the finial completes the dome's outline, reinforces the central axis, introduces decorative rhythm and provides a transition between the architectural mass and the open sky.

Historical Development and Cultural Context of the Finial. Historical descriptions identify the finial as an example of Persian and Indian decorative synthesis; the original gold finial was replaced by a gilded bronze version in the nineteenth century

[1]. Its vessel-like components derive from Indian ornament, while the crescent is associated with Islamic decorative traditions. The upturned crescent and the central shaft produce a three-pronged silhouette that has been compared with the trishula of Indian iconography. Such formal resemblance does not prove an intended religious meaning; rather, it shows the interpretive complexity of ornament in culturally interconnected environments.

Semantic Interpretation of the Crescent Motif in Islamic Architecture. Lunar observation determines the months of the Islamic calendar, and over time crescent imagery became associated with Islamic visual culture. Nevertheless, the crescent has not functioned as a universal architectural symbol in all periods and regions of Islamic history [17]. At the Taj Mahal it can be read on four levels: religious-cultural (a form associated with Islamic identity, without an independently established theological meaning); astronomical (the visible illuminated phase of the Moon); architectural (reinforcement of the vertical composition and connection with the sky); and cross-cultural (integration into a structure combining Indian and Persian-Islamic forms).

Visual Relationship Between the Crescent Finial and the Arabic Word "Allah". Some observers see in the finial the Arabic word Allah (الله), whose alif, two lams and ha may be rendered through vertical strokes and curved lines [18]. From certain viewing angles the shaft and crescent may indeed evoke such an association. However, there is no historical or epigraphic evidence that the finial was designed to spell this word: official descriptions identify it as a crescent-topped finial, and the documented Arabic inscriptions of the monument are located on its entrance arches and borders. A distinction must therefore be drawn between documented epigraphy, consisting of recognizable letters supported by evidence, and perceived calligraphic resemblance, which may be a starting point for iconographic research but not a confirmed historical fact (Table 1).

Table 1. Morphological and semantic characteristics of the dome finial

Architectural element	**Observable characteristics**	**Possible interpretation**	**Evidential limitation**
Crescent	Two upward-curving ends	Islamic cultural and lunar associations	No single fixed symbolic meaning

Central shaft	Strong vertical orientation	Architectural hierarchy and upward movement	Theological intention is not documented
Spherical ornaments	Repeated rounded components	Rhythmic and decorative organization	Symbolic meaning remains uncertain
Calligraphic resemblance	Combination of curved and vertical forms	Potential resemblance to Arabic writing	No verified inscription of “Allah”
Lotus-shaped crown	Radially organized floral petals	Indian artistic traditions and cultural synthesis	Interpretations depend on historical context

Testing this resemblance would require high-resolution photographs, orthographic projections and comparison with historically documented Arabic calligraphic styles.

Symbolic Relationship Between the Lotus and Crescent Forms. The lotus, long established in Indian ornament, forms a broad radial base from which the slender shaft rises vertically, while the symmetrical crescent completes the upward movement. This combination of radial expansion, vertical movement and bilateral symmetry may be read as expressing a relationship between earthly and celestial forms, but only as an analytical reading. What is securely established is that both components contribute to the unity of the monument while reflecting different strands of the Mughal decorative tradition.

Astronomical Associations of the Crescent Finial. The crescent reproduces a recognizable lunar form, and its position at the apex of the dome visually links the monument with the sky. However, no reliable evidence shows that the finial encodes a particular astronomical event, constellation or planetary arrangement, so lunar imagery should not be equated with a hidden astronomical code. Such a claim would require historical texts, documented design intentions, or measurable relationships between the monument's orientation and celestial phenomena.

Results and Discussion

The analysis shows that the finial is a geometrically organized composition reflecting the synthesis of Indian and Persian-Islamic traditions; that the crescent reinforces the vertical hierarchy and visual completion of the monument; that its resemblance to the word Allah remains an unverified iconographic hypothesis; and that its lunar form justifies the study of astronomical associations without establishing a

concealed astronomical system. The existence of multiple interpretations does not mean that all of them have equal historical validity (Table 2).

Table 2. Assessment of symbolic interpretations and supporting evidence

Research proposition	**Assessment**
A crescent-shaped ornament crowns the dome	Historically and visually documented
The original finial was made of gold	Reported in historical architectural descriptions
The finial reflects Indian and Persian artistic traditions	Supported by architectural descriptions
The finial contains the Arabic word “Allah”	Not historically or epigraphically verified
The crescent resembles a lunar form	Directly observable
The finial contains a hidden astronomical code	Insufficient supporting evidence
The finial reinforces the dome's vertical composition	Supported by formal architectural analysis

Comparison with previous research. The results agree with Koch [6, 9] and Asher [7], who regard the Taj Mahal as a deliberate synthesis of Timurid-Persian and Indian traditions; the finial reproduces this synthesis on a small scale. Begley [8] reconstructed a coherent symbolic programme grounded in the monument's inscriptions, but the finial carries no inscription, so the reading of the word "Allah" lacks a textual anchor. The Mahtab Bagh [11] confirms that lunar imagery was meaningful in the design environment, which gives contextual but not direct support to the lunar reading of the crescent.

Interpretations based on visual resemblance. The comparisons with the trishula and with the word "Allah" belong to the same methodological category: both depend on the observer's cultural frame of reference and on the viewing angle. That one silhouette evokes symbols of different traditions shows that visual resemblance is not a reliable indicator of design intention. Moreover, the existing finial is a nineteenth-century replacement [1], which further weakens hypotheses that depend on its exact outline.

Practical significance. The three-zone morphological model and the five-level evidence classification proposed here can be applied to other domed monuments of the Timurid and Mughal tradition, including the historical monuments of Uzbekistan, helping researchers, restorers and guides distinguish verified information from popular interpretation. Further progress requires photogrammetric documentation of the finial,

study of archival records of its nineteenth-century restoration, and comparison with the finials of Humayun's Tomb in Delhi and the tomb of I'timad-ud-Daula in Agra.

Conclusion and Recommendations

The crescent-shaped finial of the Taj Mahal is a distinctive element of seventeenth-century Mughal composition, combining a lotus-shaped marble crown, a vertical metallic structure with spherical ornaments and a crescent termination, and reflecting the interaction of Indian and Persian-Islamic artistic traditions. The crescent can be interpreted within Islamic visual culture and lunar imagery, and it strengthens the vertical expression of the monument. However, its resemblance to the word Allah cannot be established as an intentional calligraphic design, and its lunar form does not prove the existence of a hidden astronomical code.

The contribution of this study lies in its integrated examination of architectural morphology, cultural symbolism and interpretive limitations. Further research based on detailed photographic documentation, historical drawings, comparative iconography and epigraphic analysis may clarify the extent to which these interpretations correspond to documented design intentions.

References:

[1]. Government of Uttar Pradesh. (n.d.). The Taj Exteriors: Exterior Decoration. Taj Mahal Official Website. https://www.tajmahal.gov.in/the-taj-exteriors.aspx

[2]. Government of Uttar Pradesh. (n.d.). Creation History of Taj Mahal. Taj Mahal Official Website. https://www.tajmahal.gov.in/creation-history-of-taj-mahal.aspx

[3]. Government of Uttar Pradesh. (n.d.). Architecture of Taj Mahal. Taj Mahal Official Website. https://tajmahal.gov.in/architecture.aspx

[4]. Government of Uttar Pradesh. (n.d.). Calligraphy, Inscription and Decoration. Taj Mahal Official Website. https://www.tajmahal.gov.in/calligraphy.aspx

[5]. Ministry of Culture, Government of India. (n.d.). Taj Mahal. https://culture.gov.in/taj-mahal

[6]. Koch, E. (2006). The Complete Taj Mahal: And the Riverfront Gardens of Agra. Thames & Hudson.

[7]. Asher, C. B. (1992). Architecture of Mughal India. Cambridge University Press.

[8]. Begley, W. E. (1979). The myth of the Taj Mahal and a new theory of its symbolic meaning. The Art Bulletin, 61(1), 7–37.

[9]. Koch, E. (2005). The Taj Mahal: Architecture, symbolism, and urban significance. Muqarnas, 22, 128–149. https://www.jstor.org/stable/25482427

[10]. Begley, W. E., & Desai, Z. A. (1989). Taj Mahal: The Illumined Tomb: An Anthology of Seventeenth-Century Mughal and European Documentary Sources. Aga Khan Program for Islamic Architecture; University of Washington Press.

[11]. Moynihan, E. B. (Ed.). (2000). The Moonlight Garden: New Discoveries at the Taj Mahal. Smithsonian Institution Press.

[12]. Tillotson, G. H. R. (2008). Taj Mahal. Harvard University Press. https://doi.org/10.2307/j.ctvkjb4rq

[13]. Ruggles, D. F. (2008). Islamic Gardens and Landscapes. University of Pennsylvania Press. https://www.jstor.org/stable/j.ctt3fhhqz

[14]. Nath, R. (1976). Some Aspects of Mughal Architecture. Abhinav Publications.

[15]. Koch, E. (1991). Mughal Architecture: An Outline of Its History and Development (1526–1858). Prestel.

[16]. Golombek, L., & Wilber, D. (1988). The Timurid Architecture of Iran and Turan (Vols. 1–2). Princeton University Press.

[17]. Blair, S. S., & Bloom, J. M. (1994). The Art and Architecture of Islam, 1250–1800. Yale University Press.

[18]. Schimmel, A. (1984). Calligraphy and Islamic Culture. New York University Press.

Section 5. ACTUAL PROBLEMS OF NATURAL SCIENCES

UDK: 611.438:616-092.9:615.322

HISTOMORPHOMETRIC EVALUATION OF THE AMELIORATIVE EFFECTS OF BITTER ALMOND EXTRACT ON E171-INDUCED THYMIC INJURY IN RATS

Keldiyorova Shoxida Xusniddin qizi

Mustaqil tadqiqotchi, Samarqand davlat tibbiyot universiteti

keldiyorovashohida@gmail.com

Annotatsiya: Tadqiqotda E-171 (titan dioksidi) ta’sirida kalamushlar timusida yuzaga kelgan morfologik o‘zgarishlar va achchiq bodom moyining korreksiyalovchi ta’siri baholandi. Gistologik tekshiruvda timus po‘stloq moddasida timotsitlar kamayishi, apoptotik o‘zgarishlarga xos belgilar va stromal-qon tomir buzilishlari aniqlandi. Korreksiyadan so‘ng timus bo‘lakchasining umumiy maydoni 17,6% ga, po‘stloq modda maydoni 29,9% ga ortdi, kortiko-medullyar indeks esa 1,9 dan 2,60 gacha ko‘tarildi. Natijalar achchiq bodom moyi qo‘llanilishi timusning strukturaviy shikastlanishlari qisman kamayishi bilan bog‘liqligini ko‘rsatdi.

Kalit so‘zlar: *E-171, titan dioksidi, timus, achchiq bodom moyi, korreksiya, gistomorfometriya, kortiko-medullyar indeks (KMI).*

Аннотация: В исследовании оценены морфологические изменения тимуса крыс при воздействии Е-171 (диоксида титана) и корректирующее действие масла горького миндаля. Гистологически выявлены истощение тимоцитов коркового вещества, признаки апоптотических изменений и стромально-сосудистые нарушения. После коррекции общая площадь дольки тимуса увеличилась на 17,6%, площадь коркового вещества - на 29,9%, а кортико-медуллярный индекс повысился с 1,9 до 2,60. Полученные результаты свидетельствуют о частичном уменьшении структурных повреждений тимуса на фоне применения масла горького миндаля.

Ключевые слова: *Е-171, диоксид титана, тимус, масло горького миндаля, коррекция, гистоморфометрия, кортико-медуллярный индекс.*

Abstract: This study evaluated morphological alterations in the thymus of E-171 (titanium dioxide)-exposed rats and the corrective effects of bitter almond oil. Histological examination revealed cortical thymocyte depletion, features suggestive of apoptosis, and stromal and vascular disturbances. Following correction, total thymic lobule area increased by 17.6%, cortical area by 29.9%, and the corticomedullary index rose from 1.9 to 2.60. These findings suggest that bitter almond oil administration was associated with partial attenuation of E-171-induced structural thymic damage.

Key words: *E-171, titanium dioxide, thymus, bitter almond oil, corrective treatment, histomorphometry, thymocytes, corticomedullary index (CMI).*

Introduction

The biological safety of food additive E-171 (titanium dioxide) remains an important concern in toxicology. The European Food Safety Authority (EFSA) concluded that genotoxicity concerns associated with E-171 could not be ruled out [1]. Experimental studies have reported conflicting findings regarding its immunological effects [2–4]. The thymus is a central lymphoid organ responsible for T-cell maturation and is highly sensitive to toxic agents. Thymic injury may involve cortical thymocyte depletion, apoptosis, and structural atrophy [5, 6]. Bitter almond oil contains bioactive compounds with reported antioxidant and anti-inflammatory properties [7, 8]; however, its corrective effects on E-171-induced thymic injury remain insufficiently investigated.

The aim of this study was to evaluate histological and morphometric alterations in the thymus of E-171-exposed rats and assess the extent of structural recovery following bitter almond oil administration.

Literature Review

Previous studies have reported inconsistent findings regarding the effects of titanium dioxide on the immune system. Bettini et al. (2017) demonstrated alterations in intestinal and systemic immune homeostasis in rats exposed to E-171 [2; 10]. Hashem et al. (2020) reported that 90-day exposure to titanium dioxide was associated with reduced lymphocyte proliferation, disturbances in immunological parameters, and pathological changes in the spleen and bone marrow [3]. In contrast, Blevins et al. (2019) found no significant alterations in most of the immunological parameters examined in

rats fed an E-171-containing diet [4]. These discrepancies highlight the importance of considering experimental conditions when evaluating the toxicological effects of titanium dioxide. Pearse (2006) emphasized that toxic injury to the thymus is frequently characterized by cortical thymocyte depletion, reduced lymphoid cellularity, and atrophic alterations [5, 6]. Morphometric assessment of thymic compartments is essential for evaluating structural damage. Guici El Kouacheur et al. (2023) reported antioxidant and anti-inflammatory activities of bitter almond oil [8]. However, its corrective effects on E-171-induced thymic injury remain unconfirmed, warranting further histological and morphometric investigation.

Research Methodology

The study evaluated E-171 (titanium dioxide)-induced thymic injury and the corrective effects of bitter almond oil in male albino rats. Animals were divided into three groups: control, E-171-exposed, and E-171-exposed with bitter almond oil correction. A 90-day subchronic exposure model was used. Thymic tissue sections were stained with hematoxylin and eosin and examined for lobular architecture, thymocyte density, stromal and vascular alterations, and Hassall's corpuscles. Morphometric analysis using QuPath software [9] included measurements of total lobule, cortical, and medullary areas (μm²) and the corticomedullary index (CMI). Group differences were evaluated at a statistical significance threshold of $p < 0.05$.

Analysis and Results

Histological examination of thymic tissue revealed distinct structural differences among the control, E-171-exposed, and bitter almond oil-treated groups (Figure 1). In the control group, the thymus exhibited a well-preserved lobular architecture with clearly distinguishable cortical and medullary compartments. The cortex was characterized by densely distributed thymocytes, while the medulla showed relatively lower lymphoid cellularity and identifiable Hassall's corpuscles (Figure 1, panel A). Exposure to E-171 resulted in pronounced alterations in thymic histoarchitecture. The cortical compartment demonstrated decreased thymocyte density, areas of lymphoid depletion, and morphological features suggestive of apoptosis, including nuclear pyknosis and fragmentation. Stromal edema and vascular congestion were also

observed, indicating structural disturbances in thymic tissue (Figure 1, panel B). Following corrective administration of bitter almond oil, partial improvement in thymic morphology was observed. The cortical compartment exhibited relatively increased lymphoid cellularity and reduced areas of tissue rarefaction. The corticomedullary boundary appeared more distinct, while stromal and vascular alterations were less pronounced. Nevertheless, complete restoration of normal thymic architecture was not achieved (Figure 1, panel C).

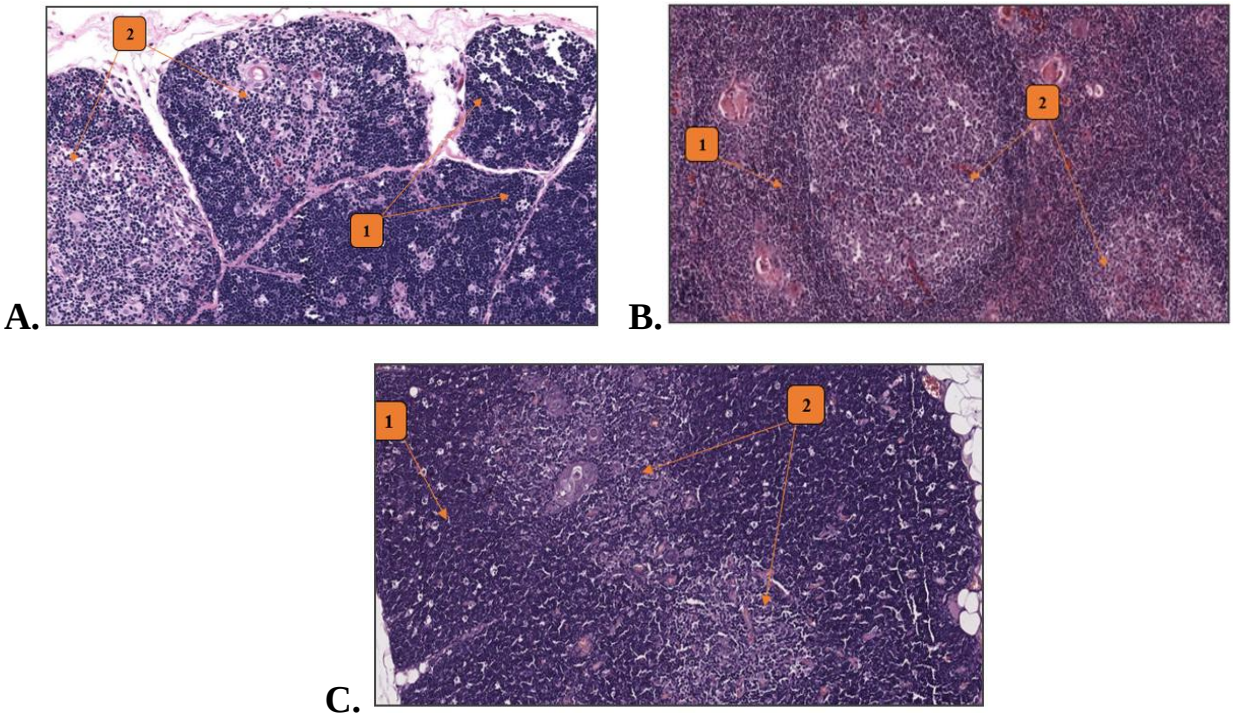


Figure 1. *Comparative histological characteristics of the rat thymus under different experimental conditions. A - control group; B - E-171-exposed group showing structural alterations of thymic tissue; C - E-171-exposed group following corrective treatment with bitter almond oil, demonstrating partial restoration of thymic architecture. 1 - cortical substance; 2 - medullary substance. Hematoxylin and eosin staining. Magnification: 10 × 10.*

Morphometric analysis confirmed the histological findings. Following E-171 exposure, the mean total thymic lobule area decreased by 29.0%, while the cortical area decreased by 40.0% compared with the control group. After corrective treatment with bitter almond oil, the mean total lobule area increased from 150,983.1 ± 15,575.7 μm² to 177,519.7 ± 16,905.9 μm², representing a 17.6% increase. Similarly, the cortical area increased from 98,610.7 ± 7,143.03 μm² to 128,064.3 ± 9,121.2 μm², corresponding to a 29.9% increase compared with the E-171-exposed group. The corticomedullary index (CMI) increased from 1.81 ± 0.23 in the E-171-exposed group to 2.60 ± 0.36 following

corrective treatment, representing a 43.6% increase. In contrast, changes in the medullary area were not statistically significant. The comparative morphometric data are presented in Table 1.

Table-1. Comparative morphometric parameters of the rat thymus in the control, E-171-exposed, and correction groups.

Parameters	Control group	E-171 group	E-171 + correction
Total lobule area (μm²)	212,638.7±19,542.1	150,983.1±15,575.7	177,519.7±16,905.9
Cortical area (μm²)	164,351.1±11,905.05	98,610.7±7,143.03	128,064.3±9,121.2
Medullary area (μm²)	48,287.6±3,961.2	52,372.4±4,112.1	49,455.4±4,002.2
Corticomedullary index (CMI)	3.40 ± 0.42	1.81 ± 0.23	2.60 ± 0.36

The combined histological and morphometric findings indicate that bitter almond oil administration was associated with partial attenuation of E-171-induced thymic injury. The most pronounced changes were observed in the cortical compartment, as reflected by the increased cortical area and corticomedullary index. However, the persistence of differences compared with the control group suggests that structural recovery remained incomplete.

Conclusion and recommendations

E-171 exposure caused structural alterations in the rat thymus. Bitter almond oil treatment increased the total lobule area by 17.6%, cortical area by 29.9%, and corticomedullary index from 1.9 to 2.60, indicating partial recovery, particularly in the thymic cortex. Based on these findings, the following recommendations are proposed:

1. Histological examination should be combined with morphometric assessment of the cortical and medullary compartments and the corticomedullary index to evaluate E-171-induced thymic injury.

2. Further investigations incorporating oxidative stress biomarkers and immunohistochemical markers are recommended to clarify the potential mechanisms underlying the corrective effects of bitter almond oil.

3. Additional controlled experimental studies should evaluate the chemical composition, safety, and dose-dependent effects of bitter almond oil.

References:

[1] EFSA Panel on Food Additives and Flavourings (FAF). (2021). Safety assessment of titanium dioxide (E171) as a food additive. EFSA Journal, 19(5), 6585. https://doi.org/10.2903/j.efsa.2021.6585

[2] Bettini, S., Boutet-Robinet, E., Cartier, C., et al. (2017). Food-grade TiO_2 impairs intestinal and systemic immune homeostasis, initiates preneoplastic lesions and promotes aberrant crypt development in the rat colon. Scientific Reports, 7, 40373. https://doi.org/10.1038/srep40373

[3] Hashem, M. M., et al. (2020). The long-term oral exposure to titanium dioxide impaired immune functions and triggered cytotoxic and genotoxic impacts in rats. Journal of Trace Elements in Medicine and Biology, 60, 126473. https://doi.org/10.1016/j.jtemb.2020.126473

[4] Blevins, L. K., Crawford, R. B., Bach, A., et al. (2019). Evaluation of immunologic and intestinal effects in rats administered an E171-containing diet, a food grade titanium dioxide (TiO_2). Food and Chemical Toxicology, 133, 110793. https://doi.org/10.1016/j.fct.2019.110793

[5] Pearse, G. (2006). Normal structure, function and histology of the thymus. Toxicologic Pathology, 34(5), 504–514. https://doi.org/10.1080/01926230600865549

[6] Pearse, G. (2006). Histopathology of the thymus. Toxicologic Pathology, 34(5), 515–547. https://doi.org/10.1080/01926230600978458

[7] Ouzir, M. et al. (2021). Almond oil: A comprehensive review of chemical composition, extraction methods, preservation conditions, potential health benefits, and safety. Comprehensive Reviews in Food Science and Food Safety, 20(4), 3344–3387. https://doi.org/10.1111/1541-4337.12752

[8] Guici El Kouacheur., et al. (2023). Prunus amygdalus var. amara (bitter almond) seed oil: Fatty acid composition, physicochemical parameters, enzyme inhibitory activity, antioxidant and anti-inflammatory potential. Journal of Food Measurement and Characterization, 17(1), 371–384. https://doi.org/10.1007/s11694-022-01629-2

[9] Bankhead, P., Loughrey, M. B., Fernández, J. A., et al. (2017). QuPath: Open source software for digital pathology image analysis. Scientific Reports, 7, 16878. https://doi.org/10.1038/s41598-017-17204-5

[10] Bischoff, N. S., de Kok, T. M., et al. (2021). Possible adverse effects of food additive E171 (titanium dioxide) related to particle specific human toxicity, including the immune system. International Journal of Molecular Sciences, 22(1), 207. https://doi.org/10.3390/ijms22010207

Section 6. ACTUAL PROBLEMS OF MATHEMATICS, PHYSICS AND MECHANICS

UDC: 621.3.082.782

DETERMINATION OF THE BAND GAP OF SEMICONDUCTORS IN A QUANTIZING MAGNETIC FIELD

Erkaboev Ulugbek
Professor, (DSc), Namangan State Technical University, Namangan, Uzbekistan
erkaboev1983@gmail.com
Khabibullaeva Laylokhon
Doctoral student, Namangan State University, Uzbekistan
habibullayevalayloo@gmail.com
Rakhimov Rustamjon
Associate Professor, (PhD), Namangan State Technical University, Uzbekistan
rgrakhimov@gmail.com

Annotatsiya. Ushbu ishda yarimo‘tkazgich ta’qiqlangan zonasining kengligi harorat hamda kvantlovchi magnit maydon birgalikda ta’sir etganda qanday o‘zgarishi o‘rganilgan. O‘tkazuvchanlik va valent zonalardagi holatlar zichligining haroratga qarab o‘zgarishini ifodalash uchun holatlar zichligi GN-funksiyalar qatori ko‘rinishida yozilgan; shu yo‘l bilan Landau sathlarining issiqlik ta’sirida kengayishi hisobga kiritilgan. InSb uchun bajarilgan sonli hisoblarga ko‘ra, H = 300 kE maydonda va T = 3 K haroratda ta’qiqlangan zona kengligi 0,263 eV ni tashkil etadi, bu esa maydonsiz va nol haroratdagi qiymatdan 0,029 eV ortiq. Harorat 3 K dan 300 K ga yetganda zona chegaralari yaqinidagi holatlar termik kengayadi va natijada ta’qiqlangan zona torayadi. n-InAs misolida esa effektiv massa energiyaga bog‘liq deb olinsa, kvantlovchi magnit maydondagi holatlar zichligining harorat bo‘yicha o‘zgarishi ancha boshqacha bo‘lishi ko‘rsatib berilgan.

Kalit so‘zlar: *ta’qiqlangan zona kengligi, kvantlovchi magnit maydon, Landau sathlari, holatlar zichligi, termik kengayish, GN-funksiya, effektiv massa, InSb, InAs.*

Аннотация. Изучено, как изменяется ширина запрещённой зоны полупроводника, когда на него одновременно действуют температура и квантующее магнитное поле. Чтобы описать поведение плотности состояний зоны проводимости и валентной зоны при изменении температуры, плотность

состояний представлена рядом по GN-функциям; тем самым в расчёт включено термическое уширение уровней Ландау. Для InSb численный расчёт при H = 300 кЭ и T = 3 K приводит к ширине запрещённой зоны 0,263 эВ — на 0,029 эВ выше, чем в отсутствие поля при нулевой температуре. Нагрев от 3 до 300 K сопровождается сужением запрещённой зоны, причина которого — термическое уширение состояний вблизи краёв зон. Расчёт для n-InAs показывает, что учёт энергетической зависимости эффективной массы заметно изменяет ход плотности состояний с температурой в квантующем магнитном поле.

Ключевые слова: *ширина запрещённой зоны, квантующее магнитное поле, уровни Ландау, плотность состояний, термическое уширение, GN-функция, эффективная масса, InSb, InAs.*

Abstract. We study how the band gap of a semiconductor responds when temperature and a quantizing magnetic field act on it together. To follow the temperature behaviour of the density of states in both the conduction and the valence band, the density of states is written as a series in GN-functions; in this way the thermal broadening of the Landau levels enters the calculation directly. A numerical model built for InSb yields a gap of 0.263 eV in a field of 300 kOe at 3 K, that is, 0.029 eV above the zero-field, zero-temperature value. Heating from 3 K to 300 K makes the gap shrink, since the states near the band edges spread out thermally. Taking n-InAs as an example, we also show that once the effective mass is allowed to depend on energy, the temperature dependence of the density of states in a quantizing magnetic field changes markedly.

Key words: *band gap, quantizing magnetic field, Landau levels, density of states, thermal broadening, GN-function, effective mass, InSb, InAs.*

Introduction

The band gap determines both the electrical and the optical properties of a semiconductor and, with them, the performance of the devices made from it. Considerable attention is now paid to materials that combine semiconducting and magnetic properties: they are expected to underlie a new generation of optoelectronic devices controlled by a magnetic field. Designing such devices requires an understanding of how the band gap behaves when a strong magnetic field and temperature act on the crystal simultaneously.

A quantizing magnetic field quantizes the motion of charge carriers in the plane perpendicular to the field. As a result, the continuous energy spectrum in both the conduction band and the valence band is replaced by a set of Landau levels, the density of states begins to oscillate as a function of energy, and the edges of the allowed bands shift. Heating causes thermal broadening of the Landau levels; when kT becomes comparable to $\hbar\omega_c$, the discrete structure of the spectrum is smoothed out [1, 2]. Both mechanisms, Landau quantization and thermal broadening, affect the positions of the band edges at the same time, yet their joint effect on the band gap has so far been studied poorly.

The aim of this work is to find, on the basis of a model of thermal broadening of energy levels, the band gap of a semiconductor placed in a quantizing magnetic field at different temperatures. To achieve this, three tasks had to be solved:

1) to derive an expression for the density of states of the conduction and valence bands in a quantizing magnetic field that takes its temperature dependence into account;
2) to calculate the density of states of InSb for several temperatures and magnetic field strengths and to determine the positions of the band edges from it;
3) to find out, using n-InAs as an example, how the temperature dependence of the density of states changes when the effective mass depends on energy.

Literature Review

It has been established from electrical and optical measurements that the band gap of semiconductors changes with temperature [3]. The reason is seen in the change of the

energy of the electron–phonon system, which consists of three parts: a purely electronic one, a vibrational one, and one associated with the electron–phonon interaction [4].

Band parameters are determined most reliably by optical methods. As shown in [5–9], the band gap, as well as the effective masses and mobilities of electrons and holes, can be extracted from optical properties with sufficient reliability. These works investigated quantum wells based on $Cd_xHg_{1-x}Te$ [5], InGaN quantum dots [6] and CdS_xSe_{1-x} quantum dots [8], and AlGaN alloys [7], while in [9] sets of parameters for describing the temperature dependence of the fundamental gap were collected. In all of these cases the band gap was found from optical spectra, and its temperature dependence was obtained without a magnetic field.

A sufficiently strong magnetic field substantially reconstructs the energy spectrum of free electrons and holes, and this affects the density of states [10]. Interband magneto-optical measurements in static and pulsed fields have shown that the band gap of InAs depends nonlinearly on the magnetic field [11]. For GaAs, the optical band gap in fields of up to 10 MG was calculated in a five-band $k \cdot p$ model, and agreement with experiment can be reached if the contribution of the “tails” of the density of states to light absorption is taken into account [12]. However, the question of how temperature affects the band gap in a quantizing magnetic field was not addressed in [10–12].

Another way of describing the temperature dependence of energy gaps was proposed in [13–15]. In it, the density of states is expanded in a series in *GN*-functions, that is, in derivatives of the probability of depopulating an energy level with respect to energy. According to this model, the band gap changes with temperature because of the thermal broadening of the quasi-discrete levels located at the bottom of the conduction band and at the top of the valence band. In this way the temperature dependence of the band gap of Ge [14] and Si [15] was explained.

Later this method was extended to the density of states in a quantizing magnetic field [1, 2]. It turned out that the density-of-states spectrum, which looks continuous at liquid-nitrogen temperature, breaks up into discrete Landau levels on cooling. Nevertheless, none

of the cited works determined the band gap in a quantizing magnetic field at different temperatures; this is the problem solved in the present paper.

Research Methodology

Theoretical calculation and computer simulation were used in this work; all numerical calculations were performed in the Maple package. The band gap is defined as the distance between the conduction band edge and the valence band edge, both found from the calculated density of states.

If the spin splitting of the levels is taken into account, the energies of free electrons and holes in a quantizing magnetic field are written as [10]:

$$E_c(N,k_z) = E_g(0) + \left(N+\tfrac{1}{2}\right)\hbar\omega_e + \frac{\hbar^2 k_z^2}{2m_e} \pm \tfrac{1}{2} g_e \mu_B H$$
$$E_v(N,k_z) = -\left(N+\tfrac{1}{2}\right)\hbar\omega_h - \frac{\hbar^2 k_z^2}{2m_h} \pm \tfrac{1}{2} g_h \mu_B H \qquad (1)$$

In (1), $N = 0, 1, 2, \ldots$ numbers the Landau levels, k_z is the component of the wave vector along the field, m_e and m_h are the effective masses of the electron and the hole, ω_e and ω_h are the corresponding cyclotron frequencies, g_e and g_h are the g-factors, μ_B is the Bohr magneton, H is the magnetic field strength, and $E_g(0)$ is the band gap at $T = 0$ and $H = 0$. The energy zero is taken at the valence band top in the absence of the field.

To pass from absolute zero to a finite temperature, the density of states is represented as a series in GN-functions [2, 13]:

$$N_s(E,H,T) = \sum_{i=1}^{n} N_s(E_i,H)\,GN(E_i,E,T)\,\Delta E \qquad (2)$$

$$GN(E_i,E,T) = \frac{1}{kT}\exp\left[\frac{E_i - E}{kT} - \exp\left(\frac{E_i - E}{kT}\right)\right] \qquad (3)$$

In these expressions ΔE is the step into which the energy scale is divided, k is the Boltzmann constant, and $N_s(E_i, H)$ is the density of states that the semiconductor would have in a quantizing magnetic field at $T = 0$. The meaning of the expansion is simple: on heating, the

level E_i ceases to be sharp, and the shape of its smearing is given by the *GN*-function. Summing in (2) such smeared contributions from all levels of the chosen energy interval, we obtain the density of states at temperature T. In the limit $T \to 0$ the *GN*-function turns into the Dirac delta function.

If the spin splitting is neglected, the density of states of the conduction band at $T = 0$ has the form [16]:

$$N_s^c(E,H) = \frac{(2m_e)^{3/2}\hbar\omega_e}{4\pi^2\hbar^3}\sum_{N=0}^{N_{\max}}\left[E - E_g(0) - \left(N+\tfrac{1}{2}\right)\hbar\omega_e\right]^{-1/2} \tag{4}$$

and for the valence band:

$$N_s^v(E,H) = \frac{(2m_h)^{3/2}\hbar\omega_h}{4\pi^2\hbar^3}\sum_{N=0}^{N_{\max}}\left[-E - \left(N+\tfrac{1}{2}\right)\hbar\omega_h\right]^{-1/2} \tag{5}$$

Only those N for which the expression under the root is positive enter the sums (4) and (5). The distribution of states over energy is given by:

$$N_s(E,H) = \begin{cases} N_s^v(E,H), & E < E_v, \\ 0, & E_v < E < E_c, \\ N_s^c(E,H), & E > E_c. \end{cases} \tag{6}$$

The boundaries in (6) are the band edges already shifted by the magnetic field: at $T = 0$ the valence band ends at the energy $E_v = -\hbar\omega_h/2$, and the conduction band begins at $E_c = E_g(0) + \hbar\omega_e/2$.

If distribution (6) is now substituted as $N_s(E_i, H)$ into the sum (2), we obtain the density of states $N_s(E, H, T)$ corresponding to the chosen values of H and T. The sought quantity, the interval between the edges of the two bands, is found from it:

$$E_g(H,T) = E_c(H,T) - E_v(H,T) = E_g(0) + \Delta\varepsilon(H,T) \tag{7}$$

Here $E_c(H, T)$ and $E_v(H, T)$ denote the energies between which the calculated curve contains no states, and $\Delta\varepsilon(H, T)$ is the addition to $E_g(0)$ caused by the field and temperature. When $T \to 0$, the band edges are the zero Landau levels ($N = 0$), and expression (7) simplifies to:

$$E_g(H) = E_g(0) + \tfrac{1}{2}\hbar\left(\omega_e + \omega_h\right) \tag{8}$$

The calculation proceeds as follows:

1) the energy interval that includes both allowed bands and the forbidden gap between them is divided into small equal segments;
2) at each node of the partition the density of states at $T = 0$ is found from formulas (4)–(6);
3) summation according to formula (2) gives $N_s(E,H,T)$ for the required temperature;
4) E_c and E_v are determined from the resulting curve, after which $E_g(H,T)$ is calculated from formula (7).

The correctness of the model is verified by limiting cases. For $T \to 0$, expression (2) turns into (6), and the Landau levels are seen as sharp peaks. For kT > $\hbar\omega_c$ the oscillations disappear, and the density of states becomes the same as without a magnetic field [1, 2].

Results and Discussion

The calculations were carried out for InSb; the value $E_g(0) = 0.234$ eV was taken from [9]. The field was chosen equal to 300 kOe, and the temperature took the values of 3, 70 and 300 K; the resulting density-of-states curves for both bands of InSb are collected in Fig. 1. On the left, at $E < E_v$, lies the valence band; on the right, at $E > E_c$, the conduction band; and the interval $E_v < E < E_c$ between them is empty: this is the band gap. The lowest of the three temperatures, 3 K, gives a curve that hardly differs from the ideal one described by formulas (4)–(6): the levels are still too little broadened by heat. The positions of the band edges and the band gap were determined from this curve (Table 1).

Table 1. Band edge positions and band gap of InSb at $H = 300$ kOe and $T = 3$ K

Quantity	Value, eV
$E_g(0)$, band gap at $T = 0$ and $H = 0$	0.234
E_v, valence band top	−0.012
E_c, conduction band bottom	0.251
$E_g = E_c - E_v$, band gap	0.263
$\Delta\varepsilon = E_g - E_g(0)$, change of the band gap	0.029

$E_g(0)$ is taken from [9].

Thus, at T = 3 K in a field H = 300 kOe the band gap of InSb is wider than at zero field and zero temperature by 0.029 eV. This increase is explained by the shift of the band edges toward the zero Landau levels (N = 0), as follows from formula (8). A different picture is observed on heating. The curves of Fig. 1 show that between 3 and 300 K the band gap of InSb becomes narrower. The reason is the thermal smearing of the levels of both bands, the conduction band and the valence band: the sharp edges of the density of states are blurred and extend into the forbidden gap.

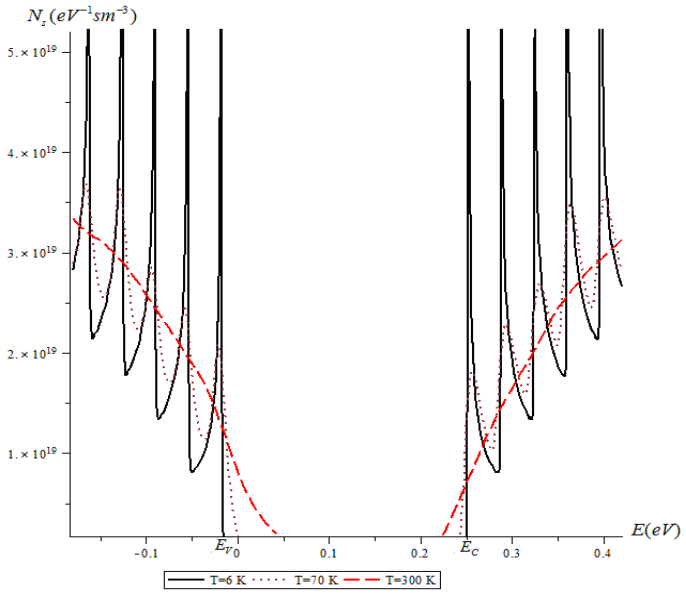


Fig. 1. Density of states of InSb at H = 300 kOe, calculated for temperatures of 3, 70 and 300 K (by formulas (2)–(6)).

Fig. 2 allows the densities of states of InSb at T = 3 K to be compared in two fields: H = 300 kOe and H = 400 kOe (B = 30 and 40 T). In the stronger field the Landau levels are farther apart, the band edges shift, and the band gap, according to formula (8), increases.

So far the masses m_e and m_h in (4) and (5) have been constants. In reality the mass of a carrier depends on its energy, and for electrons in n-InAs this dependence has been measured: in [17] it was obtained by analysing how the amplitude of the oscillations of tunnelling conductance in a strong magnetic field changes with temperature. The result of [17] is reproduced in Fig. 3. This dependence can be included directly in the calculation. The higher the electron energy, the larger its mass and the lower its cyclotron frequency

(which is inversely proportional to the mass), so that with increasing energy neighbouring Landau levels move closer together. The density of energy states of InAs calculated in this way for H = 50 kOe at several temperatures is shown in Fig. 4. A comparison of the curves in Fig. 4 shows that, for a variable effective mass, the density of states in a quantizing magnetic field changes with temperature noticeably differently. Since the band gap is found precisely from the edges of the density of states, the energy dependence of the mass cannot be ignored in the calculation of $E_g(H, T)$ either.

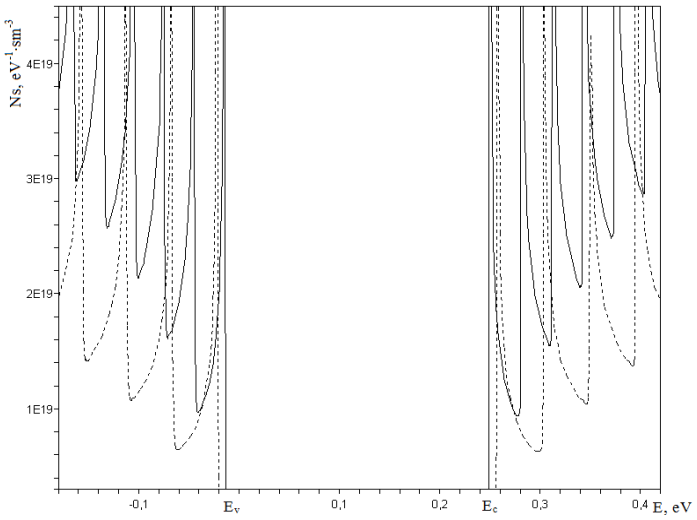


Fig. 2. Density of energy states of InSb at T = 3 K for two values of the magnetic field: H = 300 kOe (solid line) and H = 400 kOe (dashed line).

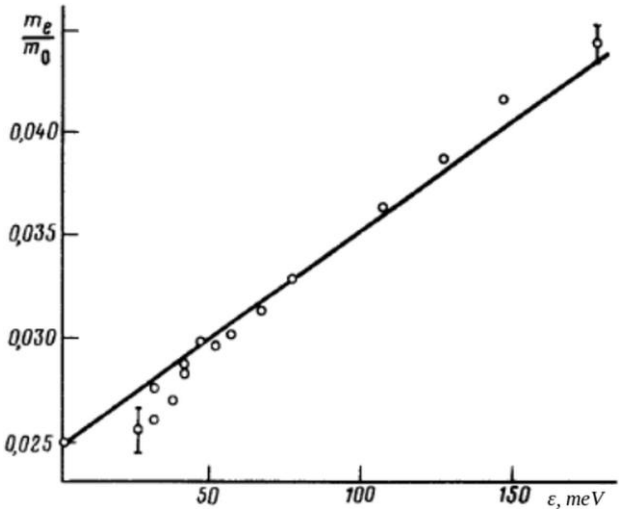


Fig. 3. Effective mass of electrons in n-InAs as a function of energy [17].

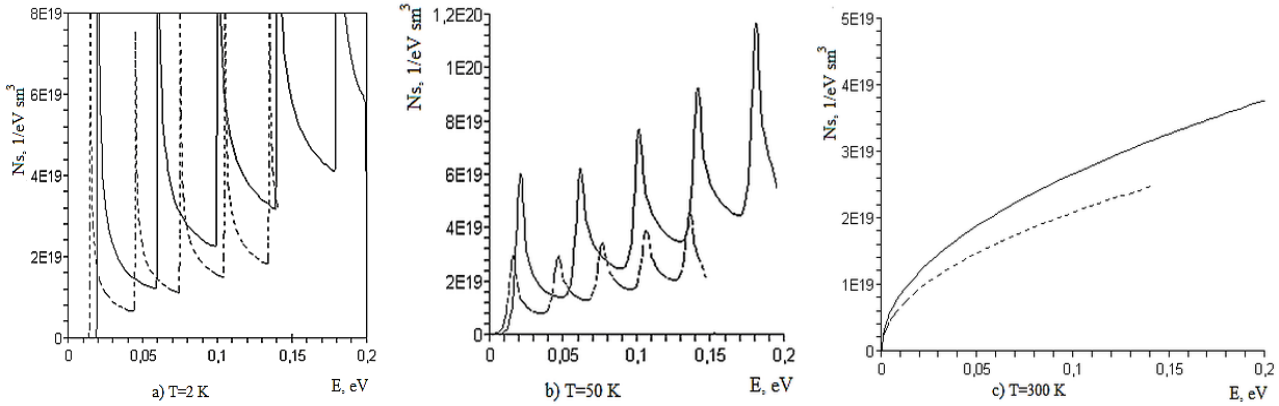


Fig. 4. Density of energy states of InAs at H = 50 kOe and temperatures of 2, 50 and 300 K (a, b, c); the effective mass in the calculation depends on energy.

Conclusion and Recommendations

The study carried out allows the following conclusions to be drawn:

- It is proposed to find the band gap of a semiconductor in a quantizing magnetic field directly from the density of states of the two bands, the conduction band and the valence band. Thermal broadening of the Landau levels is introduced here through the expansion of the density of states in a series in *GN*-functions.
- For InSb in a field of 300 kOe at 3 K the calculation gives E_c = 0.251 eV and E_v = −0.012 eV, i.e. E_g = 0.263 eV, which is 0.029 eV larger than $E_g(0)$ = 0.234 eV.
- Heating InSb from 3 to 300 K in the same field narrows the band gap. It follows that the thermal smearing of states near the edges of both bands can substantially change the band gap in a quantizing magnetic field.
- If the effective mass of electrons depends on energy, as in InAs, the density of states behaves with temperature in a substantially different way; together with it, the temperature course of the band gap in a quantizing magnetic field changes as well.

On the basis of the results obtained, the following recommendations are made:

1) When processing experimental density-of-states and magneto-optical spectra recorded in strong magnetic fields, the band gap should be determined from the band edges of the density-of-states curve calculated with account of thermal broadening;

the value E_g = 0.263 eV for InSb at 300 kOe and 3 K can serve as a reference for comparison with measurements.

2) In calculations of $E_g(H, T)$ for narrow-gap semiconductors such as InAs, the energy dependence of the effective mass should be taken into account, because a constant mass distorts the temperature behaviour of the density of states.
3) In the design of magnetodiodes and magnetically controlled optoelectronic devices, the operating temperature should be chosen taking into account that the magnetic field widens the band gap, whereas thermal broadening of the states narrows it.
4) Further research should extend the calculation to semiconductors with a nonparabolic (Kane) dispersion law and take into account the influence of hydrostatic pressure on the positions of the band edges.

References

[1] Gulyamov G., Erkaboev U.I., Sharibaev N.Yu. Effect of temperature on the thermodynamic density of states in a quantizing magnetic field // Semiconductors. 2014. Vol. 48, Iss. 10, pp. 1323–1328.
[2] Gulyamov G., Erkaboev U.I., Sharibaev N.Yu. Simulation of the temperature dependence of the density of states in a strong magnetic field // Journal of Modern Physics. 2014. Vol. 5, No. 8, pp. 680–685.
[3] Vavilov V.S., Kekelidze N.P., Smirnov L.S. Effect of Radiation on Semiconductors. Moscow: Nauka, 1988, pp. 50–75 (in Russian).
[4] Ridley B.K. Quantum Processes in Semiconductors. Moscow: Mir, 1986, pp. 85–100 (Russian translation).
[5] Bazhenov N.L., Shilyaev A.V., Mynbaev K.D., Zegrya G.G. Optical transitions in quantum wells based on $Cd_xHg_{1-x}Te$ and their analysis taking into account the features of the band structure // Fizika i Tekhnika Poluprovodnikov. 2012. Vol. 46, Iss. 6, pp. 792–798 (in Russian).
[6] Usov S.O., Tsatsulnikov A.F., Lundin V.V., Sakharov A.V., Zavarin E.E., Ledentsov N.N. Photoluminescence of localized excitons in InGaN quantum dots // Fizika i Tekhnika Poluprovodnikov. 2008. Vol. 42, Iss. 2, pp. 187–191 (in Russian).
[7] Nepal N., Li J., Nakarmi M.L., Lin J.Y., Jiang H.X. Temperature and compositional dependence of the energy band gap of AlGaN alloys // Applied Physics Letters. 2005. Vol. 87, 242104.
[8] Kunets V.P., Kulish N.R., Kunets Vas.P., Lisitsa M.P., Malysh N.I. Temperature dependence of the optical energy gap of CdS_xSe_{1-x} quantum dots // Fizika i Tekhnika Poluprovodnikov. 2002. Vol. 36, Iss. 2, pp. 227–230 (in Russian).
[9] Pässler R. Parameter sets due to fittings of the temperature dependencies of fundamental bandgaps in semiconductors // Physica Status Solidi (b). 1999. Vol. 216, pp. 975–990.

[10] Anselm A.I. Introduction to Semiconductor Theory. Moscow: Nauka, 1978, Ch. 6, p. 367 (in Russian).
[11] Zwerdling S., Keyes R.J., Foner S., Kolm H.H., Lax B. Magneto-band effects in InAs and InSb in dc and high pulsed magnetic fields // Physical Review. 1956. Vol. 104, Iss. 6, pp. 1805–1808.
[12] Aleshkin V.Ya., Zakrevskii N.V. Optical band gap of GaAs in megagauss magnetic fields // Fizika Tverdogo Tela. 2007. Vol. 49, Iss. 4, pp. 602–612 (in Russian).
[13] Gulyamov G., Sharibaev N.Yu. Determination of the density of surface states at the semiconductor–insulator interface in an MIS structure // Fizika i Tekhnika Poluprovodnikov. 2011. Vol. 45, Iss. 2, pp. 178–182 (in Russian).
[14] Gulyamov G., Sharibaev N.Yu., Erkaboev U.I. Thermal broadening of the density of states and temperature dependence of the band gap of Ge // Physical Surface Engineering. 2012. Vol. 10, No. 4, pp. 366–370 (in Russian).
[15] Gulyamov G., Erkaboev U.I., Sharibaev N.Yu. The temperature dependence of the band gap Si // Physical Surface Engineering. 2013. Vol. 11, No. 3, pp. 289–292.
[16] Ziman J.M. Principles of the Theory of Solids. Moscow: Mir, 1974, Ch. 9, p. 349 (Russian translation).
[17] Zverev L.P., Kruzhaev V.V., Min'kov G.M., Rut O.E. On the possibility of using tunnelling spectroscopy to determine the energy dependence of the effective mass in semiconductors // JETP Letters. 1980. Vol. 31, Iss. 3, pp. 169–172 (in Russian).

UDC: 621.382.2

EFFECT OF HEIGHT ON THE EFFICIENCY OF A SILICON VERTICAL TUNNEL-JUNCTION CONCENTRATOR SOLAR CELL: TCAD MODELLING WITH A CALIBRATED TUNNEL JUNCTION MODEL

Bexzod Jumaboyev Quronboy o‘g‘li
PhD student, Department of Physics, Urgench State University named after Abu Rayhon Beruniy
jumaboyevbexzod2315@gmail.com

Otaxonova Nafisa Omonboy qizi
Master's student, Department of Physics, Urgench State University named after Abu Rayhon Beruniy
nafisaotaxonova81@gmail.com

Davlatova Maqsuda Muxiddin qizi
Teacher, General Secondary Education School No. 6, Urgench District, Uzbekistan
davlatovamaqsuda2315@gmail.com

Xushnudbek Saparov Sharipbayevich
Lecturer, Department of Physics, Urgench State University named after Abu Rayhon Beruniy
xushnudbeksaparov@gmail.com

Ortikova Dilnura Umid qizi
Master's student, Department of Physics, Urgench State University named after Abu Rayhon Beruniy
ortiqovadilnura212@gmail.com

Annotatsiya. Ushbu ishda ikkita p^+nn^+ element metall kontakt o‘rniga kremniy tunnel o‘tish orqali ulangan vertikal konsentratorli quyosh elementi (VTJ) Sentaurus

TCAD dasturida 2D modellashtirish yordamida o‘rganildi. Si tunnel diodining modellari tajriba asosida kalibrlandi: dinamik nolokal zonadan-zonaga tunnellanish, Hurkx modeli va chegaraviy tuzoqlar birgalikda qo‘llanganda cho‘qqi toki va manfiy differensial qarshilik sohasi to‘g‘ri tavsiflandi. Kalibrlangan VTJ elementi metall kontaktli element bilan deyarli bir xil J–V xarakteristikaga ega. Element balandligi H 5 μm dan 600 μm gacha oshganda (W_n = 20 μm) samaradorlik 8,36 % dan 13,16 % gacha ortadi, bu asosan qisqa tutashuv tokining ortishi bilan bog‘liq.

Kalit so‘zlar: *vertikal quyosh elementi, tunnel o‘tish, kremniy, konsentratorli fotoenergetika, TCAD modellashtirish, samaradorlik.*

Аннотация. Методом 2D-моделирования в Sentaurus TCAD исследован вертикальный концентраторный солнечный элемент, в котором два p^+nn^+-субэлемента соединены кремниевым туннельным переходом (VTJ) вместо металлического контакта. Модели кремниевого туннельного диода откалиброваны по эксперименту: совместное использование модели межзонного туннелирования по динамическому нелокальному пути, модели Hurkx и ловушек на границе воспроизводит пиковый ток и область отрицательного дифференциального сопротивления. Откалиброванный VTJ-элемент имеет практически ту же ВАХ, что и элемент с металлическим контактом. При увеличении высоты элемента H от 5 до 600 мкм (W_n = 20 мкм) КПД возрастает с 8,36 % до 13,16 %, главным образом за счёт роста тока короткого замыкания.

Ключевые слова: *вертикальный солнечный элемент, туннельный переход, кремний, концентраторная фотоэнергетика, TCAD-моделирование, КПД.*

Abstract. A silicon vertical concentrator solar cell with two p^+nn^+ subcells connected by a Si tunnel junction (VTJ) instead of a metal contact is studied by 2D simulation in Sentaurus TCAD. The models of a Si tunnel diode were calibrated against experiment: the dynamic nonlocal path band-to-band tunnelling model

combined with the Hurkx model and interface traps reproduces the peak current and the negative differential resistance region. The calibrated VTJ cell has practically the same J–V characteristic as the metal-contact cell. When the cell height H increases from 5 to 600 μm (W_n = 20 μm), the efficiency rises from 8.36 % to 13.16 %, mainly due to the growth of the short-circuit current.

Key words: *vertical solar cell, tunnel junction, silicon, concentrator photovoltaics, TCAD simulation, efficiency.*

Introduction

Concentrator photovoltaics (CPV) provides the highest conversion efficiencies among photovoltaic technologies [1] and reduces the amount of expensive semiconductor material by collecting sunlight with inexpensive optics [2]. However, at high concentrations the efficiency of conventional horizontal-junction cells saturates and then decreases because of series resistance losses [3, 4]. Vertical junction cells solve this problem [4, 5]: the p–n junctions are perpendicular to the illuminated surface, the contacts are on the lateral faces and do not shade the cell, and the series connection of subcells gives a high voltage at a low current density. Silicon vertical multijunction (VMJ) cells with metal interconnections showed high performance at about 1000 suns [6]. Fernández et al. proposed the vertical-tunnel-junction (VTJ) cell, in which the subcells are connected by tunnel junctions, and showed for GaAs that it keeps a high efficiency above 2000 suns [7, 8]. Silicon tunnel diodes can be fabricated by spin-on doping and rapid thermal processing [9], and Si tunnel junctions have been simulated for silicon/perovskite tandems [10]. However, the simulation of Si VTJ cells requires a tunnel junction model validated against experiment, and the effect of the cell height on their efficiency is not sufficiently clear. The aim of this work is to calibrate the tunnelling models of a Si tunnel junction in Sentaurus TCAD and to use them to study the effect of the cell height H and base width W_n on the efficiency of a Si VTJ cell with two p^+nn^+ subcells.

Literature review

Gover and Stella developed a one-dimensional analytical theory of VMJ cells relating the short-circuit current and open-circuit voltage to the cell dimensions [11]. Sater and Sater measured silicon VMJ cells of 40 series-connected p^+nn^+ units under high concentration [6]. Pozner et al. showed that the low series resistance of vertical Si cells allows operation at much higher concentrations than horizontal cells [4]; Xing et al. reviewed concentrator Si cells [5] and analysed front surface diffusion in VMJ cells [12]; Braun et al. proposed multiple-bandgap vertical-junction architectures [13]. For GaAs VTJ cells, efficiencies of about 28 % up to 10,000 suns were predicted [7, 8]. A tunnel junction can limit the cell when its peak current is lower than the photocurrent [14], and nonlocal tunnelling models are needed to describe it [15]. Band-to-band tunnelling is described by the Kane model [16], and trap-assisted tunnelling by the Hurkx [17] and Schenk [18] models. Experimental J–V curves of Si tunnel diodes were reported by Yan [19]. Our previous works [20, 21] studied the effects of geometry and doping on a Si VTJ cell without an experimentally calibrated tunnel junction model, which motivates the present study.

Research methodology

The 2D simulations were carried out in Synopsys Sentaurus TCAD [22] in two stages. First, an isolated Si tunnel diode (Fig. 1a, Table 1) with the dimensions and doping of the experimental sample [19] was simulated and compared with the measured J–V curve. Then the tunnel junction was incorporated into a vertical cell of two identical p^+nn^+ subcells (Fig. 1b, Table 2)

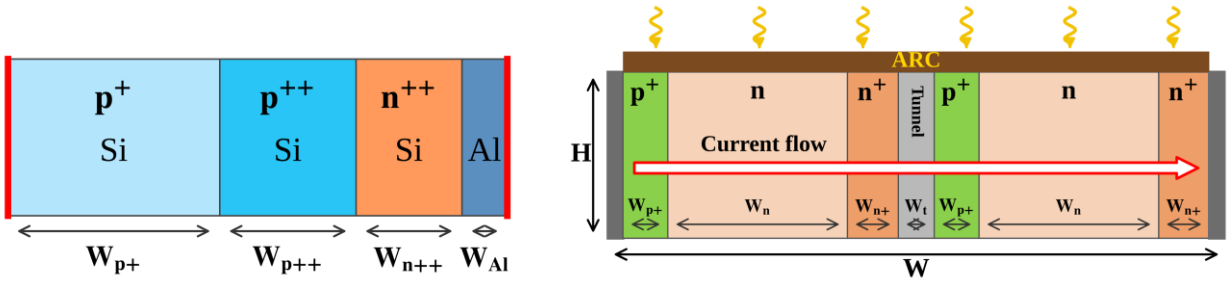


Fig. 1. Simulated structures: (a) Si tunnel diode; (b) vertical two-junction Si solar cell with a tunnel junction (VTJ).

Table 1. Parameters of the simulated Si tunnel diode.

H, μm	W_{p+}, μm	W_{p++}, μm	W_{n++}, μm	W_{Al}, μm	p^+, cm^{-3}	p^{++}, cm^{-3}	n^{++}, cm^{-3}
64	0.05	0.02	0.014	0.01	10^{18}	$3.6\cdot10^{20}$	$8\cdot10^{20}$

Table 2. Parameters of the simulated vertical two-junction VMJ and VTJ cells.

H, μm	W_{p+}, μm	W_{n+}, μm	W_n, μm	W_{p++}, μm	W_{n++}, μm	W_{metal}, μm	H_{ARC}, μm	p^+, cm^{-3}	n, cm^{-3}	n^+, cm^{-3}	p^{++}, cm^{-3}	n^{++}, cm^{-3}
500	5	5	185	0.02	0.014	55	0.1	$8\cdot10^{17}$	10^{14}	$3\cdot10^{18}$	$2\cdot10^{20}$	$1.1\cdot10^{20}$

with lateral metal contacts and a top antireflection coating (ARC). Light is incident on the top surface parallel to the junctions, and the current flows laterally. The drift–diffusion model, doping-dependent mobility, SRH recombination ($\tau_n = 10^{-5}$ s, $\tau_p = 3\cdot10^{-6}$ s), Auger recombination and ray-tracing optics were used. For the tunnel junction two model sets were compared: (1) nonlocal barrier tunnelling (e/hBarrierTunneling "NLM") with Schenk trap-assisted tunnelling; (2) dynamic nonlocal path band-to-band (BTB) recombination with SRH recombination including the Hurkx and doping-dependent models and traps at the p^{++}/n^{++} interface. The BTB rate follows the Kane–Keldysh expression [16]:

$$R_{net} = A\cdot(F/F_0)^P\cdot\exp(-B/F), \quad (1)$$

where F is the electric field, $F_0 = 1$ V/cm, P = 2, and A and B are fitting coefficients. The doping of the degenerate layers, the trap density, A and B were adjusted to fit the experiment. The cell model was validated against the J–V curve of the Si VMJ cell with 40 junctions [6], converted to two junctions by dividing the voltage by 20. The experiment at 2480 suns and 850 W/m² corresponds to 2108 suns at 1000 W/m² in the simulation; in the VMJ cell the subcells were connected by a 55 μm metal contact. The efficiency was calculated as

$$\eta = I_{sc}\cdot U_{oc}\cdot FF / (P_{in}\cdot W) = J_{sc}\cdot H\cdot U_{oc}\cdot FF / (P_{in}\cdot W), \quad (2)$$

where I_{sc} is the short-circuit current per unit depth, J_{sc} its density referred to the junction area, U_{oc} the open-circuit voltage, FF the fill factor, P_{in} the incident power density and W the cell width. H and W_n were varied in the range 5–600 μm at a solar concentration of one suns.

Analysis and results

Calibration of the tunnel junction model. The nonlocal barrier tunnelling model (Fig. 2a) describes the rise of the tunnel current up to the peak (≈ $2.6 \cdot 10^5$ mA/cm² at 0.15 V), but after the peak the current drops almost to zero, so the valley current is not reproduced and the diffusion branch is shifted. The dynamic nonlocal path BTB model with the Hurkx model and interface traps (Fig. 2b) reproduces the whole characteristic: the peak (≈ $2.7 \cdot 10^5$ mA/cm² at 0.16 V), the negative differential resistance region, the valley (≈ $1.25 \cdot 10^5$ mA/cm² at 0.33–0.35 V, peak-to-valley ratio ≈ 2.2) and the diffusion branch, for p^{++} = $3.6 \cdot 10^{20}$ cm^{-3} and n^{++} = $8 \cdot 10^{20}$ cm^{-3}. Hence the valley current is governed by trap-assisted tunnelling at the interface. The peak current density (≈ 270 A/cm²) is an order of magnitude higher than the short-circuit current density of the cell at 2108 suns (≈ 27 A/cm², Fig. 3a), so such a tunnel junction does not limit the cell current. *Validation of the cell model.* The simulated J–V curves of the VMJ (metal interconnection) and VTJ (tunnel interconnection) cells agree well with the experiment [6] (J_{sc} ≈ 27 A/cm², U_{oc} ≈ 1.6 V), and the VTJ curve practically coincides with the VMJ curve (Fig. 3a). In Fig. 3b a single vertical junction (VJ) and the two-junction VTJ cell have the same J_{sc} = 84.24 mA/cm², while U_{oc} doubles from 0.5653 V to 1.131 V (FF = 73.81 %, η = 11.54 %).

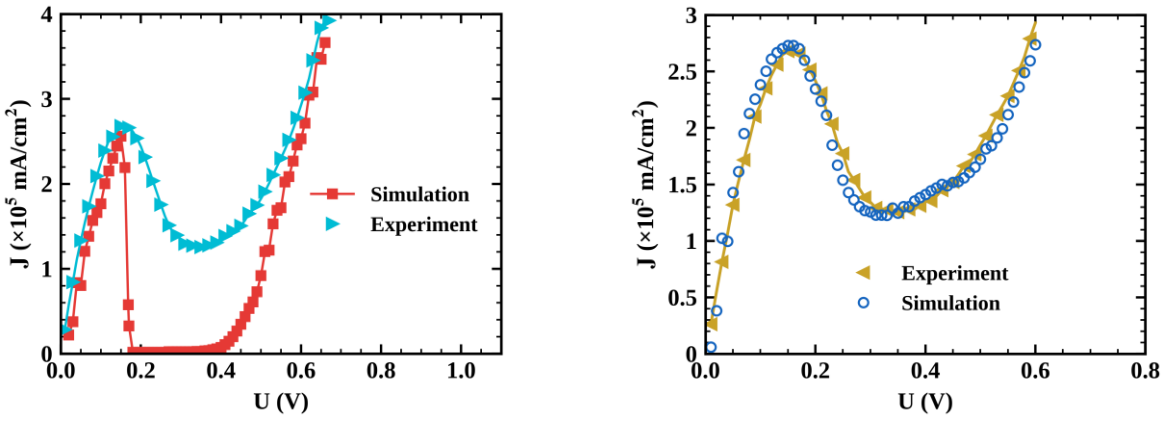
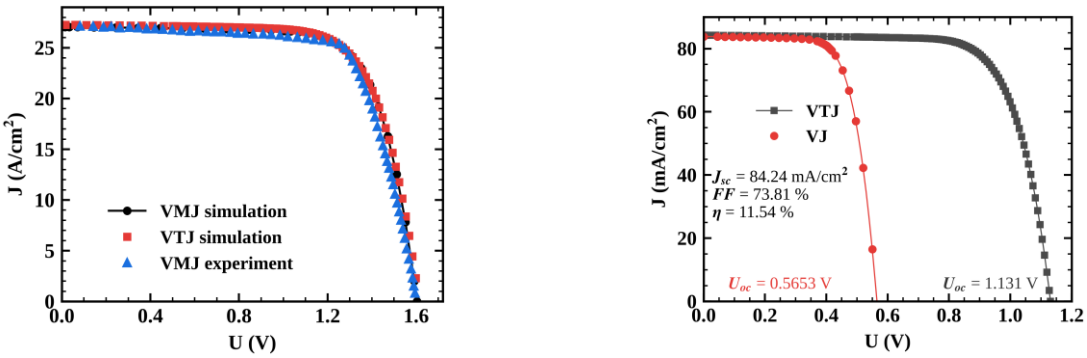


Fig. 2. Experimental [19] and simulated J–V curves of the Si tunnel diode: (a) nonlocal barrier tunnelling with Schenk trap-assisted tunnelling; (b) dynamic nonlocal path BTB model with Hurkx model and interface traps.

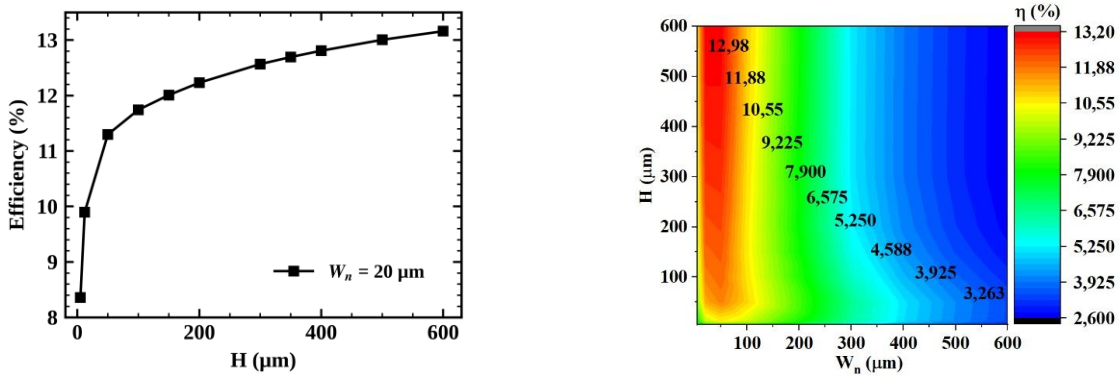
Thus the voltage drop across the tunnel junction is negligible, and it can replace the metal interconnection.



(a) (b)

Fig. 3. (a) Experimental [6] and simulated J–V curves of two-junction VMJ and VTJ cells at 2108 suns (Table 2); (b) J–V curves of a single vertical junction (VJ) and the VTJ cell (H = 64 μm, tunnel layers as in Table 1).

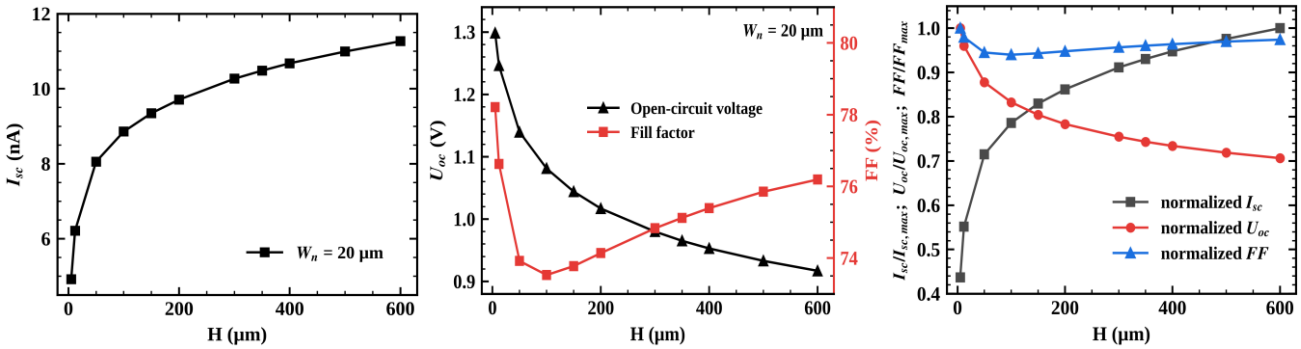
Effect of height and base width. According to the efficiency map (Fig. 4b), η increases with H for all W_n. At a fixed H, η reaches a maximum at $W_n \approx 20$–50 μm and then falls to about 5 % at $W_n \approx 300$ μm. The incident power grows with the cell width, but the carriers are collected only within the diffusion length: for $\tau_p = 3 \cdot 10^{-6}$ s in the lightly doped n-base, the hole diffusion length is about 60 μm. Carriers generated farther away recombine, and the base series resistance increases, so the optimum W_n lies below the diffusion length. At W_n = 20 μm (Fig. 4a) the efficiency rises steeply from 8.36 % at H = 5 μm to about 11.3 % at 50 μm and then slowly approaches saturation (≈ 12.6 % at 300 μm, 13.16 % at 600 μm). I_{sc} increases with H from 4.9 to 11.3 nA, i.e., 2.3 times (Fig. 5a).



(a) (b)

Fig. 4. (a) Efficiency versus cell height H at W_n = 20 μm; (b) efficiency map versus H and base width W_n.

Since light propagates along the height, H is the optical thickness of the cell: near-infrared photons have absorption lengths of tens to hundreds of micrometres in Si, so I_{sc} grows until almost all absorbable light is collected. U_{oc} decreases from 1.30 to 0.92 V (Fig. 5b). For each junction $U_{oc} = (kT/q)\cdot\ln(I_{sc}/I_0 + 1)$ [11], and the dark current I_0 is proportional to the junction area, i.e., to H; as I_{sc} grows more slowly than H, U_{oc} falls. FF decreases from 78.2 % to 73.5 % at H ≈ 100 μm and then rises to 76.2 % (Fig. 5b),



(a) (b) (c)

Fig. 5. (a) I_{sc}, (b) U_{oc} and FF, (c) normalized I_{sc}, U_{oc} and FF versus cell height H (W_n = 20 μm).

which is attributed to the changes of the series and shunt resistances with geometry [12]; at large H the base series resistance, proportional to W_n/H, decreases. The normalized curves (Fig. 5c) show that I_{sc} changes by 56 %, U_{oc} by 29 % and FF by less than 6 %. Therefore, η(H) is determined mainly by I_{sc}, while the decrease of U_{oc} limits the efficiency growth at large H.

Conclusion and recommendations

A Si vertical two-junction concentrator cell with a tunnel junction interconnection was studied using a tunnel junction model calibrated against experiment. The VTJ cell reproduces the experimental J–V curve of the Si VMJ cell, its U_{oc} equals the sum of the subcell voltages, and its efficiency increases from 8.36 % to 13.16 % as H increases from 5 to 600 μm. Based on the results, we recommend:

1) to simulate Si tunnel junctions in Sentaurus TCAD with the dynamic nonlocal path BTB model combined with SRH recombination including Hurkx tunnelling and interface

traps ($p^{++} = 3.6 \cdot 10^{20}$ cm^{-3}, $n^{++} = 8 \cdot 10^{20}$ cm^{-3}), since the nonlocal barrier tunnelling model alone does not reproduce the negative differential resistance and the valley current;

2) to use Si tunnel junctions instead of metal interconnections in silicon vertical multijunction concentrator cells, as they give the same J–V characteristic without noticeable voltage loss and simplify fabrication;

3) to choose the cell height $H \geq 300$ µm, where the efficiency is within 5 % of its value at 600 µm, and the base width $W_n \approx 20$–50 µm, below the minority-carrier diffusion length, avoiding $W_n > 100$ µm.

References:

[1] P. Pérez-Higueras, J.P. Ferrer-Rodríguez, F. Almonacid, E.F. Fernández, "Efficiency and acceptance angle of high concentrator photovoltaic modules: current status and indoor measurements," *Renewable and Sustainable Energy Reviews*, vol. 94, pp. 143–153, 2018.

[2] A. Luque, S. Hegedus (Eds.), *Handbook of Photovoltaic Science and Engineering*, 2nd ed. Chichester: Wiley, 2011.

[3] M. Ochoa, E. Barrigón, L. Barrutia, I. García, I. Rey-Stolle, C. Algora, "Limiting factors on the semiconductor structure of III–V multijunction solar cells for ultra-high concentration (1000–5000 suns)," *Progress in Photovoltaics: Research and Applications*, vol. 24, no. 10, pp. 1332–1345, 2016.

[4] R. Pozner, G. Segev, R. Sarfaty, A. Kribus, Y. Rosenwaks, "Vertical junction Si cells for concentrating photovoltaics," *Progress in Photovoltaics: Research and Applications*, vol. 20, no. 2, pp. 197–208, 2012.

[5] Y. Xing, P. Han, S. Wang, et al., "A review of concentrator silicon solar cells," *Renewable and Sustainable Energy Reviews*, vol. 51, pp. 1697–1708, 2015.

[6] B.L. Sater, N.D. Sater, "High voltage silicon VMJ solar cells for up to 1000 suns intensities," in *Conference Record of the 29th IEEE Photovoltaic Specialists Conference*, New Orleans, 2002, pp. 1019–1022. doi: 10.1109/PVSC.2002.1190778

[7] E.F. Fernández, N. Seoane, F. Almonacid, A.J. García-Loureiro, "Vertical-tunnel-junction (VTJ) solar cell for ultra-high light concentrations (>2000 suns)," *IEEE Electron Device Letters*, vol. 40, no. 1, pp. 44–47, 2019. doi: 10.1109/LED.2018.2880240

[8] C. Outes, E.F. Fernández, N. Seoane, F. Almonacid, A.J. García-Loureiro, "Numerical optimisation and recombination effects on the vertical-tunnel junction (VTJ) GaAs solar cell up to 10,000 suns," *Solar Energy*, vol. 203, pp. 136–144, 2020.

[9] A. Fave, J.-F. Lelièvre, T. Gallet, Q. Su, M. Lemiti, "Fabrication of Si tunnel diodes for c-Si based tandem solar cells using proximity rapid thermal diffusion," *Energy Procedia*, vol. 124, pp. 577–583, 2017.

[10] G. Gaspar, J.M. Serra, J. Kern, M. Müller, "TCAD simulation of electrical characteristics of silicon tunnel junctions for monolithically integrated silicon/perovskite tandem solar cells," *AIP Conference Proceedings*, vol. 2826, 070001, 2023.

[11] A. Gover, P. Stella, "Vertical multijunction solar-cell one-dimensional analysis," *IEEE Transactions on Electron Devices*, vol. ED-21, no. 6, pp. 351–356, 1974. doi: 10.1109/T-ED.1974.17927

[12] Y. Xing, P. Han, S. Wang, et al., "Performance analysis of vertical multi-junction solar cell with front surface diffusion for high concentration," *Solar Energy*, 2013. doi: 10.1016/j.solener.2013.04.030

[13] A. Braun, A. Vossier, E.A. Katz, N.J. Ekins-Daukes, J.M. Gordon, "Multiple-bandgap vertical-junction architectures for ultra-efficient concentrator solar cells," *Energy & Environmental Science*, vol. 5, pp. 8523–8527, 2012.

[14] W. Dawidowski, B. Ściana, I. Zborowska-Lindert, M. Mikolášek, J. Kováč, M. Tłaczała, "Tunnel junction limited performance of InGaAsN/GaAs tandem solar cell," *Solar Energy*, vol. 214, pp. 632–641, 2021.

[15] M. Hermle, G. Létay, S.P. Philipps, A.W. Bett, "Numerical simulation of tunnel diodes for multi-junction solar cells," *Progress in Photovoltaics: Research and Applications*, vol. 16, no. 5, pp. 409–418, 2008.

[16] E.O. Kane, "Theory of tunneling," *Journal of Applied Physics*, vol. 32, no. 1, pp. 83–91, 1961.

[17] G.A.M. Hurkx, D.B.M. Klaassen, M.P.G. Knuvers, "A new recombination model for device simulation including tunneling," *IEEE Transactions on Electron Devices*, vol. 39, no. 2, pp. 331–338, 1992.

[18] A. Schenk, "A model for the field and temperature dependence of Shockley–Read–Hall lifetimes in silicon," *Solid-State Electronics*, vol. 35, no. 11, pp. 1585–1596, 1992.

[19] Y. Yan, *Silicon-Based Tunnel Diode Technology*, Ph.D. dissertation, University of Notre Dame, 2008. doi: 10.7274/7w62f7643

[20] A.E. Atamuratov, B.Q. Jumaboyev, A. Yusupov, A.E. Abdikarimov, A.G. Loureiro, “The effect of geometrical sizes on efficiency of vertical silicon tunnel junction solar cell for high solar concentration,” in *Proc. International Conference on Information Science and Communications Technologies (ICISCT 2022)*, Tashkent, 2022. doi: 10.1109/ICISCT55600.2022.10146907

[21] A.E. Atamuratov, B.Q. Jumaboyev, A.E. Abdikarimov, A. Yusupov, A.G.J. Loureiro, “The effect of height on the efficiency of vertical silicon tunnel junction solar cell for high solar concentration,” in *Proc. 14th Spanish Conference on Electron Devices (CDE 2023)*, Valencia, 2023. doi: 10.1109/CDE58627.2023.10339414

[22] Synopsys Inc., *Sentaurus Device User Guide*, Version O-2018.06. Mountain View, CA, 2018.

UDC: 532.516:519.63:004.942

UNSTEADY FLOW IN A CAVITY WITH A CENTRAL CUTOUT

Ismailov Shikhnazar Rashidovich

Researcher, Tashkent University of Information Technology
tuit.9393@gmail.com

Khasanov Azizbek Bakhodirovich

Researcher, Urganch State University
azizbek.x@urdu.uz

Abdukarimov Nabijon Ibadullayevich

Lecturer, Urgench State University
nabijon.88@urdu.uz

Annotatsiya: Ushbu ishda ikki o‘lchovli siqilmaydigan qovushoq suyuqlikning oqimi ko‘rib chiqiladi. Ushbu oqim ikkita yuqori devorning o‘ng tomonga harakatlanishi natijasida yuzaga keladi. Hisoblash ishlari Reynolds sonining 100 va 400 qiymatlarida amalga oshiriladi. t = 3 s vaqt momentida olingan natijalar o‘tkinchi (nostatsionar) deb qaraladi.

Kalit so’zlar: *Qovushoq oqim, kavernadagi oqim, hisoblash gidrodinamikasi (CFD), sonli modellashtirish, chegaraviy shartlar, oqim funksiyasi.*

Аннотация: Рассматривается двумерное течение несжимаемой вязкой жидкости, приводимое в движение двумя верхними стенками, перемещающимися вправо. Расчёты проводятся при числах Рейнольдса 100 и 400. Результаты, полученные при t = 3 с, рассматриваются как переходные

(нестационарные), поскольку выбранный критерий установления стационарного режима ещё не достигнут.

Ключевые слова: *Вязкое течение, течение в каверне, вычислительная гидродинамика (CFD), численное моделирование, граничные условия, функция тока.*

Abstract: We examine two-dimensional flow of an incompressible viscous fluid driven by two upper walls moving to the right. Calculations are performed at Reynolds numbers of 100 and 400. The results at t = 3 s are treated as transient, since the chosen criterion for a steady state has not yet been met.

Key words: *Viscous flow, cavity flow, computational fluid dynamics (CFD), numerical simulation, boundary conditions, stream function*

Introduction

Cavity flow offers a useful setting for studying how vortices develop and how pressure varies in a confined fluid. Here, we consider a two-dimensional cavity with a central cutout and two upper walls moving in the same direction. The fluid is viscous and incompressible. Reynolds numbers of 100 and 400 are chosen to examine the effect of changing the balance between inertia and viscosity. The calculations use the finite-volume method in OpenFOAM, with PISO coupling for velocity and pressure. We compare velocity magnitude, stream function, vorticity and pressure on meshes of different resolutions, and track changes in the solution over time. These comparisons reveal distinct circulation patterns and provide an initial check on the results. They do not yet establish mesh independence or steady-state behaviour; both require further verification.

Literature review

Previous studies have extensively investigated lid-driven cavity flows. Ghia et al. [1] established benchmark numerical solutions for incompressible viscous flows at different Reynolds numbers. Shankar and Deshpande [2] analysed vortex formation and circulation patterns in driven cavities. Botella and Peyret [3] provided high-accuracy spectral results for validating numerical solutions. Bruneau and Saad [4] further examined the numerical

and physical characteristics of two-dimensional cavity flows. Building on these studies, the present work investigates unsteady flow in a modified cavity with a central cutout and two moving upper walls using OpenFOAM at Reynolds numbers of 100 and 400.

Research Methodology

Geometry and Parameters. The cavity occupies a 3d × 3d square with a d × d cutout at the centre of its upper edge. Below the cutout, the lower section connects the two upper branches, leaving a single fluid domain.

$$\Omega = \{(x, y): 0 < x < 3d,\ 0 < y < 3d,\ (y < 2d) \text{ or } (x < d) \text{ or } (x > 2d)\}.$$

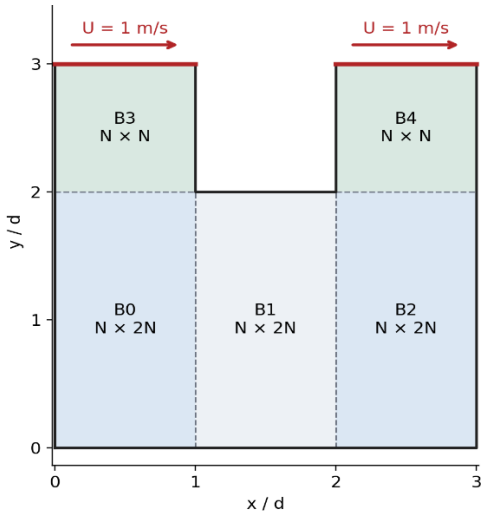


Figure 1. Five blocks form the computational domain. Red arrows indicate the direction of motion of the upper walls, while dashed lines separate adjacent blocks.

Parameter	Value
Characteristic length and velocity	d = 0.1 m; U = 1 m/s
Overall domain size and cutout	0.3 × 0.3 m; 0.1 × 0.1 m
Computational layer thickness	h = 0.01 m; one layer thickness
Area and volume	0.08 m²; 0.0008 m³

Mathematical Model

Density ρ and kinematic viscosity ν are held constant, and body forces are neglected. The pressure variable p used by icoFoam is kinematic pressure; physical pressure is denoted by P.

$$p = \frac{P}{\rho}.$$

The velocity field satisfies the Navier–Stokes equations and the incompressibility condition:

$$\frac{\partial u_x}{\partial t} + u_x \frac{\partial u_x}{\partial x} + u_y \frac{\partial u_x}{\partial y} = -\frac{\partial p}{\partial x} + \nu \left(\frac{\partial^2 u_x}{\partial x^2} + \frac{\partial^2 u_x}{\partial y^2} \right),$$

$$\frac{\partial u_y}{\partial t} + u_x \frac{\partial u_y}{\partial x} + u_y \frac{\partial u_y}{\partial y} = -\frac{\partial p}{\partial y} + \nu \left(\frac{\partial^2 u_y}{\partial x^2} + \frac{\partial^2 u_y}{\partial y^2} \right),$$

$$\frac{\partial u_x}{\partial x} + \frac{\partial u_y}{\partial y} = 0.$$

Initial and Boundary Conditions

The fluid is initially at rest throughout the domain:

$$u_x(x, y, 0) = 0, \qquad u_y(x, y, 0) = 0.$$

At the start of the calculation, both horizontal upper walls begin moving to the right:

$$y = 3d, \qquad 0 < x < d \text{ or } 2d < x < 3d: \qquad u_x = U, \quad u_y = 0.$$

All remaining walls are stationary and satisfy the no-slip condition. This includes the bottom boundary and the vertical faces of the cutout:

$$u_x = 0, \qquad u_y = 0.$$

Velocity is prescribed with the fixedValue boundary condition in OpenFOAM. At the walls, pressure is assigned zeroGradient, following the standard icoFoam setup. The pressure reference is fixed by setting pRefCell to 0 and pRefValue to 0, since the solution otherwise contains an arbitrary additive constant. This choice fixes the reference level; it does not set the physical pressure to zero throughout the cavity.

Where a moving wall meets a stationary wall, each face retains its own prescribed velocity. The resulting jump in boundary values can give rise to local singular behaviour in the solution.

Dimensionless Variables

$$x^* = \frac{x}{d}, \quad y^* = \frac{y}{d}, \quad t^* = \frac{tU}{d}, \quad \mathrm{u}^* = \frac{\mathrm{u}}{U}.$$

$$p^* = \frac{p}{U^2} = \frac{P}{\rho U^2}, \qquad Re_d = \frac{Ud}{\nu}.$$

$$\frac{\partial \mathrm{u}^*}{\partial t^*} + (\mathrm{u}^* \cdot \nabla^*)\mathrm{u}^* = -\nabla^* p^* + \frac{1}{Re_d}\Delta^* \mathrm{u}^*, \qquad \nabla^* \cdot \mathrm{u}^* = 0.$$

We define the Reynolds number using d. Choosing the full cavity length 3d would therefore give a Reynolds number three times as large. The kinematic viscosities used here are 0.001 m²/s at Re = 100 and 0.00025 m²/s at Re = 400. A difference in physical pressure is recovered by multiplying the corresponding difference in kinematic pressure p by the density ρ.

Solution Algorithm and Time Step

Each time step begins with a momentum solve. The finite-volume equation below predicts velocity using the pressure and face fluxes from the previous time step:

$$\frac{V_P}{\Delta t}(\mathrm{u}_P^{n+1} - \mathrm{u}_P^n) + \sum_f \phi_f^n \, \mathrm{u}_f^{n+1} = -V_P(\nabla p)_P^n + \nu \sum_f \frac{S_f}{\delta_f}(\mathrm{u}_N^{n+1} - \mathrm{u}_P^{n+1}).$$

Here, P identifies the current cell and N a neighbouring cell. The symbols V, S and δ denote cell volume, face area and the distance between cell centres, respectively. On boundary faces, the prescribed velocity values are used.

PISO couples the velocity and pressure fields. Dividing the momentum equation by the cell volume gives:

$$a_P \mathrm{u}_P = \mathrm{H}_P - (\nabla p)_P, \qquad r_A = \frac{1}{a_P}, \qquad \mathrm{u}_P = \frac{\mathrm{H}_P}{a_P} - r_A(\nabla p)_P.$$

Inserting this expression for velocity into the incompressibility condition yields the pressure equation: $\nabla \cdot (r_A \nabla p) = \nabla \cdot \left(\frac{\mathrm{H}}{a_P}\right)$.

On the orthogonal mesh, its discrete form is: $\sum_f (r_A)_f \frac{S_f}{\delta_f}(p_N - p_P) = \sum_f \phi_{H,f}$.

The predicted velocity defines the flux φ_H. In icoFoam, the temporal flux correction ddtCorr is also included. The equations above outline the main PISO coupling steps rather than every term in the implementation.

1. Assemble the momentum equation and calculate a provisional velocity.
2. Solve the pressure equation, then correct the face fluxes and cell velocities.
3. Repeat the pressure-correction step; nCorrectors is set to 2.
4. Check flux continuity before proceeding to the next time step.

The pressure equation is solved with PCG and a DIC preconditioner; velocity uses smoothSolver with symGaussSeidel. The absolute tolerance is 10^{-8}. Intermediate pressure solves use relTol = 0.05, whereas pFinal and velocity use relTol = 0. These settings control the algebraic solves. A small residual by itself does not establish that the flow is steady.

Results and Discussion

Post-processing and Verification of Results

We use the following definitions of stream function ψ and vorticity ω:

$$u_x = \frac{\partial \psi}{\partial y}, \qquad u_y = -\frac{\partial \psi}{\partial x}, \qquad \omega_z = \frac{\partial u_y}{\partial x} - \frac{\partial u_x}{\partial y}, \qquad \Delta\psi = -\omega_z.$$

Since the boundary forms one closed, impermeable contour, ψ may be set to zero along it. Stream function has units of m^2/s, and vorticity has units of s^{-1}. At a given time, the contours of ψ are streamlines. They should not be interpreted as the paths followed by fluid particles throughout the unsteady motion. The original report identifies OpenFOAM v1912 as the software used for these calculations. After an error was found in the standard post-processing procedure, the stream function was reconstructed from the saved face fluxes φ. Vorticity was calculated directly from the velocity field. For a computational layer of thickness h, the stream-function differences were obtained from:

$$\psi_{\text{top}} - \psi_{\text{bottom}} = \text{sign}(S_x)\frac{\phi_f}{h}, \qquad \psi_{\text{right}} - \psi_{\text{left}} = -\text{sign}(S_y)\frac{\phi_f}{h}.$$

The stream-function differences were fitted by least squares. The reported maximum relative residual, 4.277×10^{-10}, measures agreement between the reconstructed stream

function and the saved fluxes. It does not quantify the overall error of the Navier–Stokes solution.

Velocity and Stream Function

Both plots correspond to N = 40 at t = 3 s, with Re = 100 on the left and Re = 400 on the right. Red segments identify the moving walls.

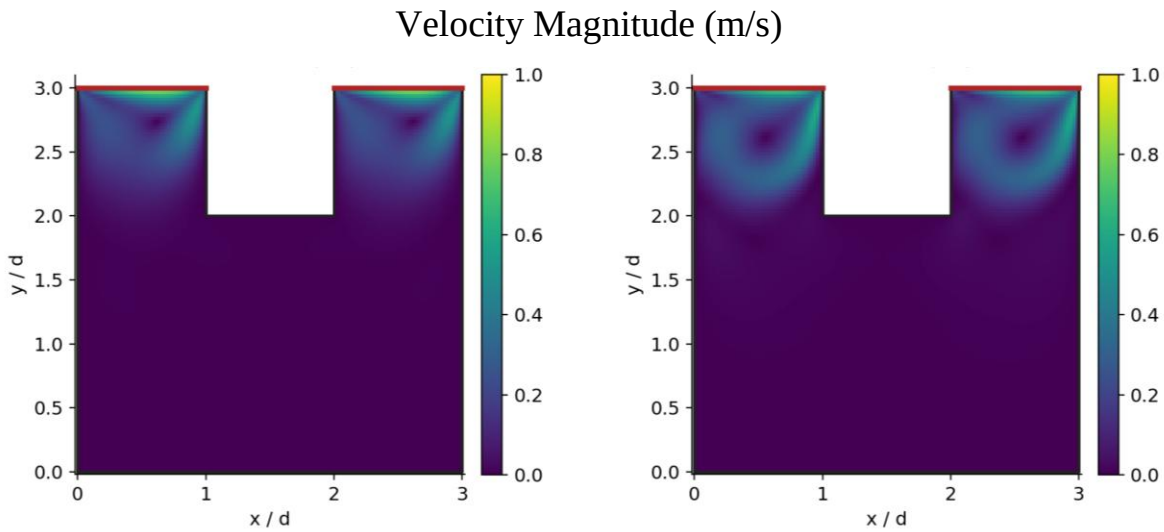


Figure 2. Velocity magnitude, with a common scale of 0–1 m/s for both cases. The largest velocities occur near the moving upper walls.

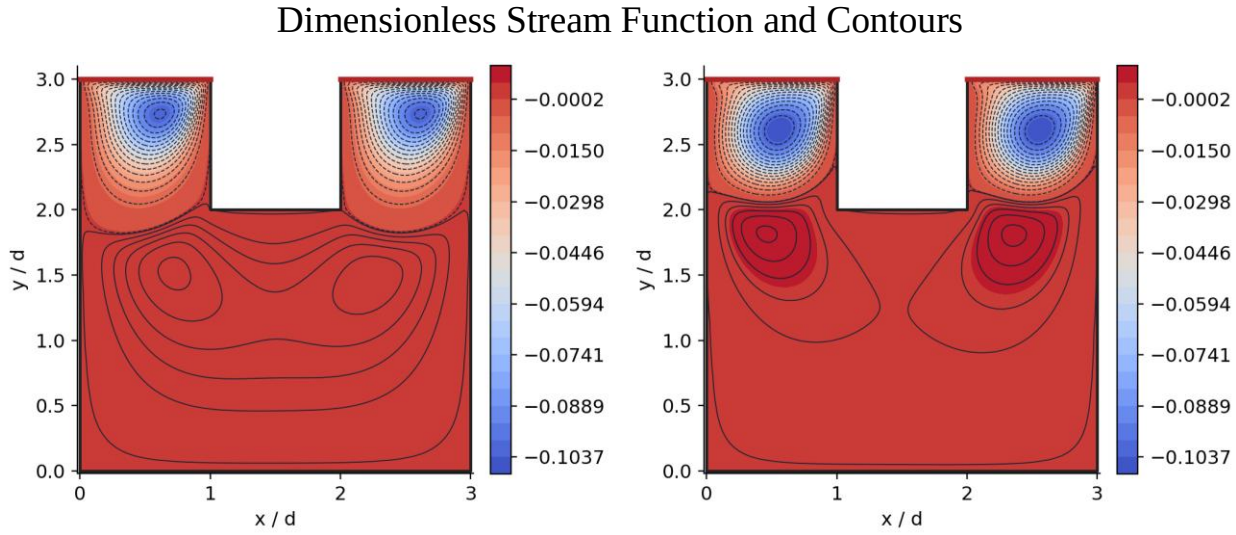


Figure 3. Dimensionless stream function ψ/(Ud). The main circulation occupies the upper branches, with weaker return flow in the lower part of the cavity.

The small vortices shown here belong to this particular transient solution. Their persistence and locations still need to be checked on finer meshes and at later times.

Pressure and Further Verification

The pressure plots again show N = 40 at t = 3 s: Re = 100 is on the left and Re = 400 on the right. Kinematic pressure is measured relative to the domain average and is expressed in m^2/s^2.

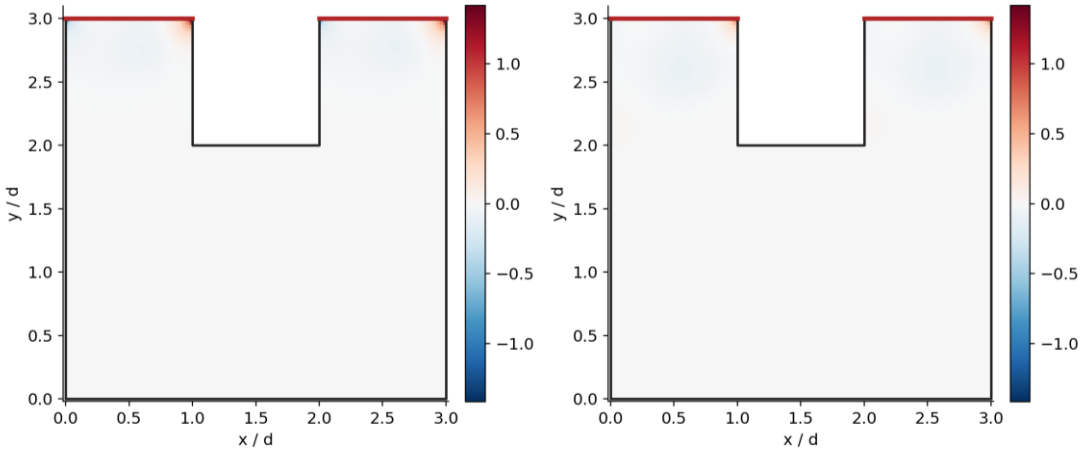


Figure 4. Kinematic pressure relative to the domain mean, plotted with the same colour-scale limits for both cases.

Conclusion and Recommendations

The next step is a comparison with N = 80, followed by a separate time-step study on a fixed mesh. Each run should continue until the convergence criterion holds over several successive intervals. Both cell-level mass conservation and the overall mass balance must also be checked.

References:

[1]. Ghia, U., Ghia, K. N., & Shin, C. T. High-Re solutions for incompressible flow using the Navier–Stokes equations and a multigrid method. Journal of Computational Physics, 48(3), 387–411, 1982.

[2]. Shankar, P. N., & Deshpande, M. D. Fluid mechanics in the driven cavity. Annual Review of Fluid Mechanics, 32, 93–136, 2000.

[3]. Botella, O., & Peyret, R. Benchmark spectral results on the lid-driven cavity flow. Computers & Fluids, 27(4), 421–433, 1998.

[4]. Bruneau, C.-H., & Saad, M. The 2D lid-driven cavity problem revisited. Computers & Fluids, 35(3), 326–348, 2006.

[5]. Sahin, M., & Owens, R. G. (2003). A novel fully implicit finite volume method applied to the lid-driven cavity problem—Part I: High Reynolds number flow calculations. International Journal for Numerical Methods in Fluids, 42, 57–77.

[6]. AbdelMigid, T. A., Saqr, K. M., Kotb, M. A., & Aboelfarag, A. A. (2017). Revisiting the lid-driven cavity flow problem: Review and new steady state benchmarking results using GPU accelerated code. Alexandria Engineering Journal.

[7]. Issa, R. I. (1986). Solution of the implicitly discretised fluid flow equations by operator-splitting. Journal of Computational Physics, 62(1), 40–65.

[8]. Issa, R. I., Gosman, A. D., & Watkins, A. P. (1986). The computation of compressible and incompressible recirculating flows by a non-iterative implicit scheme. Journal of Computational Physics, 62(1), 66–82. [9]. Patankar, S. V. (1980). Numerical Heat Transfer and Fluid Flow. Hemisphere Publishing Corporation.

[10]. Versteeg, H. K., & Malalasekera, W. (2007). An Introduction to Computational Fluid Dynamics: The Finite Volume Method (2nd ed.). Pearson Education.

[11]. Jasak, H. (1996). Error Analysis and Estimation for the Finite Volume Method with Ations to Fluid Flows. PhD thesis, Imperial College London.

[12]. Weller, H. G., Tabor, G., Jasak, H., & Fureby, C. (1998). A tensorial approach to computational continuum mechanics using object-oriented techniques. Computers in Physics, 12(6), 620–631.

[13]. Tabor, G. (2022). Implementation of a Modified Lid Driven Cavity in OpenFOAM. OpenFOAM Journal, 2, 62–80.

UDC: 538.9:004.94

COMPUTER SIMULATION OF ANGULAR AND ENERGY DISTRIBUTIONS OF Ne^+ IONS SCATERRED FROM THE $Si_{0.25}Ge_{0.75}(100)$ SURFACE

Kutliyev Uchkun Otoboyevich
professor, Urgench State University named after Abu Rayhan Beruni
kutliev.u.o@gmail.com
Bekchanova Kuvonch Kuvondikovna
Assistant teacher, Urgench State University named after Abu Rayhan Beruni
quvonchoybekchanova95@gmail.com

Annotatsiya. Ushbu ishda Ne^+ ionlarining $Si_{0.25}Ge_{0.75}(100)$ materialining sirtidan sochilish jarayoni kompyuter modellashtirish usuli yordamida tadqiq etilgan. Ne^+ ionlarining 1–5 keV energiya oralig‘idagi sochilish jarayoni ikkilik to‘qnashuvlar yaqinlashuviga (Binary Collision Approximation — BCA) asoslangan hisoblash usuli yordamida o‘rganilgan. Modelda nishon material sirtining kristall tuzilishi hisobga olingan hamda tushuvchi ionlarning nishon atomlari bilan ketma-ket o‘zaro ta’sirlashuvi natijasida yuzaga keladigan trayektoriyalari kuzatilgan. Ko‘p sonli ion trayektoriyalarining statistik tahlili asosida sochilgan ionlarning burchak va energiya taqsimotlari aniqlangan. Shuningdek, tushuvchi ion turi va nishon material tarkibining sochilish xarakteristikalariga ta’siri ham o‘rganilgan.

Kalit so‘zlar: *SiGe, ionlar sochilishi, binary collision approximation, yarimkanal, ion trayektoriyalari, sirt kanallashishi.*

Аннотация. В данной работе методом компьютерного моделирования исследуется процесс рассеяния ионов Ne^+ на поверхности материала $Si_{0.25}Ge_{0.75}(100)$. Рассеяние ионов Ne^+ в диапазоне низких энергий 1–5 кэВ изучается с использованием вычислительного метода, основанного на приближении бинарных столкновений (Binary Collision Approximation — BCA). В модели учитывается кристаллическая структура поверхности мишени, а также отслеживаются траектории падающих ионов, возникающие в результате последовательных взаимодействий с атомами мишени. На основе статистического анализа большого количества ионных траекторий

определяются угловые и энергетические распределения рассеянных ионов. Кроме того, исследуется влияние сорта падающих ионов и состава материала мишени на характеристики рассеяния.

Ключевые слова: *SiGe, рассеяние ионов, приближение парных столкновений, полуканал, траектории ионов, поверхностное каналирование*

Abstract. In this work, the scattering of Ne^+ ions from the surface of a $Si_{0.25}Ge_{0.75}(100)$ material is investigated by computer simulation. The scattering of Ne^+ ions in the low-energy range of 1–5 keV is studied using a computational method based on the binary collision approximation. The crystalline structure of the target surface is taken into account in the model, and the trajectories of incident ions resulting from successive interactions with target atoms are tracked. Statistical analysis of a large number of ion trajectories is used to determine the angular and energy distributions of scattered ions. The influence of the incident ion species and of the target composition on the scattering characteristics is also examined.

Key words: *SiGe, ion scattering, binary collision approximation, semichannel, ion trajectories, surface channeling*

Introduction

Because the structural and physical properties of SiGe alloys can be tuned by changing their composition, they are among the important materials in modern semiconductor technology [1]. The study of the surface and bulk properties of Ge-rich SiGe systems is particularly important for investigating ion–solid interactions. The interaction of low-energy ions with a solid surface proceeds through successive collisions with surface atoms, energy loss, and changes in the direction of motion [2,3,4,5,6]. The energy and angular distributions of scattered ions provide important information about these microscopic processes.

Literature Review

A number of experimental and theoretical studies have addressed the scattering of ions from Si and Ge surfaces. In particular, the effect of the ion species and the initial energy on the energy distributions of Ne^+ and Ar^+ ions scattered from Si surfaces has been investigated [7,8,9,10]. For the scattering of Ne^+ and Ar^+ ions from Ge surfaces in

the 1–5 keV energy range, studies have analyzed the energy spectra of scattered ions and multiple-collision processes [11,12,13,14]. Work on modeling the trajectories and angular distributions of Ne^+ and Ar^+ ions on crystalline semiconductor surfaces has also been reported [15].

Ion scattering and ion irradiation in SiGe systems have also been studied with respect to their effects on surface composition, crystallinity and atomic redistribution. However, the scattering characteristics of ions may differ substantially when the composition and crystallographic orientation of the SiGe alloy change. Therefore, detailed modeling of Ne^+ ion scattering from the Ge-rich $Si_{0.25}Ge_{0.75}(100)$ surface is one of the pressing problems.

The aim of this work is to model the scattering of 1–5 keV Ne^+ ions from the $Si_{0.25}Ge_{0.75}(100)$ surface, to determine the ion trajectories in the crystal lattice, and to analyze the angular and energy distributions of the scattered ions. The results make it possible to determine the influence of the ion species and the initial energy on the scattering process at a Ge-rich SiGe surface.

Research Methodology

The (100) surface of the $Si_{0.25}Ge_{0.75}$ alloy was considered in this study. The surface model is based on the arrangement of Si and Ge atoms in the crystal lattice. Ne^+ ions with initial energies of 1–5 keV were used in the calculations.

For each calculation condition, a large number of ion trajectories were computed and the results were analyzed statistically; 1000 ion trajectories are considered for each calculation condition. The ion motion in the crystal is modeled within the binary collision approximation (BCA) [16,17,18,19,20]. In this approximation, the complex many-body interaction of the ion in the crystal is treated as a sequence of successive ion–atom two-body collisions.

The atomistic structure of the $Si_{0.25}Ge_{0.75}(100)$ surface used in the calculations was geometrically optimized with the VASP code. Based on the optimized structure, the relevant interatomic distances between surface atoms were measured with the VESTA program. The determined distances were introduced into the calculation code as

geometric parameters for modeling ion motion and scattering along the surface [21]. The atomistic structure of the optimized $Si_{0.25}Ge_{0.75}(100)$ surface is shown in Figure 1.

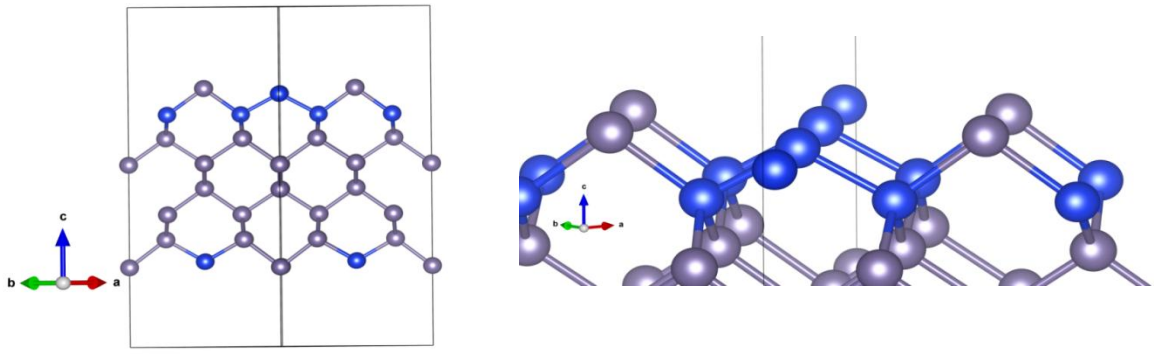


Figure 1. Atomistic structure of the optimized $Si_{0.25}Ge_{0.75}(100)$ surface (blue ball – Si, grey ball – Ge).

The elastic interaction in ion–atom collisions is described using the Ziegler–Biersack–Littmark (ZBL) universal screened nuclear potential [2]. The ZBL potential describes the Coulomb interaction between atomic nuclei, taking into account the screening effect of electrons, and is used to describe ion–atom collisions over a wide range of energies and interatomic distances. The potential is written in the following form:

$$E_1 = (1+\mu)^{-2} E_0 (\cos\theta_1 \pm \sqrt{(f\mu)^2 - \sin^2\theta_1})^2$$

The inelastic energy losses arising during the ion's motion in the crystal are taken into account on the basis of the Firsov formula in the form modified by Kishinevskiy [3]. This approach describes the decrease in the ion's energy during collisions.

The energies and directions after an elementary collision between the ion and a surface atom are determined from the conservation laws of energy and momentum in classical mechanics. Within the BCA, the ion's motion in the crystal is treated as a set of successive ion–atom two-body collisions. After each collision, the ion's energy, velocity and direction are updated and used as the initial parameters for the next collision. For each calculation condition, 1000 ion trajectories were computed, and the resulting angular and energy distributions of the scattered ions were analyzed statistically. Calculations were performed for Ne^+ ions with initial energies of 1–5 keV at incidence angles in the range 1°–15°. For each calculation condition, 1000 ion

trajectories were computed, and the resulting angular and energy distributions of the scattered ions were analyzed statistically. The calculations yielded the angular and energy distributions that describe the scattering process, and the influence of the initial ion energy and incidence angle on the scattering process at the $Si_{0.25}Ge_{0.75}(100)$ surface was analyzed.

Results and Discussion

Below, to analyze the effect of the initial ion energy on the scattering process, the angular distributions obtained at 1, 3 and 5 keV are presented in Figure 2. These results allow the energy distribution of scattered ions at different incidence angles to be compared. The graphs show the angular distributions $dN/d\varphi$ of Ne^+ ions scattered from the monocrystalline $Si_{0.25}Ge_{0.75}(100)$ alloy surface along the [110] crystallographic direction, for different initial energies (1, 3 and 5 keV) and small incidence angles (1°–15°). The spectra show how the physical mechanisms of particle–surface interaction change with incidence angle; in particular, the evolution from pure specular reflection to the complex surface channeling regime is shown. At small incidence angles (1°, 3° and 5°; left column of graphs), a pronounced central peak located near $\psi = 0°$ dominates the distributions for all energies studied. The maximum intensity is observed at an incidence angle of 1° for all energies and reaches approximately 160 relative units. This indicates that the incident particles are reflected mainly specularly from the uppermost layer of the target and do not penetrate deeply into it. As the incidence angle increases to 5°, the intensity of the central peak falls sharply and the distribution broadens (an increase in the full width at half maximum, FWHM). This change is associated with an increase in the probability of multiple scattering as particles partly overcome the potential barrier and move into deeper layers. At intermediate incidence angles (7°–11°; middle column), the dependence of the process on the initial energy becomes more pronounced. At the lowest energy (1 keV, upper row), the transition to the surface channeling regime occurs at the smallest critical angles. In this regime the intensity of the central peak drops sharply, and the beam distribution splits into distinct, symmetric side peaks in the region $\psi \approx \pm 10°$. This proves that the atomic half-channels formed along the [110]

direction of the (100) surface strongly focus low-energy particles along their axis. When the initial energy is raised to 3 and 5 keV (middle and lower rows), the surface channeling mechanism weakens. Higher-energy particles overcome the surface lattice barrier more easily and enter the crystal lattice, so the central peak remains dominant at 7°–11° (intensity of about 40–55 units).

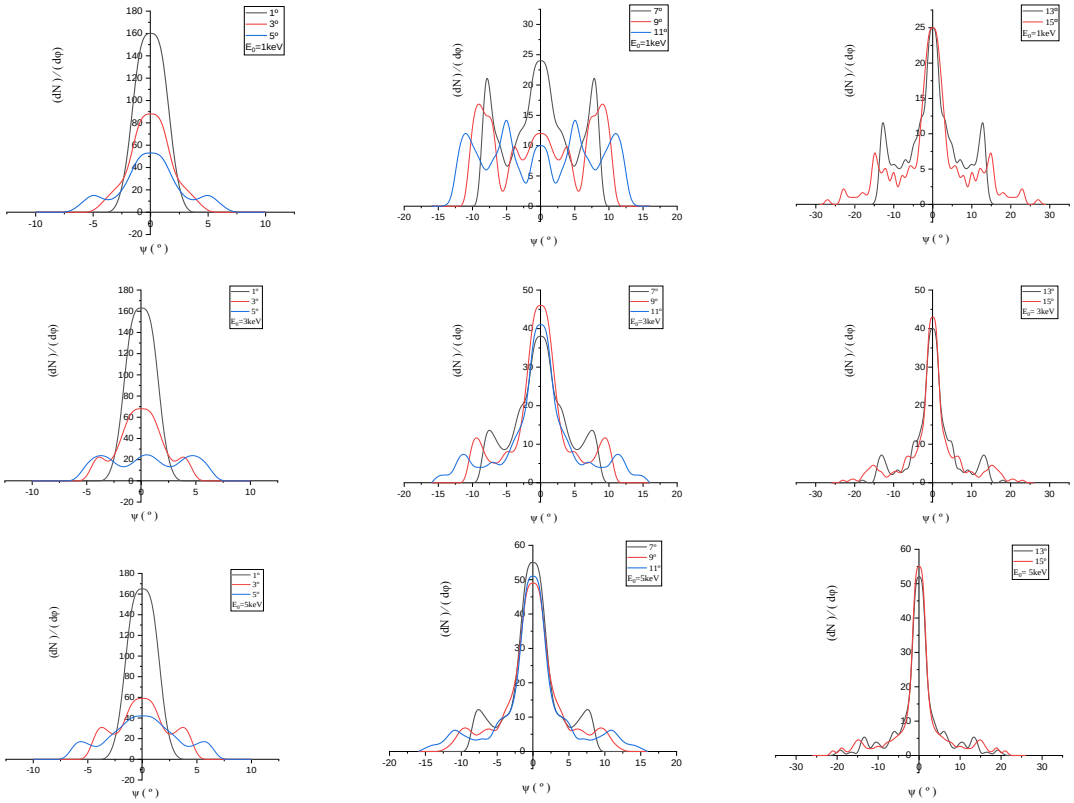


Figure 2. Angular distributions of scattered Ne^+ ions for various incidence angles at initial energies of 1, 3 and 5 keV.

At large incidence angles (13° and 15°; right column), the scattering pattern again changes its shape. At 1 keV, the particles are still influenced by the surface architecture and form a complex multi-peak structure as a result of channeling and of blocking by neighboring atoms in the crystal. However, at 5 keV (lower right graph), the beam distribution is concentrated almost entirely in an intense central maximum (intensity of 50–60 units). This shows that at high energy and large incidence angle the particles penetrate rapidly into deeper layers (dechanneling regime), and the guiding structural effects of the crystal surface lose their main role in shaping the angular distribution.

The energy distributions (dN/dE) of scattered Ne^+ ions from the $Si_{0.25}Ge_{0.75}$ surface for initial kinetic energies E_0 = 1, 3 and 5 keV are presented in Figure 2. The

calculations were carried out over a wide range of incidence angles (1° to 15°), and reflect the atomic structure of the alloy surface and the scattering dynamics.

Low-energy regime dynamics (E_0 = 1 keV):

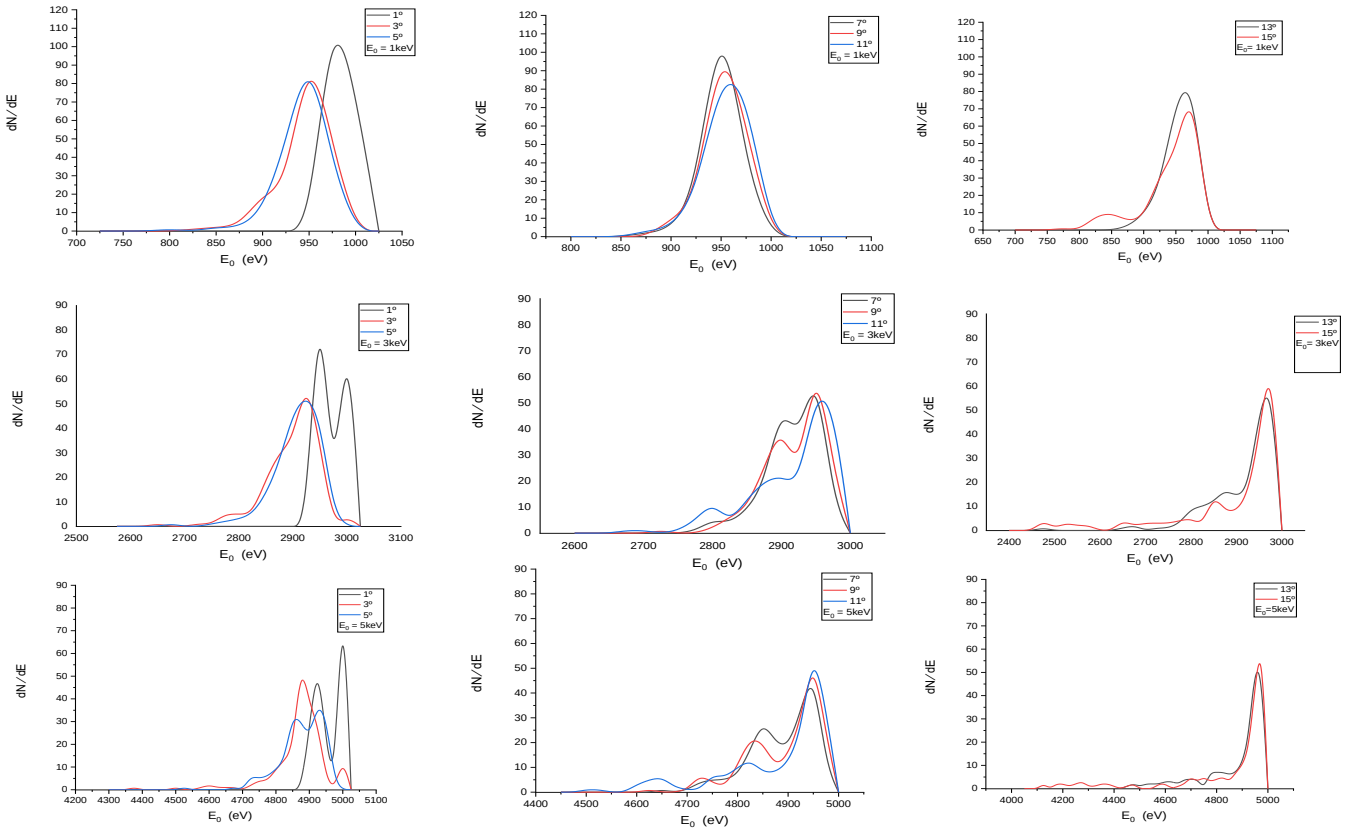


Figure 2. Energy distributions of scattered Ne^+ ions for various incidence angles at initial energies of 1, 3 and 5 keV.

At an initial energy of 1 keV, for all angles analyzed, the spectra take the form of a single broadened and asymmetric peak. At a small grazing angle (1°), most of the ions are scattered with an energy of about 980 eV; as the angle increases to 5°, this maximum shifts toward lower energies (about 950 eV) and the FWHM of the spectrum increases. This is explained by the increased probability of multiple-scattering sequences between the ion and surface atoms and by the angle dependence of inelastic energy losses. At this energy, the mass difference between Si and Ge atoms does not provide sufficient kinematic resolution to form separate peaks in the spectrum. Medium- and high-energy regimes: isotopic/elemental separation (E_0 = 3 keV and 5 keV): When the ion energy is increased to 3 and 5 keV, qualitative changes occur in the morphology of the energy spectra; in particular, the peaks clearly split. For E_0 = 5 keV and an incidence angle of

1°, two sharp, separate peaks form in the spectrum, with kinetic energies of about 4900 eV and 4980 eV. This double-peak structure is directly related to the differences in the kinematic factors for quasi-single elastic scattering of Ne^+ ions from atoms of different mass in the alloy: silicon (Si, 28 amu) and germanium (Ge, 72 amu). According to the laws of elastic collisions, Ne^+ ions scattered from the heavier germanium atoms retain more kinetic energy, giving the dominant high-energy peak (~4980 eV). Ions colliding with the lighter silicon atoms lose more energy, which gives rise to the lower-energy peak (~4900 eV). The ratio of the peak intensities is proportional to the stoichiometric composition of the near-surface layer of the alloy (25% Si and 75% Ge) and to the scattering cross-sections of these elements.

Angular effect and subsurface scattering:

The spectra at E_0 = 3 and 5 keV show that, as the scattering angle increases from 7° to 15°, additional structures (shoulders) begin to develop in the low-energy part of the spectrum. For example, at 3 keV and an angle of 15°, broadened spectral tails form around ~2800 eV and ~2900 eV. This is explained by the contribution of ions that penetrate sub-surface layers, undergo multiple wide-angle collisions, and then leave the surface. The sharp, narrow peaks obtained at small angles (1°–5°) mainly reflect the interaction with the uppermost atomic monolayer of the surface, which proves the very high surface sensitivity of the method.

Conclusion and Recommendations

In this study, the structural and elemental features of the $Si_{0.25}Ge_{0.75}$ semiconductor alloy surface were analyzed by computer simulation of the scattering of low-energy Ne^+ ions over a range of initial energies (E_0 = 1, 3, 5 keV) and scattering angles (1°–15°). The main conclusions are as follows:

1. Dependence of kinematic resolution on energy: An increase in the initial kinetic energy (in particular in the 3 and 5 keV regimes) significantly enhanced the kinematic differences in the scattering of Ne^+ ions from centers of different mass. This made it possible to distinguish clearly the quasi-single elastic scattering peaks from silicon and germanium atoms of the alloy surface and to resolve them as two peaks in the spectrum.

2. Very high sensitivity to the surface monolayer: At small grazing angles (1°–5°), the sharpness of the spectral peaks reflects the state of the uppermost atomic layer of the surface. This regime creates ideal conditions for determining the surface stoichiometry of the alloy. Multiple-collision dynamics: An increase in the scattering angle (7°–15°) and the low-energy regime (1 keV) led to asymmetric broadening of the energy spectra and the appearance of additional low-energy structures. This indicates that the probability of Ne^+ ions penetrating sub-surface layers increased and that multiple inelastic collision processes were activated. The high fraction of the heavier Ge atoms (75%) in the alloy determined the dominant high-energy peak. The study confirms that ion probing with Ne^+ ions is an effective, high-precision and minimally invasive tool for investigating surface processes, elemental composition and atomic dynamics in multicomponent systems such as $Si_{1-x}Ge_x$.

References:

[1] W. P. A. Jansen, A. Knoester, A. J. H. Maas, P. Schmit, A. Kytökivi, A. W. Denier v.d. Gon, H. H. Brongersma, “Influence of compaction and surface roughness on low-energy ion scattering signals” Surface and interface analysis, volume 36, Issue 11, https://doi.org/10.1002/sia.1921

[2]J. M. Ziman, “ Electrons and Phonons: The Theory of Transport Phenomena in Solids” Oxford Scholarship Online:September 2007, DOI:10.1093/acprof:oso/9780198507796.001.000

[3]D. J. Paul, “Si/SiGe heterostructures: from material and physics to devices and circuits,” Semiconductor Science Technology (2004).

[4]Grehl, T., Brüner, P., Brongersma, H. H. "Low-Energy Ion Scattering (LEIS)". Surface and Interface Analysis.(2024).

[5]K. Nordlund, "Primary radiation damage: A review of current understanding and models". Journal of Nuclear Materials (2018)

[6]A.Mutzke . "SDTrimSP Version 6.00: Simulation of ion dynamics and target interactions". Max-Planck-Institut for Plasmaphysik Reports (2019)

[7]Y.W. Mo, D.E. Savage, M.G. Lagally, B.S. Swartzentruber "Kinetic pathway in Stranski–Krastanov growth of Ge on Si(001)." Physical Review Letters (1990).

[8]Buck, T. M., Wheatley, G. H., & Jackson, D. P. "Low energy noble-gas ion scattering from Si (100) and Si (111) surfaces." Nuclear Instruments and Methods in Physics Research (1983).

[9] Niehus, H., Heiland, W., Taglauer, E. "Ion-solid interaction at low energies: Application to surface structure determination." Surface Science Reports, (1993).

[10] Markin, S. N. "Charge exchange of low energy Ne^+ and Ar^+ ions scattered from a Si(100) surface." Physical Review B, (2009).

[11] Eckstein, W. - Computer Simulation of Ion-Solid Interactions. Springer Series in Materials Science.(2013)

[12] Sadullayev, S., Kutliev, U., Saidova, A., Jumanazarov, G., Ruzmetov, R. (2025). Investigation of Ar+ Ions Scattering from the Surface of CdTe(001) <110> at the Glancing Incidence. East European Journal of Physics, (2), 206-210. https://doi.org/10.26565/2312-4334-2025-2-21

[13] Kutliev U., Sadullaev Sh., Saidova A. and Tangribergenov I, "Studying the Trajectory of Small-Angle Scattered Ar+ Ionsfrom CdTe(001) <110> Surface Semichannel", Int. J. Thin. Fil. Sci. Tec. 14, No. 1, 11-14 (2025). http://dx.doi.org/10.18576/ijtfst/140102

[14] Dzhurakhalov, A. A., Rasulov, A. M. (2001). "Simulation of multiple scattering of low-energy ions from semiconductor surfaces." Vacuum, 62(2-3), 257-263.

[15] Parilis, E. S., Turaev, N. Y., Umarov, F. F., et al. Atomic Collisions on Solid Surfaces. Elsevier Science (North-Holland) (1993).

[16] Aono, M., Oshima, C., Zaima, S., Otani, S., Ishizawa, Y. "Quantitative surface atomic geometry and two-dimensional alloy formation analysis by low-energy ion scattering." (1981).

[17] M.K. Karimov*, F.O. Kuryozov, Sh.R. Sadullaev, M.U. Otabaev, S.B. Bobojonova, Investigation of Defect InP(001) Surface by Low Energy Ion Scattering Spectroscopy, Materials Science Forum(2022). https://doi.org/10.4028/www.scientific.net/MSF.1049.192

[18] Robinson, M. T., & Torrens, I. M. "Computer simulation of atomic-displacement cascades in solids in the binary-collision approximation." Physical Review B, (1974).

[19] A.A Dzhurakhalov, B.S. Kalandarov, M. Kurbonov, U.O. Kutliev, H. Dreysse, "Study of ion scattering and dechanneling from surface defect structure by computer simulation", Computational Materials Science (2002),

[20] Ashirov A. S., Qurbanov M. K., Tangribergenov I. U., Karimov M. K., Otabaeva K. U. Inelastic Energy Loss of Ar Ions Scattered Al_2O_3 Surface under Grazing Incidence // Physics and Chemistry of Solid State. – 2021. – Vol. 22, No. 2. – P. 255–259. – DOI: https://doi.org/10.15330/pcss.22.2.255-259.

[21] https://jp-minerals.org/vesta/en/

UDK: 621.383.52: 620.18

EDS ANALYSIS OF Ti/Cu/Sn/Ni PRECURSORS FOR THIN-FILM SOLAR CELLS

Utamuradova Sharifa Bekmuradovna
O‘zMU huzuridagi Yarimo‘tkazgichlar fizikasi va mikroelektronika ITI
Fayzullayev Qahramon Mahmudjonovich
O‘zMU huzuridagi Yarimo‘tkazgichlar fizikasi va mikroelektronika ITI
qahramonfayzullayev8@gmail.com
Stanchik Aliona Viktorovna
Belarus Milliy Fanlar Akademiyasi Materialshunoslik IICHB
Xamidova Nigora A’zamjon qizi
Namangan davlat universiteti magistranti

Annotatsiya: Mazkur maqolada $Cu_2NiSn(S,Se)_4$ yupqa pardali quyosh elementlarini olish uchun egiluvchan titan tagligida ketma-ket magnetronli purkash usuli bilan sintez qilingan Ti/Cu/Sn/Ni ko‘p komponentli prekursor geterostrukturasining energiya-dispersiyali rentgen spektroskopiyasi (EDS/EDX) natijalari keltirilgan. E_0 = 20.0 kV tezlatuvchi kuchlanishda olingan spektrlar asosida barcha funksional qatlamlarning (Cu, Ni, Sn), taglikning (Ti) va sirtqi fon aralashmalarining (C, O) miqdoriy atom hamda massaviy ulushlari aniqlandi. Taglik va fon elementlarini chiqarib tashlagan holda metallarning qayta normallashtirilgan tarkibi (Cu = 45.25 at.%, Ni = 33.00 at.%, Sn = 21.75 at.%) hisoblandi. Olingan natijalar yuqori samaradorlikdagi fotovoltaik absorberlarni sintez qilish uchun talab etiladigan mis bo‘yicha kambag‘allashgan (Cu-poor) rejim shakllanganligini tasdiqlaydi.

Kalit so‘zlar: *EDS analiz, Ti/Cu/Sn/Ni geterostrukturasi, stexiometriya, kation nisbatlari, Cu-poor rejimi, $Cu_2NiSn(S,Se)_4$, magnetronli purkash.*

Аннотация: В настоящей статье представлены результаты энергодисперсионной рентгеновской спектроскопии (EDS/EDX) многокомпонентной прекурсорной гетероструктуры Ti/Cu/Sn/Ni, синтезированной методом последовательного магнетронного распыления на гибкой титановой подложке для получения тонкоплёночных солнечных элементов Cu2NiSn(S,Se)4. На основании спектров, полученных при

ускоряющем напряжении E0 = 20,0 кВ, определены количественные атомные и массовые доли всех функциональных слоёв (Cu, Ni, Sn), подложки (Ti) и поверхностных фоновых примесей (C, O). После исключения элементов подложки и фона рассчитан пересчитанный (нормированный) состав металлов (Cu = 45,25 ат.%, Ni = 33,00 ат.%, Sn = 21,75 ат.%). Полученные результаты подтверждают формирование режима с обеднением по меди (Cu-poor), необходимого для синтеза высокоэффективных фотовольтаических поглотителей.

Ключевые слова: *EDS-анализ, гетероструктура Ti/Cu/Sn/Ni, стехиометрия, катионные соотношения, режим Cu-poor, Cu2NiSn(S,Se)4, магнетронное распыление.*

Abstract: This paper presents the results of energy-dispersive X-ray spectroscopy (EDS/EDX) of a multicomponent Ti/Cu/Sn/Ni precursor heterostructure synthesized by sequential magnetron sputtering on a flexible titanium substrate for the fabrication of Cu2NiSn(S,Se)4 thin-film solar cells. Based on the spectra obtained at an accelerating voltage of E0 = 20.0 kV, the quantitative atomic and mass fractions of all functional layers (Cu, Ni, Sn), the substrate (Ti), and surface background impurities (C, O) were determined. After excluding the substrate and background elements, the renormalized metal composition was calculated (Cu = 45.25 at.%, Ni = 33.00 at.%, Sn = 21.75 at.%). The obtained results confirm the formation of the copper-poor (Cu-poor) regime required for the synthesis of high-efficiency photovoltaic absorbers.

Keywords: *EDS analysis, Ti/Cu/Sn/Ni heterostructure, stoichiometry, cation ratios, Cu-poor regime, Cu2NiSn(S,Se)4, magnetron sputtering.*

Introduction

Accurate control of the elemental composition and stoichiometry of the initial metal precursors plays a crucial role in the synthesis of $Cu_2NiSn(S,Se)_4$ chalcogenide compounds, which are considered promising absorber materials for thin-film solar cells [1–2]. Currently, numerous scientific studies are investigating various multicomponent precursor systems (e.g., Cu-Zn-Sn, Cu-Ni-Sn, and Cu-Sn-Ni-based layers) for the fabrication of alternative kesterite-type thin films. In particular, the literature indicates that phase formation processes involving sequential magnetron sputtering of metal

precursors followed by high-temperature chalcogenization require particular attention [3]. In this process, carried out by magnetron sputtering using individual Cu, Sn, and Ni targets, the primary objective is to ensure highly accurate quantitative monitoring of the atomic concentrations of the constituent elements and to maintain compositional stability.

The main objective of this study is to perform a quantitative analysis of the Ti/Cu/Sn/Ni multilayer heterostructure using energy-dispersive X-ray spectroscopy (EDS/EDX), calculate the normalized cation ratios while excluding contributions from the substrate matrix and surface background impurities, and physically evaluate the thickness of the functional coating based on the excitation depth of characteristic X-ray radiation.

Experimental part

The Ti/Cu/Sn/Ni precursor structure was synthesized by sequential magnetron sputtering in a magnetron sputtering system under a high-purity argon atmosphere. Quantitative elemental microanalysis was performed using energy-dispersive X-ray spectroscopy (EDS) coupled with a Compact-W 2020 scanning electron microscope. The spectrometric measurements were carried out at an accelerating voltage of E0=20.0 kV. Analytical spectra were acquired over an energy range of 0–15 keV by identifying the K- and L-series characteristic lines of the constituent elements: Ti (K-series ~4.51 keV), Cu (K-series ~8.04 keV, L-series ~0.93 keV), Ni (K-series ~7.47 keV, L-series ~0.85 keV), Sn (L-series ~3.44 keV), as well as the background signals of C (K-series ~0.28 keV) and O (K-series ~0.52 keV). Quantitative determination of the atomic fractions (at.%) was performed using standard ZAF corrections.

Results and Discussion

To experimentally verify the effectiveness of the magnetron sputtering process in multilayer Ti/Cu/Sn/Ni systems and determine the spatial distribution of the elemental composition, local energy-dispersive X-ray spectroscopy (EDS) analysis was performed. The quantitative results, expressed in atomic percentages (at.%), demonstrate full consistency with the technological parameters of the sequential deposition process involving copper, tin, and nickel targets onto a titanium foil substrate.

According to the obtained analytical results, the titanium content is 31.24 at.%. The high intensity of its K peak (K ~ 4.51 keV) clearly confirms that, under the selected accelerating voltage conditions, the electron probe penetrates the sputtered thin films and also detects the characteristic signal originating from the titanium foil serving as the substrate. This observation indirectly suggests that the overall geometric thickness of the deposited coating lies within the deep excitation range of the substrate atoms, corresponding to submicron dimensions [4,5].

Table 1. EDS analysis results of the Ti/Cu/Sn/Ni multilayer precursor structure (including atomic, mass, and normalized metallic fractions).

lement	Atomic fraction (at.%)	Mass fraction (wt.%)	Normalized composition	
			Atomic fraction (at.%)	Mass fraction (wt.%)
C	15.72	5.41 %	–	–
O	12.25	5.62 %	–	–
Ti	31.24	42.86 %	–	–
Ni	13.46	22.64 %	33.00	26.21 %
Cu	18.46	33.62 %	45.25	38.89 %
Sn	8.88	30.21 %	21.75	34.92 %
Total	**100.00**	**100.00 %**	**100.00**	**100.00**

The functional coating formed through sequential magnetron sputtering of individual targets is characterized by the following elemental concentrations: copper — 18.46%, nickel — 13.46%, and tin — 8.88%. This distribution of elemental concentrations indicates a high degree of stability in the deposition rates, as well as strong adhesion of the sputtered atoms to the titanium surface and between the individual layers.

Particular attention should be paid to the carbon (15.72 at.%) and oxygen (12.25 at.%) contents identified during the analysis. The carbon peak may result from surface hydrocarbon adsorption originating from residual contaminants within the SEM vacuum chamber, whereas the presence of oxygen indicates the formation of thin oxide phases on the coating surface or partial surface oxidation upon exposure to the atmosphere [6].

To obtain an adequate physical assessment of the precursor's potential for forming the kesterite Cu2NiSn(S,Se)4 matrix phase, the contributions of the titanium substrate and surface-related atmospheric contaminants (C, O) must be excluded, and the metallic contents must be renormalized to 100 at.%: Cu + Ni + Sn = 100 at.%. The resulting normalized concentrations are as follows: Cu = 45.25 at.%, Ni = 33.00 at.%, and Sn = 21.75 at.%.

In the stoichiometric $Cu_2NiSn(S,Se)_4$ compound, the theoretical cation ratio Cu:Ni:Sn should be 2:1:1, corresponding to 50 at.% copper, 25 at.% nickel, and 25 at.% tin. Calculation of the characteristic technological parameters yields the following values:

1. **Copper cation ratio:** Cu / (Ni + Sn) = 18.46 / (13.46 + 8.88) ≈ 0.83. The value of 0.83 < 1.00 clearly indicates the formation of a copper-poor (Cu-poor) regime. In the physics of chalcogenide solar cells, Cu-poor conditions are considered favorable for suppressing deep donor defects associated with CuNi antisite defects and promoting

the formation of copper acceptor vacancies (V_{Cu}), which contribute to p-type conductivity of the absorber layer and potentially enhance the diffusion length of minority charge carriers.

2. **Ratio of divalent to tetravalent cations:** Ni / Sn = 13.46 / 8.88 ≈ 1.52. This value exceeds the stoichiometric ratio, reflecting a nickel-rich/tin-poor (Ni-rich/Sn-poor) composition in the precursor. From a technological perspective, excess Ni and a moderate deficiency of Sn may have certain advantages. During high-temperature selenization/sulfurization processes (500–550 °C), tin tends to evaporate intensively in the form of volatile tin monochalcogenides (SnS/SnSe). However, excessive nickel content requires careful control of the thermal treatment conditions to prevent the segregation of nickel sulfide/selenide phases (NiS, NiSe).

The background peaks of carbon (15.72 at.%) and oxygen (12.25 at.%) can be explained by their underlying physical origins. Carbon represents hydrocarbon adsorbates (contamination) deposited on the sample surface under the influence of the focused electron beam inside the SEM high-vacuum chamber. Meanwhile, oxygen is likely localized in an ultrathin surface oxide layer formed during the unavoidable short-term exposure of the metallic layers to ambient air after removal from the sputtering chamber.

Conclusion and Recommendations

Quantitative microanalysis using EDS confirmed the reproducible deposition of Cu/Sn/Ni precursor layers onto the titanium foil substrate. The Cu/(Ni+Sn) ratio of 0.83 corresponds to the required Cu-poor compositional regime, which is considered favorable for achieving high photovoltaic efficiency. The obtained elemental ratios provide a basis for accurately adjusting the magnetron sputtering durations of individual targets in order to compensate for tin losses during subsequent thermal chalcogenization and prevent the formation of excessive secondary phases.

References

[1] Alsulami, A. M. & Alsalme, A. M. Synthesis and characterization of multifunctional $Cu_2NiSnSe_4$ thin films and ITO/CdS/$Cu_2NiSnSe_4$/Au solar cell. *ECS J. Solid State Sci. Technol.* **13**, 124005 (2024).

[2] Dridi, S., Kanzari, M. & Rezig, B. One-step spray of Cu_2NiSnS_4 thin films as absorber materials for photovoltaic applications. *J. Mater. Sci. Mater. Electron.* **31**, 7193–7199 (2020).

[3] Beraich, M., Bouabellou, A., Bouguila, N. & Messad, S. Synthesis of tetragonal Cu_2NiSnS_4 thin film via low-cost electrodeposition method: Effect of Ni^{2+} molarity. *J. Electron. Mater.* **49**, 728–735 (2020).

[4] Salome, P. M. P. *et al.* Growth and characterization of Cu–Zn–Sn–S thin films on flexible metallic substrates for solar cell applications. *Mater. Sci. Semicond. Process.* **54**, 32–39 (2016).

[5] Yüksel, Ö. F., Özel, F., Akın, Ü. & Tuğluoğlu, N. Structural, optical and dispersion studies on $Cu_2NiSn(S, Se)_4$ nanocrystals thin films. *Physica B Condens. Matter* **625**, 413530 (2022).

[6] Stanchik, A. V. Morphology and crystal structure of $Cu_2NiSn(S,Se)_4$ thin films obtained by an electrodeposition-annealing process. *Coatings* **12**, 1198 (2022).

UDC: 538.911:548.73:621.315.592

RAMAN SPECTROSCOPY AND CHEMICAL MAPPING ANALYSIS OF MANGANESE-DOPED SILICON STRUCTURES

Matchonov Khusniddin Jamoladdinovich
Associate Professor, Urgench State University named after Abu Rayhan Biruni,
husniddin94_04@bk.ru

Annotatsiya: Ushbu maqolada marganets kiritilgan kremniy (p-Si<Mn>) qatlamlarining tebranish xususiyatlari, fonon modalarining evolyutsiyasi va fazaviy geterogenligi mikro-Raman spektroskopiyasi hamda kimyoviy xaritalash (2D/3D Raman mapping) usullari orqali tahlil qilindi. Termik ishlov berish haroratining 600°C dan 1200°C gacha ko‘tarilishi davomida amorf tuzilishdan (480-500 sm^{-1}) tartibli kristall holatga o‘tish hamda MnSi (~190, ~316 sm^{-1}) va Mn_4Si_7 (275-335 sm^{-1}) silitsidlarining o‘ziga xos fonon spektrlari aniqlandi. Termik kengayish koeffitsiyentlarining farqi va nostexiometriya tufayli fonon cho‘qqilarining 5-13 sm^{-1} gacha qizil siljishi va 15-20 sm^{-1} gacha kengayishi kuzatildi. 1200°C da o‘tkazilgan kimyoviy xaritalash yordamida silitsid fazalarining sirt bo‘ylab orolchali, geterogen taqsimlanishi vizual tarzda isbotlandi.

Kalit so‘zlar: *Raman spektroskopiyasi, kimyoviy xaritalash, mikro-Raman, fonon modasi, MnSi, Mn_4Si_7, optik fonon (TO), panjara zo‘riqishi, relaksatsiya.*

Аннотация: В данной статье с помощью методов микро-рамановской спектроскопии и химического картирования (2D/3D Raman mapping) проанализированы колебательные свойства, эволюция фононных мод и фазовая неоднородность слоев кремния, легированного марганцем (p-Si). При повышении температуры термической обработки от 600°C до 1200°C выявлен

переход от аморфной структуры (480-500 $см^{-1}$) к упорядоченному кристаллическому состоянию, а также обнаружены характерные фононные спектры силицидов MnSi (~190, ~316 $см^{-1}$) и Mn_4Si_7 (275-335 $см^{-1}$). Вследствие разницы коэффициентов термического расширения и нестехиометрии зафиксированы красное смещение фононных пиков на величину до 5-13 $см^{-1}$ и их уширение до 15-20 $см^{-1}$. Химическое картирование образцов, обработанных при 1200°C, наглядно подтвердило островковое, гетерогенное распределение силицидных фаз по поверхности.

Ключевые слова: *Рамановская спектроскопия, химическое картирование, микро-Раман, фононная мода, MnSi, Mn_4Si_7, оптический фонон (TO), решеточное напряжение, релаксация.*

Abstract: In this study, the vibrational properties, phonon mode evolution, and phase heterogeneity of manganese-doped silicon (p-Si) layers were analyzed using micro-Raman spectroscopy and chemical mapping (2D/3D Raman mapping). Upon increasing the thermal annealing temperature from 600°C to 1200°C, a transition from an amorphous state (480-500 cm^{-1}) to an ordered crystalline structure was observed, along with characteristic phonon spectra of MnSi (~190, ~316 cm^{-1}) and Mn_4Si_7 (275-335 cm^{-1}) silicides. Due to the discrepancy in thermal expansion coefficients and non-stoichiometry, a redshift of phonon peaks up to 5-13 cm^{-1} and peak broadening of 15-20 cm^{-1} were recorded. Chemical mapping of the samples annealed at 1200°C visually substantiated the island-like, heterogeneous distribution of silicide phases across the surface.

Key words: *Raman spectroscopy, chemical mapping, micro-Raman, phonon mode, MnSi, Mn_4Si_7, optical phonon (TO), lattice strain, relaxation.*

Introduction

Vibrational spectroscopy, particularly micro-Raman analysis, is one of the most sensitive techniques for identifying clusters, amorphous phases, and low-dimensional nanocompounds at early stages in semiconductor matrices. Manganese atoms introduced into the silicon lattice alter the lattice symmetry, deform local phonon vibrations, and lead to the formation of silicide phases.

Single-crystal silicon (c-Si) exhibits a narrow, distinct peak at 521 cm^{-1} corresponding to the zone-center TO phonon mode. However, residual stresses, defects, and secondary phases induced during doping and high-temperature diffusion manifest as characteristic shifts and broadenings in the vibrational spectra. In this study, the phonon characteristics, stress relaxation, and spatial inhomogeneity of phase distribution in the Si-Mn system were investigated using Raman spectroscopy and 3D chemical mapping.

Research Methodology

Materials and Experimental Methods

The samples were investigated using a SENTERRA II confocal micro-Raman spectrometer (Bruker Optik GmbH, Germany). The measurement parameters were set as follows:

- **Laser source:** A solid-state green laser with an excitation wavelength of λ = 532 nm (adjustable maximum power up to 25 mW).
- **Spectral range:** Wavenumber range of 50-4265 cm^{-1} with a spectral resolution of 4.0 cm^{-1}. The acquisition time per point was 100-120 s.
- **Temperature control:** To eliminate the local laser-induced heating effect, Stokes and anti-Stokes components were simultaneously acquired using a dual-channel system, and the actual temperature was monitored according to the modified Boltzmann distribution:

$$\frac{I_{\text{anti-Stokes}}}{I_{\text{Stokes}}} = \exp\left(-\frac{h\nu}{kT}\right)$$

Chemical Raman mapping was carried out on the surface of the p-Si sample thermally annealed at 1200°C over a 100 × 100 μm area via point-by-point scanning by generating a 2D phase distribution contrast map and a 3D intensity profile.

Temperature-Dependent Evolution of Phonon Modes

In the spectrum of the reference single-crystal silicon (c-Si), a characteristic line at 521.6 cm^{-1} corresponding to the zone-center TO phonon mode and a weak peak at 303 cm^{-1} attributed to two-phonon scattering (2TA) are observed. Following manganese doping of the samples, the following changes occurred depending on the thermal processing regime (figure-1):

Prior to thermal treatment and at T ≤ 600ºC: A broad, asymmetric dome-shaped band appears in the range of 460-500 cm^{-1}. This indicates the disruption of the Si matrix and the formation of an amorphous/nanocrystalline structure involving Mn atoms.

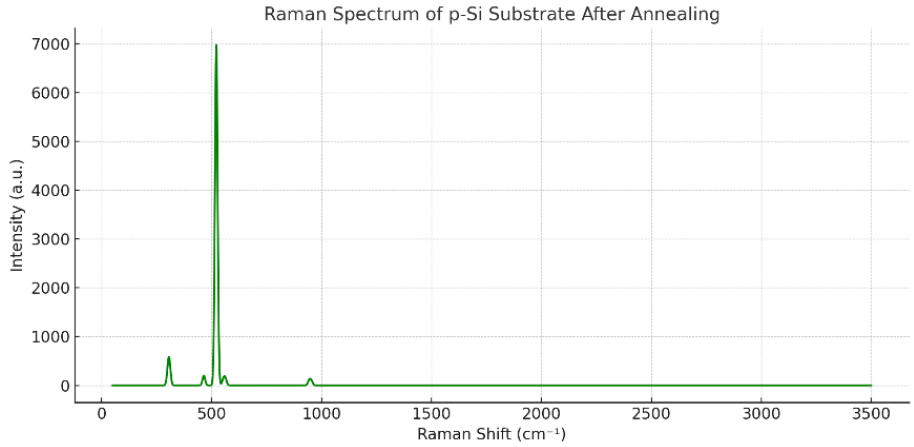


Fig. 1. Raman spectrum of the p-Si substrate after thermal annealing at 1200ºC.

Table 1. Characteristic Raman peaks, vibrational modes, and structural states of Mn–Si phases.

Phase state	Characteristic Raman Peaks (cm^{-1})	Vibrational Modes / Phonon Type	Structural Description
c-Si (initial)	521,6 va 303	TO(Γ) va 2TA	Single-crystal lattice order
a-Si + Mn	460–500 (Broad peak)	Acoustic / optical vibrational modes	Amorphized, disordered lattice
Mn_4Si_7	285, 305, 335	Tetragonal lattice mode	Higher silicide crystallites
MnSi (B20)	~190 va ~316	E and T modes	Cubic monosilicide phase

600-700ºC: Along with the restoration of the c-Si peak at 521 cm^{-1}, low-intensity peaks emerge in the 275-320 cm^{-1} region, signifying the initial nucleation of MnSi and Mn_4Si_7.

800-1000ºC: The degree of crystallinity increases, and a characteristic triplet forms at wavenumbers of ~285, 305, and 335 cm^{-1}. This reflects the complete crystallization of the higher silicide phase, Mn_4Si_7.

1100-1200°C: Stabilization of the optical phonon modes at ~190 and ~316 cm^{-1}, which are characteristic of the B20-structure MnSi intermetallic compound, is observed.

Strain Fields and Relaxation Processes

A redshift of 5-13 cm^{-1} in the experimentally recorded silicide Raman peaks relative to standard literature values, along with an increase in the full width at half maximum (FWHM) up to 15-20 cm^{-1}, was identified. This phonon softening is attributed to non-stoichiometry and tensile elastic strain resulting from the discrepancy between the thermal expansion coefficients of the silicide and the silicon substrate. When the thermal annealing temperature exceeds 1000°C, internal defects are annealed out, leading to strain relaxation and a reduction in peak width down to 8-10 cm^{-1} (figure-2).

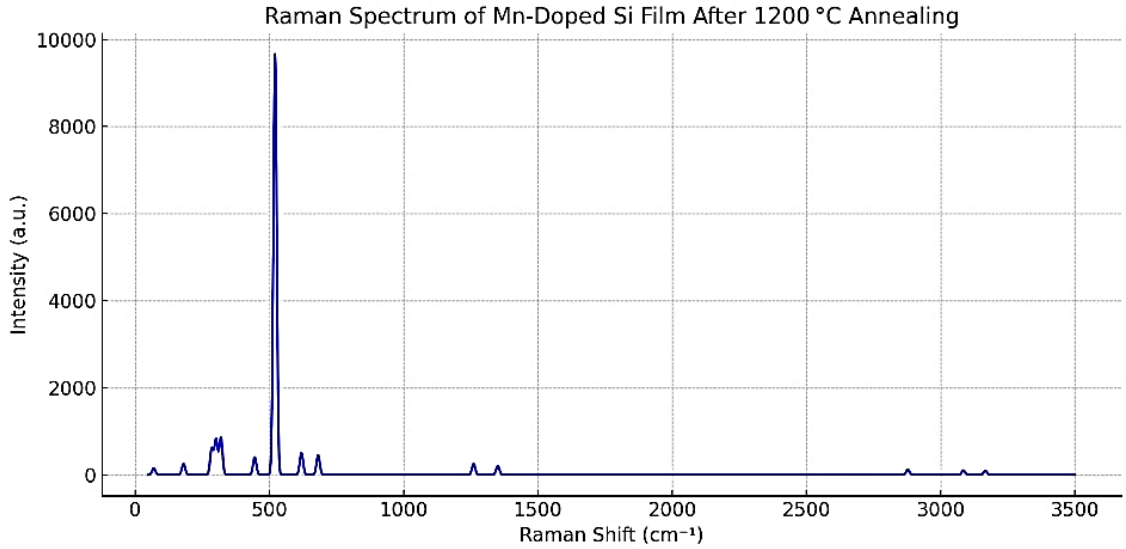


Fig. 2. Raman spectrum of the silicon sample doped with manganese (~20 at.%) obtained after thermal annealing at 1200°C (for 1 h in an inert atmosphere). Chemical Raman Mapping (1200°C)

The 2D phase contrast map and 3D intensity profile of the sample thermally annealed at 1200°C demonstrated a non-uniform distribution of silicides across the sample surface. Local maxima in the Raman intensity ranging from 2000 to 2700 a.u. correspond to regions where MnSi and Mn_4Si_7 silicides segregated into distinct clusters (domains). This observation fully confirms the phase separation induced by the low solid solubility of Mn in silicon at high temperatures (figure-3).

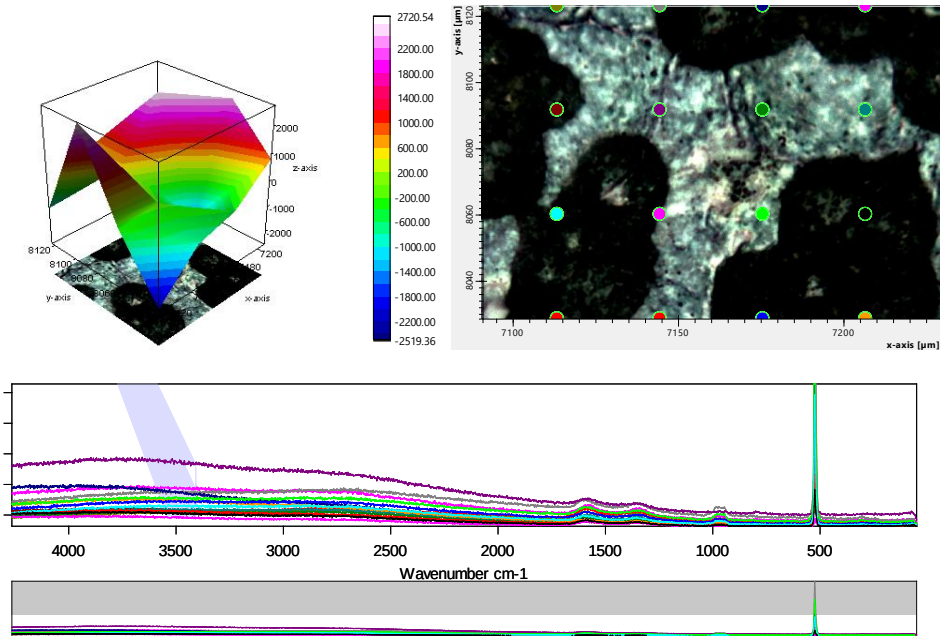


Fig. 3. Chemical Raman image of the p-Si sample after thermal annealing at 1200°C: signal intensity distribution (color scale, 3D), phase contrast map (upper right corner), and integrated spectra acquired from selected regions (bottom).

Conclusion and Recommendations

Micro-Raman spectroscopy and chemical mapping techniques demonstrated high efficacy in revealing phase transformations, lattice strain, and phase heterogeneity in the Si-Mn system at the microscale. The identified characteristic phonon peaks (190 and 316 cm^{-1} for MnSi; 285, 305, and 335 cm^{-1} for Mn_4Si_7) enable contactless and non-destructive identification of silicide phases. The shifts of 5-13 cm^{-1} observed in the Raman spectra can be utilized as a diagnostic parameter to monitor mechanical stresses at the interface.

References:

[1] Dupin, N., Sundman, B., Kattner, U. R. et al. Implementation of an effective bond energy formalism in the multicomponent CALPHAD approach. *Calphad*, 43, 18-31 (2013).

[2] Utamuradova, Sh.Kh. Daliev, J.J. Khamdamov, Kh.J. Matchonov, M.K. Karimov, Kh.Y. Utemuratova, East Eur. J. Phys. 1, 276 (2025), https://doi.org/10.26565/2312-4334-2025-1-32

[3] Li Z. et al. On Curie temperature of B20-MnSi films with $MnSi_{1.7}$ admixture. *Scientific Reports*, 12, 16388 (2022).

[4] Steiner T. et al. Thermoelectric properties of $MnSi_{1.7}$ thin films. *J. Appl. Phys.*, 111, 083709 (2012).

[5] Ishikawa Y. et al. Magnetic properties of MnSi with B20 structure. *Phys. Rev. B*, 31, 5884 (1985).

[6] Sh.B. Utamuradova, Kh.J. Matchonov, J.J. Khamdamov, and Kh.Y. Utemuratova, "X-ray diffraction study of the phase state of silicon single crystals doped with manganese". New Materials, Compounds and Applications, 7(2), 93-99, (2023). http://jomardpublishing.com/UploadFiles/Files/journals/NMCA/v7n2/Utamuradova_et_al.pdf

[7] Bruker Optik GmbH. *SENTERRA II User Manual* (2018).

[8] ICDD PDF-4+ Database. International Centre for Diffraction Data (Release 2023).

[9] Liu, C. et al. Mn silicide formation by solid phase reaction in Mn/Si thin films. *Applied Surface Science*, 2010, 256: 6134-6139.

[10] Misra, A., Bhatnagar, M. C. *Raman Imaging in Semiconductor Materials*. Materials Today: Proceedings, 2022, 49(5), 1751-1756. https://doi.org/10.1016/j.matpr.2021.09.313

[11] Ruan, Q. et al. *Chemical Imaging of Silicon-Based Heterostructures Using Confocal Raman Microscopy*. J. Raman Spectrosc., 2019, 50(12), 1733-1740. https://doi.org/10.1002/jrs.5678

[12] Wang Y. et al. Epitaxial growth and properties of MnSi and Mn_4Si_7 nanolayers on silicon substrates. *Applied Physics Letters*, 96, 042503 (2010).

[13] Novikov S. I. et al. *Formation of manganese silicides in silicon films by high-temperature annealing. Semiconductors*, 54, 1105-1110 (2020).

[14] Ferri, F. A. et al. *Evidence of magnetic vortices formation in Mn-based sub-micrometre structures embedded in Si–Mn films.* Journal of Physics D: Applied Physics, 42, 132002 (2009).

[15] Kim, Y.-W. et al. *XRD and Raman investigation of manganese silicide thin films on silicon.* Thin Solid Films, 516, 7053–7058 (2008).

UDC: 538.911:548.73:621.315.592

X-RAY DIFFRACTION ANALYSIS OF Si <Mn, S> SAMPLES

Mavlyanov Abdulaziz Shavkatovich
Acting Deputy Director of Institute of Semiconductor Physics and Microelectronics
microelectronics74@mail.ru

Annotatsiya: Maqolada ilgari xajmda joylashgan va Mn va S kirishma atomlari bilan legrlangan monokristalli kremniyning qatlamlarining rentgen difraksiya (XRD) tahlili natijalari keltirilgan. Marganets va oltingugurt atomlari bilan legimlangan kremniy namunalarining strukturaviy va fazaviy holatlari Shimadzu LabX XR-6100 difraktometrida oʻrganildi. Rentgen difraksiya oʻlçovlari Bragg-Brentano nur geometriyasi 2θB da 10° dan 80° gacha boʻlgan diapazonda 2.0000 grad/min skanerlash bosqiçi va 0.0500 (gradus) burchak bosqiçi bilan uzluksiz ravishda amalga oshirildi. Namunalar Cu Kα nurlanishi (40 kV, 30 mA) yordamida vizualizatsiya qilindi. Hisob-kitoblar uchun 1.54060 Å toʻlqin uzunligi işlatilgan. Har bir nuqtada belgilangan vaqt 1,5 soniya edi. Eng kuchli uçta

çoʻqqidan birining, yaʻni 2θ=64.1835° çoʻqqining tabiatini aniqlaş yoki biron bir aniq fazaga boğlash qiyin. Mualliflar bu çoʻqqining marganets, oltingugurt va kremniyning kristalli birikmalari bilan boğliqligini ta ʻkidlaydilar.

Kalit soʻzlar: *kremniy, gibrid struktura, diffuziya çuqurligi, yarimoʻʻtkazgiç, nuqsonlar, kubik panjara, izovalent boʻlmagan birikma, rentgen strukturaviy tahlili, çoʻqqilar, kristallografik tekislik.*

Аннотация: В статье представлены результаты рентгенодифракционного анализа (XRD) ранее полученных объемных слоев монокристаллического кремния, легированного примесями Mn и S. Исследования структурного и фазового состояний в образцах кремния, легированных атомами марганца и серы, проводились на дифрактометре Shimadzu LabX XR-6100. Рентгенодифракционные измерения проводились в геометрии пучка Брэгга-Брентано 2θБ в диапазоне от 10° до 80° непрерывно с шагом сканирования 2,0000 град/мин и угловым шагом 0,0500 (град). Образцы визуализировались с использованием излучения Cu Kα (40 кВ, 30 мА). Для расчетов использовалась длина волны 1,54060 Å. Заданное время в каждой точке составляло 1,5 секунды. Природа одного из трех наиболее интенсивных пиков, а именно пика 2θ=64,1835°, трудно поддается определению или отнесению к какой-либо фазе. Авторы предполагают, что указанный выше пик, скорее всего, связан с кристаллическими соединениями марганца, серы и кремния.

Ключевые слова: *кремний, гибридная структура, глубина диффузии, полупроводник, дефекты, кубическая решетка, неизовалентное соединение, рентгеноструктурный анализ, пики, кристаллографическая плоскость.*

Abstract: The paper presents the XRD analysis of previously bulk layers of single crystal silicon samples doped with Mn and S impurities. Studies of the structural and phase states in silicon samples doped with manganese and sulfur atoms were carried out on Shimadzu LabX XR-6100 diffractometer. The X-ray diffraction measurement activities were done in Bragg-Brentano $2\theta_Б$ beam geometry in the range from 10° to 80° continuously at a scanning step of 2.0000

deg/min and an angular step of 0.0500 (deg). Samples were imaged using Cu Ka radiation (40 kV, 30 mA). A wavelength of 1.54060 A was used for calculations. The specified time at each point was 1.5 seconds. The nature of one of the three most intense peaks, namely of the peak 2θ=64.1835°, is difficult to determine or assign to any phase. The authors assume that the above peak could most likely could be related to crystalline compounds of manganese, sulfur, and silicon.

Keywords: *Silicon, hybrid structure, depth of diffusion, semiconductor, defects, cubic lattice, non-isovalent compound, XRD analysis, peaks, crystallographic plane.*

Introduction

The formation of quasi-molecular electroneutral bonds between transition group element impurities and oxygen in silicon have been intensively studied by numerous research laboratories over recently. In particular, in [1; 2] how molecular complexes of Si-IV/III-V and Si-IV/II-VI type could be grown on various substrates, have been in detail described in. The materials based on these complexes are often used for engineering optically sensitive materials on a silicon substrate. In [3-6] researchers present the idea and technique of how molecular precursors could be used for engineering growth of non-isovalent Si_3AlP-bonds that could manifest themselves as a hybrid between silicon matrix and AlP matrix. These quasi-molecular bonds are believed to be located at adjacent sites thus forming new structures in the lattice. In particular, the authors in [7] argue that in the process of formation of electroneutral complexes like Si_2OMn, one might anticipate incidental occurrence of tetrahedral structures in the silicon crystal lattice. These structures are believed to slightly distort the lattice periodicity of basic matrix, however their properties hugely differ from those of pure silicon unit cell. In the abovementioned research [7], the authors conclude that there might occur a mixed “ionic-covalent” type of chemical bonding and a unique electron binding energy. An increase in the number of such tetrahedral units creates the preconditions for their interaction and the formation of larger structures, including nanocrystals of a new phase, which will be characterized by their own key physical and energy parameters. Also, in [7] the authors state that if other elements of the transition

group interacted with sulfur in the temperature range of intensive decomposition of the solid solution “silicon – sulfur” (800 ÷ 950º C), in the case of manganese such interaction seemed to take place directly in the process of diffusion of silicon with manganese, previously doped with sulfur. In [8], the authors describe the formation of exchange-coupled sulfur and manganese complexes in silicon. In this paper they anticipate that during heat treatment of silicon crystals, that were previously diffusion doped with sulfur and one of the transition group elements in a certain temperature range, intense interaction between these impurity centers seems to occur, accompanied by electrical neutralization of both impurity centers. To have an idea about the structure of electrically neutral chemically bonded sulfur and manganese complexes, the authors in [9] studied the electronic paramagnetic resonance (EPR) spectra of silicon crystals sequentially doped with sulfur and manganese. For comparison, the EPR spectra of reference *Si<S>* and *Si<Mn>* crystals were also studied. Having analyzed the results of the above studies, the authors suggested that the observed EPR spectrum at weak fields in *Si <S,Mn>* and *Si <Mn>* crystals is due to the presence of exchange-coupled complexes between impurity centers, since the complexes, interacting with each other, create strong internal magnetic fields. Besides, the hypothesis of formation of a "hybrid" structure with Si_2MnS -type phases in an idealized case were reviewed in [10-11]. The crystal model and quantum mechanically calculated parameters of Si_2MnS -type phases were in detail given in [12-14]. Further studies into possibility of forming such bonds, especially XRD analysis of silicon samples with transition group elements and sulfur could incidentally shed light into revealing new phases and structures in the basic matrix of silicon.

Research Methodology

Materials and Experimental Methods

Doping of silicon samples with sulfur and manganese by using diffusion doping technique in vacuumed (10^{-4} bar) and sealed quartz ampoules at a temperature of 1260 °C and 1200 °C, respectively, was carried out for a duration that would ensure uniform distribution of impurities in the bulk of the crystal. The initial samples were Si doped with boron, with an initial specific resistance in the range of ρ = 1 Ω·cm. After doping

with Mn and S, the initial silicon remained of *p*-type, but the resistivity increased to $\rho = 2.4 \times 10^4$ Ω·cm. Studies of the structural and phase states in silicon samples doped with manganese and sulfur atoms were carried out on Shimadzu LabX XR-6100 diffractometer. The X-ray diffraction measurements were carried out in Bragg-Brentano $2\theta_Б$ beam geometry in the range from 10° to 80° continuously at a scanning step of 2.0000 deg/min and an angular step of 0.0500 (deg). Samples were imaged using Cu Ka radiation (40 kV, 30 mA). A wavelength of 1.54060 A was used for calculations. The specified time at each point was 1.5 seconds.

Results and Discussion

The experimental data of the X-ray study of the *p*-type Si <MnS> sample is shown in Fig. 1 and Table 1. In the diffraction pattern, a number of structural reflections of a selective nature with varying intensity can be observed, as can be seen from the diffraction pattern of the p-type Si <MnS> sample. An analysis of the results shows that that the most intense peaks correspond to *2θ=43.8204°*, *2θ=64.1835°* и *2θ=77.3023°* with structural reflection intensities of 100, 77 and 53 and lattice parameters d=2.06430 Å, d=1.44990 Å и d=1.23331Å, (Fig. 1). The peak 2θ=77.3023° (crystallographic direction 420) corresponds to manganese sulfide in the cubic modification F43m-β-MnS, which is confirmed by the calculated data from the *materialsproject.org/materials/mp-1783/* database (Fig. 2). The intensity of this reflection increases significantly and, in Si,<Mn,S> sample it is almost 53.

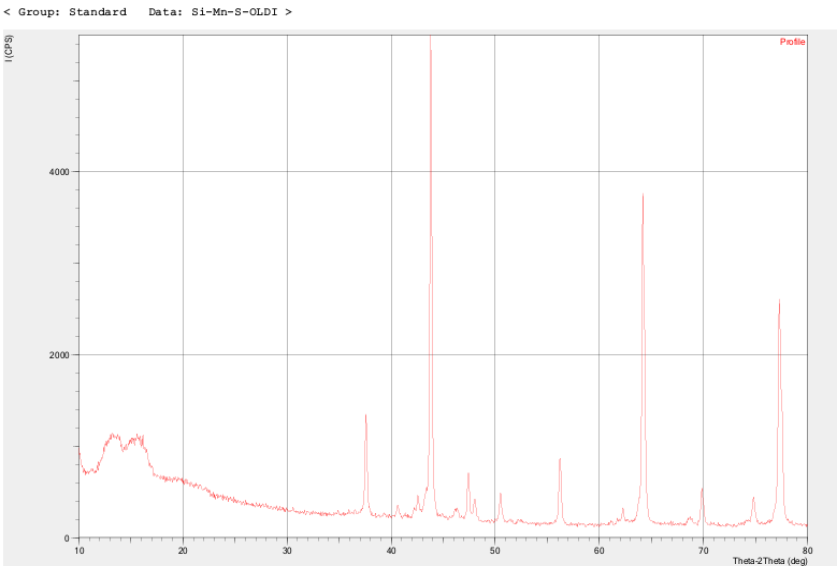


Fig. 1. X-ray diffraction pattern of the sample Si <Mn, S> on Shimadzu LabX XR-6100

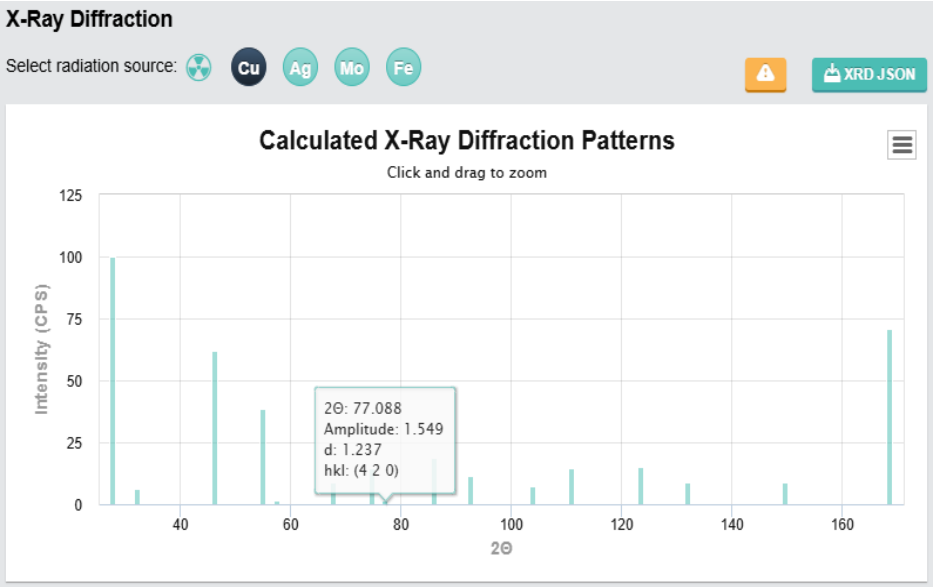


Fig. 2. Calculated X-ray diffraction pattern of manganese sulfide in the cubic modification F43m-β-MnS with a peak 2θ=77.088 (420) (Calculated data of the database materialsproject.org/materials/mp-1783/)

Table 1. Basic XRD Data Process for Si <MnS> sample

Group : Standard
Data : Si-Mn-S-OLDI TARAFI # Strongest 3 peaks

no	peak no.	2Theta (deg)	d (A)	I/I1	FWHM (deg)	Intensity (Counts)	Integrated Int (Counts)
1	16	43.8204	2.06430	100	0.18540	6222	26381
2	23	64.1835	1.44990	77	0.20000	4818	20444
3	27	77.3023	1.23331	53	0.23070	3297	17680

Peak Data List

peak no.	2Theta (deg)	d (A)	I/I1	FWHM (deg)	Intensity (Counts)	Integrated Int (Counts)
1	12.6834	6.97371	3	0.56300	215	3398
2	13.0816	6.76231	4	0.00000	240	0
3	13.2808	6.66133	5	0.00000	280	0
4	13.4302	6.58756	4	0.00000	231	0
5	13.6295	6.49168	4	0.00000	223	0

6	13.8287	6.39861	4	0.00000	226	0
7	13.9782	6.33051	3	0.29020	194	1316
8	15.0747	5.87242	3	0.61700	199	2758
9	15.3240	5.77744	3	0.00000	211	0
10	15.6731	5.64953	4	0.00000	274	0
11	15.9225	5.56160	4	0.00000	269	0
12	16.1719	5.47639	4	0.97360	269	3965
13	37.5902	2.39086	21	0.18850	1287	6033
14	42.5716	2.12192	4	0.19260	258	1566
15	43.2817	2.08874	4	0.32860	238	2955
16	43.8204	2.06430	100	0.18540	6222	26381
17	47.4266	1.91541	10	0.19380	648	2891
18	48.0237	1.89298	5	0.21220	300	1753
19	50.4958	1.80595	6	0.19650	393	2026
20	56.2100	1.63515	15	0.21320	953	4785
21	62.2658	1.48987	3	0.17310	217	991
22	63.7231	1.45926	3	0.22340	198	1999
23	64.1835	1.44990	77	0.20000	4818	20444
24	64.5229	1.44309	4	0.11160	262	1989
25	69.8479	1.34553	8	0.22180	493	2530
26	74.7883	1.26841	6	0.25070	380	2483
27	77.3023	1.23331	53	0.23070	3297	17680
28	77.7191	1.22774	3	0.12980	198	1679

For the single crystal silicon wafer with the <100> plane orientation, the X-ray diffraction peaks appear at 69.24, 65.84, 61.68, 33.0 (JCPDS). It was found that 69.24

denotes the Si 004 CuK_{α} plane. 33.0 for the Si <200> CuK_{α}, 61,68 - Si <004> CuK_{β}, 65,84 Si <004> - WL_{α}.

In the paper [15], an X-ray diffraction analysis was performed of metastable thin films of manganese sulfide obtained by chemical deposition in a bath. X-ray diffraction analysis showed the presence of metastable phases β and γ – MnS in the films. The paper [15] shows the diffraction pattern of MnS films deposited on the substrate at different molar ratios. The onset of crystallization was detected in the diffraction pattern of the film deposited at a molar ratio of 1:1. An increase in the intensity of the diffraction peaks with an increase in the molar fraction (1:2 and 1:3) revealed an improvement in the degree of crystallization of the MnS films. The diffraction reflections along the orientations (211), (102), (110), (103), (004) (58.4) and (202) were assigned to the γ-MnS phase of the hexagonal wurtzite structure (JCPDS File No.:89-4089; 65-3333). Diffraction reflections along the (111) and (200) directions correspond to the β-MnS (32,40) phase of the zinc blende structure (JCPDS File No.: 40-1288). The presence of this peak is confirmed by the calculated data of the peak (2θ=32,361(200)) (Fig. 3) of F43m-β-MnS from the *materialsproject.org/materials/mp-1783* database.

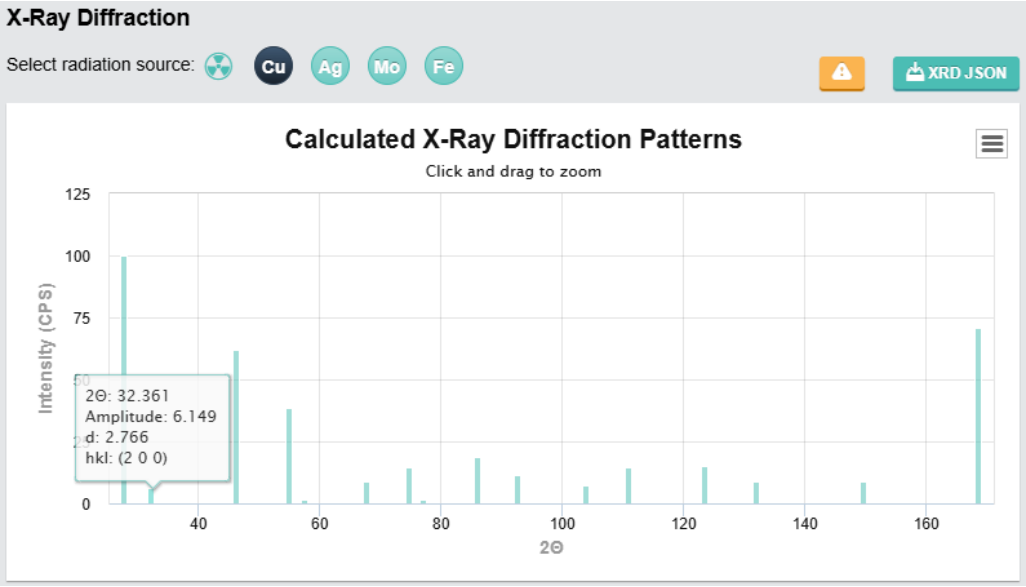


Fig. 3. Calculated X-ray diffraction pattern of manganese sulfide in the cubic modification F43m-β-MnS with a peak 2θ=32.361(200) (Calculated data from the materialsproject.org/materials/mp-1783/ database)

The most intense peak 2θ=43.8204° (202) corresponds to bonds of silicon and manganese in the presence of oxygen [4], since such a peak was revealed neither in the

calculated data from the materialsproject.org/materials/mp-1783 database for manganese monosulfide in both β-MnS nor in γ – MnS modifications mentioned in [15].

For a single crystal silicon wafer with <100> crystallographic orientation, the X-ray diffraction peak appears at 69.24 (JCPDS data revealed that 69.24 represents the Si 004 CuK_{α} plane).

The nature of one of the three most intense peaks, 2θ=64.1835°, is difficult to determine or assign to any phase. They most likely belong to crystalline compounds of manganese, sulfur, and silicon, whose size is 48.955401 nm (Debye-Scherrer equation).

In addition to the main reflections, the diffraction pattern also contains structural lines with broad diffuse reflection and a number of other structural lines with low intensity and a diffuse reflection band at scattering angles 2θB in the range from 15 to 80°. The observed reflections at these scattering angles on the surface layers of the studied samples indicate that they are caused by small structural fragments formed with the participation of oxygen impurities.

Conclusion and Recommendations

Thus, quasi-molecular electroneutral compounds or so-called exchange-coupled complexes between transition element impurities and elements, in particular of group VI inside the silicon lattice, could become the platform for the subsequent development of silicon semiconductors with novel optical and electrophysical properties.

The purpose of this study was to investigate the behavior of manganese and sulfur atoms in the silicon crystal lattice using the X-ray diffraction method and thus, the phase states of manganese and sulfur atoms in silicon have been studied using the X-ray diffraction method.

The nature of one of the three most intense peaks, namely of the peak 2θ=64.1835°, is difficult to determine or assign to any phase. We assume that this peak could most likely could be related to crystalline compounds of manganese, sulfur, and silicon, whose size is 48.955401 nm (Debye-Scherrer equation).

References

[1] Jiang, L., Aoki, T., J. Smith, D., Andrew, V., and Chizmeshya G., et al., Nanostructure-Property Control in AlPSi3/Si(100) Semiconductors Using Direct Molecular Assembly: Theory Meets Experiment at the Atomic Level, *C Chem. Mater.,* 2014, vol. 26, p. 4092.

[2] Kang, J., Park, J., Stradins P., and Wei S., Nonisovalent Si-III-V and Si-II-VI alloys: Covalent, ionic, and mixed phases. *Physical Review B.,* 2017, vol. 96, p. 045203-1.

[3] Watkins, T., Chizmeshya, G., Jiang, L., Smith, D., Beeler, R. T., Grzybowski G., and Menéndez, J., and et.al., Nanosynthesis Routes to New Tetrahedral Crystalline Solids: Silicon-like Si_3AlP, *J. Am. Chem. Soc.*, 2011, vol. 133, p. 16212.

[4] Yang J.-H., Zhai, Y., Liu, H., Xiang, H., Gong X., and Wei., S.-H., Si3AlP: A New Promising Material for Solar Cell Absorber. *J. Am. Chem. Soc.,* 2012, vol. 134, p. 12653.

[5] Watkins, T., Jiang, L., Xu, C., Chizmeshya, G., Menéndez, J., and J. Kouvetakis, et al., (Si) 5− 2y (AlP) y alloys assembled on Si (100) from Al-P-Si3 building units. *Appl. Phys. Lett.,* 2012, vol. 100, p. 022101.

[6] Jiang, L., Aoki, T., Smith, D. J., Chizmeshya, G., and J. Kouvetakis, Nanostructure–Property Control in $AlPSi_3$/Si(100) Semiconductors Using Direct Molecular Assembly: Theory Meets Experiment at the Atomic Level. *Chem. Mater.*, 2014, vol. 26, p. 4092.

[7] М. К. Бахадирханов, Х. М. Илиев, М. О. Турсунов, С. Б. Исамов, С. В. Ковешников, М. Х. Маджитов. Неорганические материалы, 2021, Т. 57, № 7, стр. 685-692.

[8] Shoikrom Askarov, Bashirulla Sharipov, Abdulaziz Mavlyanov, Shohista Saliyeva, Barnokhon Ibragimova. Exchange-coupled sulfur and manganese complexes in silicon / Samarkand International Symposium on Magnetism, SISM-2023, Samarkand State University on July 2-6, 2023. p.99.

[9] Sh. Askarov, B. Sharipov, A. Mavlyanov, Sh. Saliyeva, B. Ibragimova. On how “sulfur-manganese” bonds might occur in silicon//First International Conference on Low-Dimensional Advanced Materials ICLODAM-24, February 21-22, 2024 Tashkent, Uzbekistan, pp.88-89.

[10] Sh. B. Utamuradova, A. Sh. Mavlyanov, Sh. A. Sobirova, and O. E. Sattarov. Hybrid Secondary Structure of Manganese and Sulfur in Silicon/Surface Engineering and Applied Electrochemistry, 2025, Vol. 61, No. 5, pp. 633–636

[11] Utamuradova, Sh., Mavlyanov, A., Uteniyazova, A., Matchonov, Kh., Numerical calculation of optimal duration and temperature of diffusion of impurity atoms of Sulfur and Manganese, *Electronic Journal Of Actual Problems Of Modern Science, Education And Training*, 2025,. Issn 2181 -9 750, p.124.

[12] A.Mavlyanov, M.Khakkulov, O.Abjalilov, M.Azizov. Mn_2S Covalent Tetrahedral Structure Spatial Analogue in Si / 21st International Conference on defects in insulating materials - ICDIM 2024, 19 –23 August, Astana, Kazakhstan, pp. 15.

[13] Sh.B. Utamuradova, A.Sh. Mavlyanov, Kh.J. Matchonov. Study and calculation of sulfur-manganese-silicon cell in silicon lattice // European Science Review, 2024, No 9-10, pp.16-20. (SJIF 2024 = 6.735).

[14] Sh.B. Utamuradova, A.Sh. Mavlyanov. Cubic “F43m - β -MnS” (zinc blende)-type hypothetical structure of Si_2MnS // Физика полупроводников и микроэлектроника 2024, том 6, Вып.6, стр. 32-37

[15] R. Sivakumar et al. Metastable MnS films prepared by the addition of EDTA using chemical bath deposition technique/Int.J. ChemTech Res.2014-2015,7(2), pp 974-978.